Nonlocal Models with Applications to Ecology

by

E. Ellefsen

B.A., Luther College, 2017

M.S., University of Colorado Boulder, 2020

A thesis submitted to the

Faculty of the Graduate School of the

University of Colorado in partial fulfillment

of the requirements for the degree of

Doctor of Philosophy

Department of Applied Mathematics

2022

Committee Members:

Nancy Rodríguez, Chair

Zachary Kilpatrick

David Bortz

Mark Hoefer

Brett Melbourne

Ellefsen, E. (Ph.D., Applied Mathematics)

Nonlocal Models with Applications to Ecology

Thesis directed by Prof. Nancy Rodríguez

Understanding how species move in their environment is a key objective in ecology. In the face of climate change, invasive species, and habitat destruction, understanding primary factors that drive species can help predict how territories change or whether a species survives as the environment changes, another species goes extinct, or a competing species invades. Mechanistic models using only local information and local processes have been used to understand the forces that drive species movement and to predict the persistence or extinction of species. However, many ecological phenomena are deeply affected by nonlocal interactions and reactions, and including these forces into mathematical models can change the dynamics and more accurately describe observed phenomena. We investigate two particular ecological phenomena affected by nonlocal forces.

First, we study a nonlocal mechanistic model describing territory development of social groups to determine the most prominent mechanisms driving movement. While the nonlocal nature of this model leads to a better approximation of physical reality, it also causes numerical and analytical challenges. The focus in this work is to address these issues. Therefore, we employ several strategies to solve the nonlocal system of equations. We are particularly interested in model verification through the connection with data and understanding how the nonlocal terms and parameters in the model influence solutions.

Second, we investigate an integro-differential equation modeling a birth-jump process, where birth and dispersal cannot be decoupled. This has been argued to be a more suitable model for processes such as seed dispersal, cancer cell growth, and fire propagation. We prove global existence and uniqueness of solutions and investigate persistence and extinction of a population subject to various growth terms. We are particularly interested in cases where a population can overcome the Allee effect, where population density affects the fitness of individuals.

Contents

Chapter

Tables

Table

Figures

Figure

Chapter 1

Introduction

Mechanistic models, which use theory to predict the real world, are powerful tools that can help understand complex biological phenomena. In particular, mechanistic models using only local information and processes have been used to describe diverse ecological phenomena such as competition, dispersal, consumption of resources, and territory use [62, 102, 7, 71]. However, there are systems in ecology and biology that are deeply affected by nonlocal interactions or reactions. For example, consider the COVID-19 virus. It is well known that COVID-19 is spread through particles in the air [29]. Thus, an infected individual can spread this virus to an individual at a different spatial location. Nonlocal processes also occur at the cellular level [50]. Chemotaxis is the process through which a cell senses a chemical gradient which directs its movement, and this can be considered a nonlocal process [101, 49]. In [49], the authors consider a chemotaxis model with a finite sampling radius, meaning the sampling is nonlocal. Some cells can sense their environment through long protrusions that probe the area around them [3, 85]. These nonlocalities have been included in cellular models and have been used to understand cancer cells [34].

In ecology, nonlocal forces are also at work as individuals gather information about their local environment, such as location of food resources, temperature, environmental features, predator and prey locations, and location of conspecifics [16, 83]. Many species sense their surroundings and use this information to aggregate in flocks, swarms, herds, and social groups, to avoid predators, and to hunt prey [30, 35, 57, 72]. Gathering information about one's environment is inherently nonlocal [23, 63]. Consider the process of observing locations of predators, prey, or conspecifics.

These observations can happen at a distance, and individuals might use these observations to avoid these locations in the future. They also might be attracted to locations where they have previously encountered members of their own species or group. This is all evidence of nonlocal information influencing decisions in species. Therefore, understanding the effects of nonlocal forces in ecological processes has become of great interest. For example, the system of Lotka-Volterra equations that models competition between species has been intensely studied. Recently, variants including nonlocal competition have been of interest, [32, 46, 67, 98], as well as nonlocal dispersal [5, 79, 109], which has also been included in various ecological models [24, 61, 99, 100, 61, 104]. In ecology, the question of which dispersal strategies are advantageous in a population is an important one as it can lend insight into what strategies persist in populations through the process of natural selection. This has been explored in some cases with nonlocal dispersal, [28, 70]. In [28], the authors investigate which nonlocal dispersal strategies are evolutionarily stable, meaning a population using this strategy is resistant to invaders. They determine that the only evolutionarily stable nonlocal dispersal strategies are those that lead to all individuals in the population having equal fitness with no movement of individuals at equilibrium.

Nonlocal interactions can produce markedly different results than their local counterparts, often leading to dynamics that more closely describe what is observed than when nonlocal processes are ignored. For example, cell-cell adhesion is a biological phenomenon that is important in many areas of biology such as early embryo development and tumor growth. A continuous nonlocal model of cell-cell adhesion was able to replicate observed cell-sorting behavior that was previously only able to be accomplished through discrete models [3]. In [64], the inclusion of nonlocal interactions in competition enhances the possibility of coexistence between competing species. The inclusion of nonlocal advection in home range [13] and territory [90] models has ensured well posedness of the model, and is necessary to model cohesive swarms [72]. In other cases, the nonlocal advective term allows a model to avoid blow up and ensure global existence of solutions [33, 49, 11, 21].

We study nonlocal dispersal and advection under the umbrella of two ecological phenomena, the first being territory development of social groups. Social interactions and social groups are

not exclusive to the human population, and certain animal populations also move and live in social groups, *e.g*, deer, wolves, lions, and meerkats [108, 107, 7]. To better understand nonlocal processes involved with territory development of social groups, we investigate a nonlocal mechanistic model that incorporates nonlocal aggregation within a group and nonlocal segregation between groups. The second phenomenon we consider is a population where birth and dispersal cannot be decoupled, which we model as a birth-jump processes. Dispersal in populations is often modeled using linear diffusion, describing random dispersal of individuals. While this is reasonable for many populations, for processes such as fire propagation or cancer cell growth, dispersal is a nonlocal process and is linked to birth. Thus, birth-jump processes have been introduced to understand phenomena where birth and dispersal cannot be decoupled [48, 12, 93].

1.1   Nonlocal Territorial Models in Ecology

Learning about the local environment is essential to a species' survival. Interactions within a social group, competition with conspecifics, foraging, and avoiding predators are a few examples of processes that inform how a species moves in its environment, and these are essential in understanding and predicting territories of species. For example, wolves move according to the scent of their pack, scents of conspecifics, pack density, the location of wolf pups, foraging to find food, and dispersal to mark territory [107]. Understanding how individuals interact with each other and their environment, a core objective of theoretical ecology, is particularly crucial as climate change is altering the habitats of many species [73, 103]. A recent study in Nature [86] brought forward significant evidence that 279 species (out of 1700 in their study) had been affected by climate change, and the use of mathematical models to obtain insight into this issue can be extremely powerful. Mathematical models can use the mechanisms that inform territory decisions to predict how territories change or redistribute in response to the environment, or a change in the territory of another species.

Mechanistic models can be used to study how populations live and move in their environment by utilizing the underlying description of the primary drivers of movement. In some cases,

mechanistic models can be more useful than stochastic models due to their predictive ability and ability to compare to field measurements [74]. They have been used to describe foraging [44, 43], aggregation [45], and home ranges [59, 71] . Mechanistic home range models connect species movement, territory formation, environment favorability, and space use [76, 75]. In [51] and [82], these models included diffusion and attraction to a home center, such as a den site, to generate stable territory patterns. More realistic mechanistic models have been considered since, incorporating scent marking [74] and habitat selection [77].

A modeling framework which has been heavily used in biology and ecology is that of reaction-advection-diffusion equations [16, 14, 83, 68, 19, 18, 17]. These models can be derived mechanistically from individual based models, and use assumptions of random and directed movement, birth, and death to help make conclusions about persistence, extinction, and coexistence in species [16]. Local reaction-advection-diffusion (RAD) models, or those that only take local information and local processes into account, have been used with success to predict the territories of species such as wolves, [107], coyotes, [74], and meerkats, [7]. Such verified models can then be of use to help predict how territories will evolve as the environment changes or how different groups will redistribute if a group becomes extinct. Local mechanistic models attempt to capture the social and environmental dynamics that govern how competing subgroups of a species interact with one another. Generally, local RAD models incorporate inter- and intra-group dynamics, or the dynamics within and between groups, respectively, and preferences toward favorable patches in the environment [27, 96]. However, as mentioned earlier, it is the case that the process of gathering information about a local environment is inherently nonlocal. Thus, there are cases where local RAD models alone are insufficient to explain certain observed phenomena without the introduction of artificial dynamics. In the local system introduced to model the dynamics of territory use of meerkats, an advective term pointing in the direction of an artificial home center was introduced in order to keep different groups coherent [7]. Recent evidence shows that some animals avoid locations where they have previously encountered a member of another group (see for example [26, 7]). This implies that these animals inform their decision of where to move based on nonlocal information.

We introduce a system of nonlocal RAD equations to model territory formation of social groups which we argue to be more suitable for the case where there is no home center. Due to the analytical and computational expense of the nonlocal term, we investigate several methods to efficiently find solutions to the model. We are particularly interested in solving the system efficiently in order to connect the model with data and to better understand the effects of diffusion, aggregation, segregation, and the environment on solutions.

1.2   Birth Jump Processes

The movement of individuals from one location to another, known as dispersal, can greatly influence the development of a population. For example, dispersal can help populations control their size or expand their territory. While dispersal can be beneficial to species, in some cases it can be detrimental. High dispersal rates can prevent the adaptation of a population to a new environment, which can hinder the survival of small populations [91]. In fact, the effect that dispersal has on the dynamics of a population is very complex and thus developing mathematical models that incorporate dispersal and growth of a population can be helpful in teasing out what those effects are.

Reaction-diffusion equations have provided a good framework for such modeling efforts as they allow one to understand the effect that dispersal has on the population dynamics from a macroscopic perspective. Importantly, the reaction-diffusion framework allows one to understand when a population will persist and when it will become extinct. Classically, dispersal is represented by linear diffusion modeling random dispersal of individuals [102, 16], and two growth patterns that are typically studied with dispersal are logistic growth and an Allee effect. The Allee effect is a phenomenon in biology in which the density of a population affects the fitness of the individuals; if the population density falls below the Allee threshold, the per-capita growth rate becomes negative. It is known that the type of growth-pattern that a species is subject to also plays a key role in the population dynamics. For example, the Allee effect is observed in the fact that solutions to classical models with initial density below the Allee threshold will go extinct as time goes to infinity. An

important thing to note here is that in classical models, birth and dispersal are decoupled actions. This is a natural assumption to make in many circumstances, for example, when modeling mammals that are dispersing to hunt prey or to move from their birth site to breeding site. However, there are situations, such as birth jump processes, where dispersal and birth are inextricably linked.

In [48], a model for birth jump processes was introduced and was argued to be more suitable to model forest fire propagation due to a mechanism called spotting, where an ember from a fire can float in space and start another fire ahead of the front [69, 2]. It is shown that the inclusion of spotting in the model can lead to increased invasion speed of forest fire fronts. Birth jump processes have also been argued to be more accurate to describe cancer cell growth [12]. Cancer can metastasize due to cells transported through bodily fluids, thus growing tumors in distant locations, which is directly related to the birth of new cells [105]. To tease out the complicated effects of nonlocal dispersal, we develop theory for a model of birth-jump processes. We establish results on properties of solutions and global existence and uniqueness, and we are interested in determining under which initial conditions a population can persist or will go extinct. We pay particular attention to the question of whether nonlocal dispersal can help a population overcome the Allee effect.

Chapter 2

Nonlocal Mechanistic Models in Ecology

2.1   Introduction

We present and analyze a nonlocal mechanistic model that can be used to describe territory formation of social groups, without the need for artificial dynamics. However, due to the inclusion of nonlocal advection, classical theory no longer applies [13, 21]. Therefore, analyzing the model is difficult and solving it numerically is computationally expensive [9]. In order to investigate the behavior of solutions in two dimensions with several groups and connect the model with data, we must address these challenges. Specifically, we introduce a nonlocal RAD system for multiple-species, which helps maintain coherence of animal territories when there is no home center. We are concerned with studying the solutions of this model, with particular interest in those where the territories are segregated, as this is observed in many species.

We take advantage of the fact that this mechanistic model can be seen as a gradient flow of an energy (with respect to the Wasserstein metric, [106]), thus minimizers of the energy are equilibrium solutions of the mechanistic model. We first focus on the study of the nonlocal energy that contains convolution terms, which can be computationally expensive. In [111], the authors study a system of nonlocal PDEs modeling pattern formation in marshes. They use a local approximation to predict pattern formation in the nonlocal one-dimensional model which they explore numerically. This motivates our second objective, which is to derive local approximations of the original nonlocal model and provide a comparison of the energy landscapes. Here, we present both second and fourth-order approximations and determine that, in one-dimension, the second-order approximation does

a good job matching the minimizers of the nonlocal model only in a few cases. As we will see, the fourth-order local approximation matches the dynamics of the nonlocal model more widely. Moreover, in two-dimensions, the fourth-order approximation is required.

One objective is to understand how much faster (if at all) it is to find minimizers of the local energies compared to the nonlocal energy and how these savings scale with the number of species. The latter point is of particular importance, because in the model verification stage, when comparing to data, we will have to find equilibrium solutions of many groups (e.g. 6-10 depending on the application). When our algorithm was seeded with random data, we discover that the local approximations can lead to significant savings in computational time. However, with two groups, when starting data close to an energy minimizer was fed to the algorithm, the computation times were similar and in some occasions, the local approximation was slower than the original nonlocal energy. With three groups in two-dimensions, we observe an increased savings in computation time with the fourth-order approximation and random starting data. For some parameter values, we also see increased savings in computation time for segregated starting data. Moreover, for some starting data, the local and nonlocal algorithms find different energy minimizers. This can be attributed to the fact that the energy landscapes are complex (indeed there are an infinite number of equilibrium solutions, [95]). Note that we are often able to find a minimizer in the local approximation that matches the nonlocal minimizer provided we seed the nonlocal equilibrium to the local approximation. Incorporating an environmental potential alleviates this issue as the set of minimizers is reduced significantly. Of course, we still have non-uniqueness since for a given minimizer, if you swap populations, we obtain another minimizer. Moreover, if the environmental potential is radially symmetric, then the minimizers are invariant under rotations. Studying this case will highlight differences in segregation strength between the local and non-local models.

We find the energy landscapes to be quite complicated and difficult to compute efficiently. Thus, we shift to the use of a different method to numerically find solutions to the model. We work on a bounded, periodic grid and use spectral methods to compute the convolutions and derivatives in Fourier space. We investigate the effects the interaction potential, the environment,

the diffusion strength, and the number of groups have on the behavior of the equilibrium solutions and the computation time. Interestingly, we find some cases where changing the type of interaction potential has more of an effect on a population's territory than changing the variance. We also see that the balance between the diffusion strength and the aggregation strength seems to have a large influence in the computation times. Finally, with the intention of completing a similar analysis to [7] to determine which forces are primary drivers in the movement of meerkat social groups, we propose a method to connect the model with observed environment and meerkat location data. We test this method on synthetic data.

2.1.1   Application: Meerkat Territory Formation

As discussed, connecting mechanistic models of meerkat territory formation with data from field observations has been done in a local RAD framework [7]. The authors use various local RAD models to describe territories of social groups of meerkats, incorporating processes such as territorial scent marking and direct interactions between groups. They consider the model,

$$\partial_t u_i(x,t) = \nabla^2[u_i(x,t)D(x,t)] - \nabla \cdot [u_i(x,t)C_i(x,t)], \tag{2.1}$$

for $x \in \Omega \subseteq \mathbb{R}^d$, $t > 0$, where u_i represents social group with $i = 1...N$, $D(x,t)$ is the spatial diffusion rate, and $C_i(x,t)$ is the velocity of group i's directed movement. Each groups advects in the direction of $\hat{v}_i(x)$, a unit vector pointing in the direction of group i's home center. There are two core versions of this model: the groups either move away from direct interactions with conspecifics or away from scent markings by conspecifics. Within these core models, the authors can take into account both desirable and undesirable habitat features, social groups splitting, and territories shifting.

This model was connected with environment data and meerkat location data from the Kalahari Meerkat Project, a long term study of meerkat social groups in South Africa. The meerkat location data, seen in Figure 2.1(a), describes locations and times where members of meerkat social groups were observed, as well as occurrences of social groups splitting. Environment data such
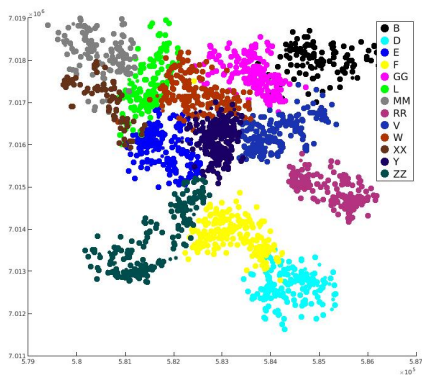
(a) Meerkat location data
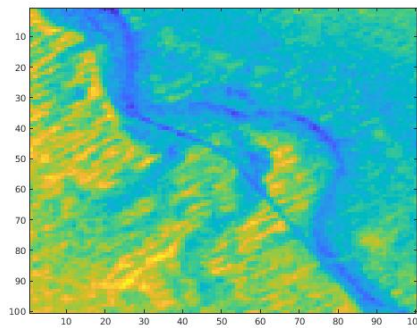
(b) Elevation data
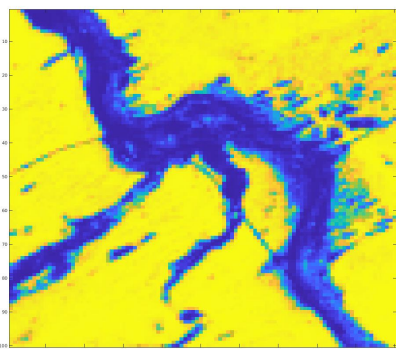
(c) Sand Data
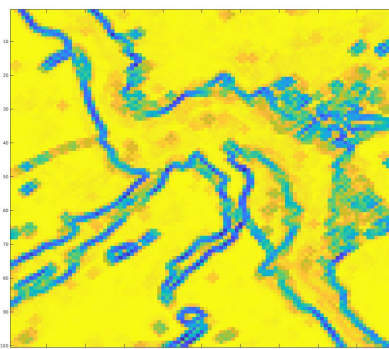
(d) Edge Data

Figure 2.1: Data from the same geographical location in South Africa: Meerkat location data from the Kalahari Meerkat Project and environment data rated from most attractive (yellow) to least attractive (blue) on a scale from 0 to 1.

as elevation (Figure 2.1(b)), sand-type (Figure 2.1(c)), and interface between sand-types (Figure 2.1(d)), were also considered in this study. For three different distinct time periods, the authors incorporate data into the various versions of equation (2.1) via maximum likelihood estimation, They determine which models are most accurate to the data during each period and hypothesize primary drivers of meerkat movement.

However, in the local system introduced to model the dynamics of territory use of meerkats, an advective term pointing in the direction of an artificial home center was introduced in order to keep different groups "coherent" (by coherence we mean the non-transient formation of spatially

non-constant distributions) [7]. The home center considered for each group is not observed in meerkat populations, and there is evidence that meerkats inform their territories based on nonlocal information. It has also been noted that a mechanistic model should be able to recreate observed behaviors without fixing a home center a priori [15]. As far as we are aware, the only other work that has tried to incorporate this spatial memory is [89].

2.1.2 Model and Methods

We propose a system of nonlocal reaction-advection-diffusion equations, which in its most general form reads as follows:

$$\begin{cases} \partial_t u_i = \eta \Delta A(u_i) - \nabla \cdot \left[u_i \nabla \left(K * u_i - K * \sum_{j=1, j \neq i}^N u_j + U(x,t) \right) \right], \\ u_i(x,0) = u_0(x), \end{cases} \tag{2.2}$$

for $x \in \Omega \subset \mathbb{R}^d, t > 0$, where $K * u(x) = \int_\Omega K(x-y)u(y,t)dy$. Here, u_i represents different competing groups, with $i = 1, 2, ..., N$. For this study we use periodic boundary conditions. A version of (2.2) was first introduced in [94] to understand social segregation. However, it can be seen as a generalization of the aggregation-diffusion equation for a single group, which has been the object of much research – see [60, 10, 8, 9] and reference within. Versions have also been studied in the $N = 2$ case, [37, 22], and this model has been used to study phenomena such as animal territories [90], predator-prey dynamics [38], and human gangs [6]. In [40], the authors investigate an efficient way to solve a multi-species model using spectral methods.

The dynamics of each group in (2.2) are governed by the competition between three forces: local diffusion (or short-range repulsion); long range intra-group attraction; and long-range inter-group repulsion. Social interactions and social groups are not exclusive to the human population, and certain animal populations also move and live in social groups, *e.g* deer, wolves, lions, and meerkats [108, 107, 7]. The different inter- and intra-forces which have been observed, or postulated to occur, between these social groups are the factors that we incorporate into (2.2). The function A in (2.2) represents the intragroup dispersal rate, the convolution term represents intra-group aggregation, and inter-group repulsion is governed by the potential K. Note that the long-range

aggregation term moves the group u_i with a nonlocal velocity $-\nabla K * u_i$, which helps maintain the group coherent. Moreover, the long-range, inter-group repulsion term moves the population u_i away from other groups via the velocity field $\sum_{j=1,j\neq i}^{N} \nabla K * u_j$ and serves as a *segregation term.*

System (2.2) can be seen as a gradient flow of the following energy with respect to the Wasserstein metric, which describes the distance between two probability distributions on a metric space. One can think about this metric as the cost it takes to transfer one measure to another in the most optimal way.

$$E[u_i](t) := \int_{\Omega} \left[\eta \sum_{i=1}^{N} A(u_i) - \frac{1}{2} \sum_{i=1}^{N} (K * u_i)u_i + \sum_{i,j=1,i\neq j}^{N} (K * u_i)u_j + \sum_{i=1}^{N} U(x,t)u_i \right] dx. \qquad (2.3)$$

Indeed, the first variations of the energy with respect to u_i are given by:

$$\frac{\delta E}{\delta u_i} = \eta \frac{\delta A}{\delta u_i}(u_i) - K * \left(u_i - \sum_{j=1,j\neq i}^{n} u_j \right) + U(x,t). \qquad (2.4)$$

We see that we can rewrite (2.2) as

$$\partial_t u_i = \nabla \cdot \left[u_i \nabla \left(\frac{\delta E}{\delta u_i} \right) \right], \qquad (2.5)$$

and write the time derivative of the energy using (2.5) and integration by parts,

$$\frac{dE}{dt} = \int_{\Omega} \left(\sum_{i=1}^{n} \frac{\delta E}{\delta u_i} u_{it} \right) dx$$

$$= -\int_{\Omega} \left(\sum_{i=1}^{n} u_i \left| \nabla \frac{\delta E}{\delta u_i} \right|^2 \right) dx. \qquad (2.6)$$

One of the motivations for this work lies in the fact that solving the evolution equation (2.2) is computationally expensive as explained in the work of Bernoff and Topaz in [9]. We recap their argument for convenience. For the two-dimensional problem, if we use quadrature, the nonlocal convolution runs in $O(n^4)$ time for an $n \times n$ grid, which can be decreased to $O(n^2 \log n)$ operations with the use of pseudospectral methods. However, solutions of (2.2) can have contact lines that develop from the degenerate diffusion (as will be illustrated in what follows – see for example Figure 2.3) and dealing with this then requires a finer grid, increasing the computational time.

In [9], Bernoff and Topaz considered a nonlocal biological aggregation diffusion equation and derived its local approximation (a Cahn-Hilliard type equation). Their goal was to determine if the minimizers of the energy functional stemming from the original nonlocal model did a reasonable job matching the minimizer of the energy stemming from the local approximation. We use the ideas introduced in that paper and generalize them to a system of nonlocal equations. That is, we explore the use of the energy (2.3) as a way of efficiently finding equilibrium solutions. We note a few differences between this work and that of [9]. First, we focus on studying systems, which are known to behave differently than scalar equations (indeed we see a much more complex energy landscape even with two groups). We also provide a comparison of computational costs between finding the minimizers to the nonlocal energy and the local counterparts.

To use the energy as a way to find equilibrium solutions to (2.2) we consider two possible strategies. First we focus on a specific potential, the Laplace potential, which lends itself to some useful analysis, in the context of this model. This reduces the complexity of the problem, enabling us to find explicit equilibrium solutions when two groups are interacting. In the more general case, finding equilibrium solutions reduces to solving boundary value problems with a convolution that can be solved efficiently. The second approach considers more general potentials for which we perform a long-wave approximation. As mentioned earlier, our aim is to see if the local models do a suitable job approximating the nonlocal model and if it is more efficient to find equilibrium solutions of the local models.

Finally, we consider spectral methods as an efficient way to compute equilibrium solutions. Similar to the work of [40], we compute convolutions and derivatives in Fourier space. In contrast, we find equilibrium solutions in two dimensions with $N > 2$ in order to incorporate data. We investigate the effect of parameters and potentials on the equilibrium solutions, demonstrate the effect of each of the terms in the model, and incorporate synthetic data by minimizing the negative log-likelihood function using stochastic gradient descent.

2.2   From interacting-particles to a population density

We begin considering n distinct groups of a species interacting with each other. For each of these groups, $i = 1, ..., n$, there are N_i individuals and $x_k^{N_i}(t)$ denotes the position of the kth member of group i at time t. We can describe the change in position of the individual as follows:

$$\frac{dx_k^{N_i}(t)}{dt} = v_k(x, t),$$

where the velocity is given by the various interactions. Specifically, it has the form:

$$v_k(x, t) = \sum_{j=1, j \neq k}^{N_i} \nabla V(x_k^{N_i}(t) - x_j^{N_i}(t)) + \sum_{l=1}^{n} \sum_{j=1}^{N_l} \nabla K(x_k^{N_i}(t) - x_j^{N_l}(t)) + \nabla U(x, t).$$

The potential V describes the intra-group interactions, long-range attraction and short range repulsion, K describes the inter-group interactions, a weak long range force, and U describes the favorability of the environment. If we take the limit as the members of each group go to infinity, one has to consider how these interactions will change with different numbers of particles in the system. The typical scalings considered are:

$$V_N(x) = N^{\gamma_v} V_1(N^{\gamma_v/d}(x)) \quad \text{and} \quad K_N(x) = N^{\gamma_k} K_1(N^{\gamma_k/d}(x)).$$

Where $\gamma_i \in (0, 1)$ leads to the range of interaction decreased and the strength increased, and $\gamma_i = 0$ leads to long-range but weak interactions. Therefore, in order to match the forces we want in our model, we choose $\gamma_v \in (0, 1)$ and $\gamma_k = 0$ [81, 80].

In the continuum limit we arrive at the following nonlocal model for each group u and v. The diffusion term, $A(u) = u^2$ in (2.2).

$$\partial_t u_i = \eta \Delta u_i^2 - \nabla \cdot \left[u_i \nabla \left(K * \left(u_i - \sum_{j=1, j \neq i}^{n} u_j \right) + U(x, t) \right) \right]. \tag{2.7}$$

A version of system (2.7) was used to study animal ecosystems with multiple groups in [89], where it is assumed that each population can detect opposing populations within a local neighborhood through direct observations or interactions, communication through scent marking, or memory of past interactions with opposing populations. Thus, in system (2.7) we are able to take into account the processes modeled in system (2.1), while eliminating the need for an artificial home center.

2.3   Second and fourth-order approximations

In this section we derive and analyze the second and fourth-order local approximation to (2.2). Note that for two groups, constants $u_1 = u_2 = c$ are equilibrium solutions to (2.2), when $U \equiv 0$. For three groups or more, the non-local problem has only the trivial solution as a spatially homogeneous solutions. However, for the local counterparts, all constants are equilibrium solutions when $U \equiv 0$. Through linear stability analysis of these constant equilibrium solutions, we find that both approximations lead to some parameter regimes of stability. The main objective of this stability analysis is not to determine if there are parameter regimes where one expects non-constant equilibrium solutions, but rather to make sure that the approximations are not ill-posed.

The second and fourth-order approximation of the system for groups $i = 1, ..., n$ is given by:

$$\partial_t u_i = \nabla \cdot \left[u_i \nabla \left(\omega u_i + \sum_{j=1, j \neq i}^n u_j + U(x,t) \right) \right]. \tag{2.8}$$

and

$$\partial_t u_i = \nabla \cdot \left[u_i \nabla \left(\omega u_i - \nabla^2 u_i + \sum_{j=1, j \neq i}^n (u_j + \nabla^2 u_j) + U(x,t) \right) \right], \tag{2.9}$$

respectively, with $\omega = 2\eta - 1$. Both approximations enjoy a gradient-flow structure with the following the respective energies:

$$E_{L2}[u_1, ..., u_n] := \int \left(\frac{\omega}{2} \sum_{i=1}^n u_i + \sum_{i,j,i \neq j}^n u_i u_j + \sum_{i=1}^n U(x,t) u_i \right) dx \tag{2.10}$$

$$E_L[u_1, ..., u_n] := \int \left(\frac{\omega}{2} \sum_{i=1}^n u_i^2 + \frac{1}{2} \sum_{i=1}^n |\nabla u_i^2| - \sum_{i,j,i \neq j} (\nabla u_i \cdot \nabla u_j - u_i u_j) + \sum_{i=1}^n U(x,t) u_i \right) dx. \tag{2.11}$$

In the remainder of the paper we work with interacting potentials $\mathcal{K}$ that satisfy the following assumptions:

(1) $\mathcal{K}$ is radial: $\mathcal{K}(x) = \mathcal{K}(|x|)$;

(2) $\mathcal{K} \in L^1(\mathbb{R}^d)$ with unit mass: $\int_{\mathbb{R}^d} \mathcal{K}(y) dy = 1$;

(3) $\mathcal{K}$ has sufficient decay as $|x| \to \infty$: defining

$$M_m := \frac{1}{m!} \int_{\mathbb{R}^d} \mathcal{K}(z) z^m dz;$$

we assume that $\lim_{m \to \infty} M_m = 0$ and $M_{m+1} = o(M_m)$;

(4) $\mathcal{K}$ has a normalized second moment $M_2 = 2d$.

2.3.1 Long-wave approximations

To obtain a local approximation to the nonlocal model, we perform long-wave approximation of the nonlocal term under the assumption for the interaction potential discussed above, exactly as found in [9], but details are included for the reader's convenience. The main thing to consider is that we can approximate the convolution term by first taking the Fourier Transform of the potential and keeping the long-wave modes. By assumption, $\mathcal{K}$ is radial and thus its Fourier Transform is also radial in k. We have

$$\hat{\mathcal{K}}(k) = \int_{R^n} \mathcal{K}(r) e^{-i\mathbf{k}\mathbf{x}} d\mathbf{x},$$

where $k = |\mathbf{k}|$ and $r = |\mathbf{x}|$. We rewrite the exponential in series form,

$$e^{-i\mathbf{k}\mathbf{x}} = \sum_{m=0}^{\infty} (-i)^m \frac{\mathbf{k} \cdot \mathbf{x}}{m!};$$

and obtain that:

$$\hat{\mathcal{K}}(k) = \int_{\mathbb{R}^d} \left(\mathcal{K}(r) - \mathcal{K}(r) i\mathbf{k} \cdot \mathbf{x} - \frac{1}{2} \mathcal{K}(r)(\mathbf{k} \cdot \mathbf{x})^2 + \cdots \right) d\mathbf{x}.$$

Using the assumptions on $\mathcal{K}$, we find the second and fourth terms to be zero due to symmetry, and the first term, $\int_{\mathbb{R}^d} \mathcal{K}(z) dz = 1$. For the third term, we have

$$-\frac{1}{2}\int_{\mathbb{R}^d}(\mathbf{k}\cdot\mathbf{x})^2K(r)d\mathbf{x}=-\frac{1}{2}\sum_{p=1}^{d}\sum_{q=1}^{d}k_pk_q\left[\int_{\mathbb{R}^d}\mathcal{K}(r)x_px_qd\mathbf{x}\right] \tag{2.12}$$

$$=-\frac{1}{2}\sum_{p=1}^{d}k_p^2\left[\int_{\mathbb{R}^d}\mathcal{K}(r)x_p^2d\mathbf{x}\right] \tag{2.13}$$

$$=-\frac{1}{2}\sum_{p=1}^{d}k_p^2\left[\frac{1}{d}\int_{\mathbb{R}^d}\mathcal{K}(r)r^2d\mathbf{x}\right] \tag{2.14}$$

$$=-\frac{1}{2}\frac{1}{d}2d\sum_{p=1}^{d}k_p^2 \tag{2.15}$$

$$=-k^2.$$

We rewrite $(\mathbf{k}\cdot\mathbf{x})^2$ as a double sum in the right hand side of (2.12), (2.13) uses symmetry to conclude that the non-diagonal terms cancel, (2.14) uses the radial symmetry of $\mathcal{K}$ to arrive at the second moment, and (2.15) substitutes in the assumption we have made for M_2. Finally, using the first three terms in the approximation, we get $\hat{\mathcal{K}}=1-k^2+O(k^4)$.

From this, we obtain second-order approximation by taking $\mathcal{K}*w\approx w$ and substituting this back into (2.7) to get (2.8). On the other hand, substituting $\mathcal{K}*w\approx w+\nabla^2w$ gives the fourth-order approximation seen in (2.9).

2.3.2   Stability analysis for the local approximations

To determine the viability of using these local approximations, we start by performing a stability analysis for both approximations when the number of groups interacting with each other is two or three. We find parameter regimes leading to stability for both approximations; however, as expected, the fourth-order approximation has a larger regime of stability. Of course, this comes at the cost of having more terms to deal with analytically and numerically. Thus, for the purpose of fast computations ideally one would prefer to work with a second-order approximation.

Proposition. *We obtain the following conditions to achieve linear stability for the local approximations, (2.8) and (2.9):*

(1) *The second-order approximation, (2.8), with $U = 0$, achieves linear stability for $n = 2$ and $n = 3$ when $\eta > 1$.*

(2) *The fourth-order approximation, (2.9), with $U = 0$, achieves linear stability for $n = 2$ when $\eta > 1/2$.*

(3) *The local approximations, (2.8) and (2.9), with $U \neq 0$ achieve linear stability for $n = 2$ when $\Delta U < 0$.*

The proof of this proposition relies on lemmas which we state and prove below.

2.3.3 Second-order approximation with no environment

We begin with the stability analysis of (2.8) for $n = 2$ and $n = 3$ with the following result:

Lemma 1. *Let $U = 0$. Then, (2.8) achieves linear stability for $n = 2$ and $n = 3$ when $\eta > 1$.*

Proof. Consider perturbations of the form $u = \bar{u} + \delta_u e^{ikx+\sigma t}$ and $v = \bar{v} + \delta_v e^{ikx+\sigma t}$.

The resulting linear system is:

$$
\sigma \begin{bmatrix} \delta_u \\ \delta_v \end{bmatrix} = \begin{bmatrix} -\omega\bar{u}k^2 & -\bar{u}k^2 \\ -\bar{v}k^2 & -\omega\bar{v}k^2 \end{bmatrix} \begin{bmatrix} \delta_u \\ \delta_v \end{bmatrix}.
$$

Note that the determinant of the matrix is $D = (\omega^2 - 1)\bar{u}\bar{v}k^4$ and it is positive when $\omega^2 - 1 > 0$ which corresponds to $\eta > 1$. The trace, $T = -\omega k^2(\bar{u} + \bar{v})$, is negative when $\omega > 0$, corresponding to $\eta > 1/2$. Therefore, for (2.8), we get linear stability for $\eta > 1$.

When $n = 3$, we substitute the perturbation of the constant solution, $w = \bar{w} + \delta_w e^{ikx+\sigma t}$ and linearize the system in the same manner. The resulting system is given by:

$$
\sigma \begin{bmatrix} \delta_u \\ \delta_v \\ \delta_w \end{bmatrix} = \begin{bmatrix} -\omega\bar{u}k^2 & -\bar{u}k^2 & -\bar{u}k^2 \\ -\bar{v}k^2 & -\omega\bar{v}k^2 & -\bar{v}k^2 \\ -\bar{w}k^2 & -\bar{w}k^2 & -\omega\bar{w}k^2 \end{bmatrix} \begin{bmatrix} \delta_u \\ \delta_v \\ \delta_w \end{bmatrix}.
$$

Here we can use the Routh-Hurwitz criterion, [97], to determine when the the eigenvalues are in the left half of the complex plane. We first find the characteristic equation,

$$p(\lambda) = -\lambda^3 - \omega k^2(\bar{u} + \bar{v} + \bar{w})\lambda^2 + k^4(\bar{v}\bar{w} + \bar{u}\bar{w} + \bar{u}\bar{v})(1 - \omega^2)\lambda + k^6\bar{u}\bar{v}\bar{w}(-2 + 3\omega - \omega^3).$$

From the characteristic equation, we obtain:

$$a_0 = k^6(\bar{u}\bar{v}\bar{w})(2 - 3\omega + \omega^3)$$

$$a_1 = -k^4(\bar{v}\bar{w} + \bar{u}\bar{w} + \bar{u}\bar{v})(1 - \omega^2)$$

$$a_2 = \omega k^2(\bar{u} + \bar{v} + \bar{w}).$$

We have linear stability when $a_0 > 0, a_2 > 0$, and $a_2 a_1 > a_0$. We first consider when $a_2 a_1 - a_0$ is greater than zero:

$$a_2 a_1 - a_0 = 2k^6\bar{u}\bar{v}\bar{w}(\omega^3 - 1) + k^6(\bar{u}^2(\bar{w} + \bar{v}) + \bar{v}^2(\bar{w} + \bar{u}) + \bar{w}^2(\bar{u} + \bar{v}))(\omega^3 - \omega).$$

We see the coefficients of $\omega^3 - 1$ and $\omega^3 - \omega$ are positive. We also have $\omega^3 - \omega$ and $\omega^3 - 1$ are positive when $\omega > 1$. This corresponds to $\eta > 1$. It is quick to check that $a_0, a_2 > 0$ when $\eta > 1$ as well. Therefore, the system is linearly stable for $\eta > 1$. □

Note that we can use the Routh-Hurwitz criterion for higher dimensional systems in order to determine stability for an artibrary number of groups.

2.3.4   Fourth-order approximation with no environment

Lemma 2. *Let $U = 0$ and $n = 2$. The fourth order approximation, (2.9), achieves linear stability when $\eta > 1/2$.*

Proof. For the fourth-order approximation, the corresponding linear system with two groups is:

$$\sigma \begin{bmatrix} \delta_u \\ \delta_v \end{bmatrix} = \begin{bmatrix} -k^2(\omega + k^2)\bar{u} & k^2(k^2 - 1)\bar{u} \\ k^2(k^2 - 1)\bar{v} & -k^2(\omega + k^2)\bar{v} \end{bmatrix} \begin{bmatrix} \delta_u \\ \delta_v \end{bmatrix}.$$

The determinant $D = k^4\bar{u}\bar{v}[(\omega + k^2)^2 - (k^2 - 1)^2]$ is positive if

$$(\omega + k^2)^2 > (k^2 - 1)^2, \quad \text{or} \quad (2\eta - 1 + k^2)^2 > (k^2 - 1)^2.$$

This is true if $\eta > 0$. For the trace, $T = -k^2(\bar{u} + \bar{v})(\omega + k^2)$, to be negative we need $\omega + k^2 > 0$, or $1 - 2\eta < k^2$. If $\eta > 1/2$, $1 - 2\eta$ is always negative, so it is less than k^2. For $\eta > 1/2$, we get linear stability. $\qquad \square$

Therefore, we see that the fourth-order approximation is stable for a larger region of η than the second-order approximation.

2.3.5   Stability with an environment term

For simplicity, we only consider the case with two interacting groups when adding an environmental potential U to our system.

Lemma 3. *Let $n = 2$ and $U \neq 0$. The local approximations, (2.8) and (2.9), achieve linear stability when $\Delta U < 0$.*

Proof. The equilibrium solutions are now $\bar{u} = 0$ and $\bar{v} = 0$. So, our perturbations are now simply $u = \delta_u e^{ikx+\sigma t}$ and $v = \delta_v e^{ikx+\sigma t}$. Substituting those into the system and keeping only linear terms in δ_u, δ_v both in the second and fourth-order approximations gives us the resulting system:

$$\sigma \begin{bmatrix} \delta_u \\ \delta_v \end{bmatrix} = \begin{bmatrix} ik\nabla U(x,t) + \Delta U(x,t) & 0 \\ 0 & ik\nabla U(x,t) + \Delta U(x,t) \end{bmatrix} \begin{bmatrix} \delta_u \\ \delta_v \end{bmatrix}.$$

With an environment potential, the only constant equilibrium solution is the trivial. Therefore, we obtain a simple diagonal matrix when we perturb them and keep linear terms. The eigenvalues are the diagonal entries. In order to have real part negative, we must have $\Delta U(x,t) < 0$. Therefore, we need the environment potential to be concave down for stability. $\qquad \square$

Now we are ready to prove Proposition 2.3.2.

Proof. (Proposition 2.3.2)

Combined, Lemma 1, Lemma 2, and Lemma 3 prove our result. $\qquad \square$

2.4 Equilibrium solutions for the Laplace potential

Strategically choosing certain potentials can help streamline the analysis of the system. To illustrate this, in this section we consider the Laplace potential, which is the Green's function of the Helmholtz equation. A nice consequence of this is that for two groups we obtain analytical equilibrium solutions to (2.2). This is not the case for n groups, but we do obtain a reduced model, a nonlocal boundary-value problem where the nonlocal term is the convolution. Recall that the Laplace potential, $\mathcal{K}(x) = \frac{1}{2m}e^{-m|x|}$, satisfies:

$$\mathcal{K}_{xx} - m^2\mathcal{K} = -\delta(x). \tag{2.16}$$

2.4.1 Two groups: $n = 2$

We consider two groups, denoted by u and v. Using the gradient-flow structure observed in (2.6), we can substitute (2.4) for both groups u and v and analyze the equilibrium solutions to obtain:

$$0 = -\int_{\mathbb{R}^d} \left(u \left| \nabla \frac{\delta E}{\delta u} \right|^2 + v \left| \nabla \frac{\delta E}{\delta v} \right|^2 \right) dx$$

$$= -\int_{\mathbb{R}^d} \left(u \left| \nabla(2\eta u - \mathcal{K} * (u - v)) \right|^2 + v \left| \nabla(2\eta v - \mathcal{K} * (v - u)) \right|^2 \right) dx.$$

Note that $u, v \geq 0$ are physical constraints on the solution we care about and thus the integrand above must be non-negative. This enforces that the integrand be zero, meaning that both terms in the integrand must vanish. Thus,

$$0 = u \left| \nabla(2\eta u - \mathcal{K} * (u - v)) \right|^2 = v \left| \nabla(2\eta v - \mathcal{K} * (v - u)) \right|^2.$$

From here, we deduce that $\nabla(2\eta u - \mathcal{K} * (u - v)) = \nabla(2\eta v - \mathcal{K} * (v - u)) = 0$, implying that:

$$2\eta u - \mathcal{K} * (u - v) = c_1 \tag{2.17}$$

$$2\eta v - \mathcal{K} * (v - u) = c_2 \tag{2.18}$$

where c_1, c_2 are constants. Solving for $u + v$ gives:

$$u + v = \frac{c_1 + c_2}{2\eta}. \tag{2.19}$$

Now hitting (2.17) with the operator $\partial_{xx} - m^2$ and recalling that $\mathcal{K}$ satisfies (2.16) allows us to compute as follows:

$$2\eta(u_{xx} - m^2 u) - \int_{\mathbb{R}} (\partial_{xx} - m^2)\mathcal{K}(x-y)(u(y) - v(y))dy = -m^2 c_1$$

$$2\eta(u_{xx} - m^2 u) + u(x) - v(x) = -m^2 c_1$$

$$2\eta(u_{xx} - m^2 u) + u(x) - \frac{c_1 + c_2}{2\eta} + u = -m^2 c_1$$

$$u_{xx} + (1/\eta - m^2)u = \frac{(1 - 2\eta m^2)c_1 + c_2}{4\eta^2} \qquad (2.20)$$

In the case when $\eta m^2 < 1$, we can solve this second-order differential equation explicitly.

$$u(x) = A\cos(\sqrt{1/\eta - m^2}\, x) + B\sin(\sqrt{1/\eta - m^2}\, x) + \frac{(1 - 2\eta m^2)c_1 + c_2}{4\eta^2(1/\eta - m^2)}.$$

Using the relation in (2.19), we can explicitly write v,

$$v(x) = \frac{c_1 + c_2}{2\eta} - A\cos(\sqrt{1/\eta - m^2}\, x) - B\sin(\sqrt{1/\eta - m^2}\, x) + \frac{(1 - 2\eta m^2)c_1 + c_2}{4\eta^2(1/\eta - m^2)}.$$

One of these analytical solutions is illustrated in Figure 2.2(a). We can consider how the restriction

(a)   (b)
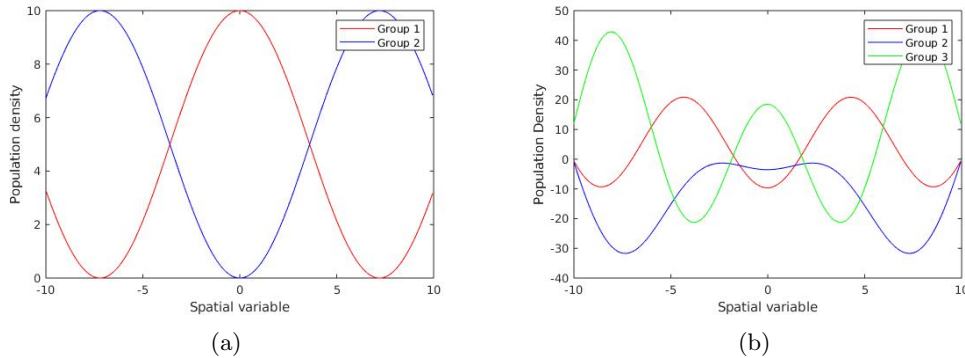
Figure 2.2: (a) Analytical solution to (2.20) with two groups interacting (b) The least squares solution to the linear system (2.22) with three groups.

$\eta m^2 < 1$ can be interpreted physically. Decreasing m leads to a steeper segregation potential, and increasing the parameter η increases the diffusion of the groups. Therefore, as we increase the steepness of the potential, we can allow for larger diffusion, or a group with smaller density. This suggests that if groups have a stronger repulsion from each other, they can take up more space.

As we decrease the steepness of the potential, we must have smaller diffusion, or higher mass for the group. Thus, if the groups are not as strongly repulsed from each other, they must take up less space. This interplay between these parameters suggests a balance that leads to the territory segregation we see in Figure 2.2(a).

2.4.2   General number of groups: $n > 2$

The nice cancellations that occurred in the above section do not happen in the more general case; however, we can still follow the procedure discussed above to reduce the system's complexity. Indeed, we obtain a system of ODEs that we can solve recursively for group $i = 1, ..., n$. We can use the symmetry of the system to get the remaining ODEs. An appropriate linear combination of (2.4), gives the following:

$$\sum_{i=2}^{n} u_i = (n-3)u_1 - \frac{n-2}{\eta}K * u_1 - \frac{n-3}{2\eta}c_1 + \frac{1}{2\eta}\sum_{i=2}^{n} c_i \tag{2.21}$$

If we hit (2.4) for $i = 1$ with the operator $\partial_{xx} - m^2$ and substitute in (2.21), we have the resulting ODE:

$$u_{1xx} - \left(m^2 + \frac{n-4}{2\eta}\right)u_1 + \frac{n-2}{2\eta^2}K * u_1 = \frac{(-2\eta m^2 - n + 3)c_1 + \sum_{i=2}^{n} c_i}{4\eta^2}. \tag{2.22}$$

The obvious algorithm to use for solving this ODE is the Fast Fourier Transform (FFT), [47]. Taking the Fourier Transform of (2.22) and solving for $\hat{u}_1$ gives that:

$$\hat{u}_1(w) = \frac{(2\eta m^2 - n + 3)c_1 + \sum_{i=2}^{n} c_i}{4\eta^2(-w^2 - (m^2 + \frac{n-4}{2\eta}) + \frac{n-2}{2\eta^2(1+w^2)})}\delta(\omega). \tag{2.23}$$

Therefore, in order to find u_1 and therefore u_i by symmetry, we need to find the inverse Fourier Transform of (2.23). Note that this returns the constant solution of the ODE. Recall that the boundary value problem is not unique. In fact, we get this same result using this method on the ODE obtained with two groups.

To obtain non-constant solutions, we discretize the domain and approximate u_{xx} with centered differences and approximate the convolution with the same matrix multiplication that we use in our numerical results in Section 2.5, reducing the problem to solving a linear system. Figure

2.2(b) illustrates a solution, while these solutions are negative in some values, the overall solution provides the territory boundaries when three groups are interacting in a one-dimensional space. In this case, we could interpret territory boundaries by shifting solutions above $y = 0$.

2.5 Energy minimizers for general potentials

To consider more general potentials we resort to computing the energy minimizers numerically, which we do through the use of fmincon from MatLab's optimization toolbox, computing the convolution via matrix multiplication using a equispaced grid, and computing derivatives using centered differences. We use the Laplace potential for each case, normalized to satisfy the assumptions put on our potential, $K(x) = -a_1 e^{a_2|x|}$, where $a_1 = \frac{\pi}{\Gamma(\frac{d+1}{8\pi})} \left(\frac{d+1}{8\pi}\right)^{d/2}$, $a_2 = \sqrt{\frac{d+1}{2}}$.

2.5.1 One-dimensional energy minimizers

For proof of concept we begin with the one-dimensional case. Our analysis begins with considering the interaction between two groups and we compare the local and nonlocal minimizers of their respective energies. Additionally, we contrast the computational time required for the algorithm to find the minimizers when seeded (1) random starting data and (2) segregated starting data (i.e. presumably close to what we believe to be a minimizer). The scaling of these computational times as we add more groups is very important for real world applications; hence, we also study what happens when we have three groups interacting. The final case we analyze in one-dimension is the addition of an environment potential.

2.5.1.1 Two groups interacting with no environmental influence

η	1/6	1/3	1/2	2/3	5/6
Nonlocal	78	153	78	33	23
Local-4th order	56	40	67	75	102

Table 2.1: Computational time in seconds for two groups interacting with no environmental influence and with a random starting data.

(a) $\eta = 1/3$ (b) $\eta = 1/2$
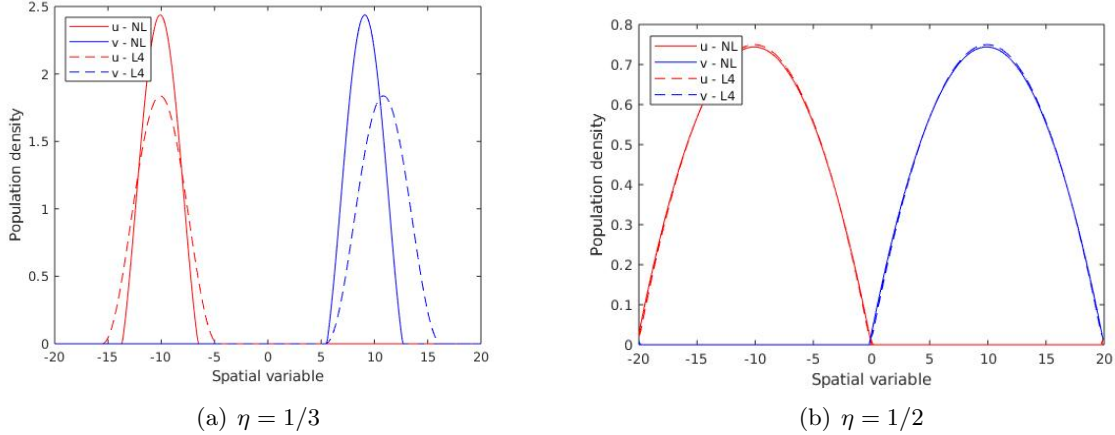
Figure 2.3: Energy minimizers for random starting data. NL refers to the non-local model and L4 to the 4th-order approximation.

(a) $\eta = 1/3$ (b) $\eta = 1/2$
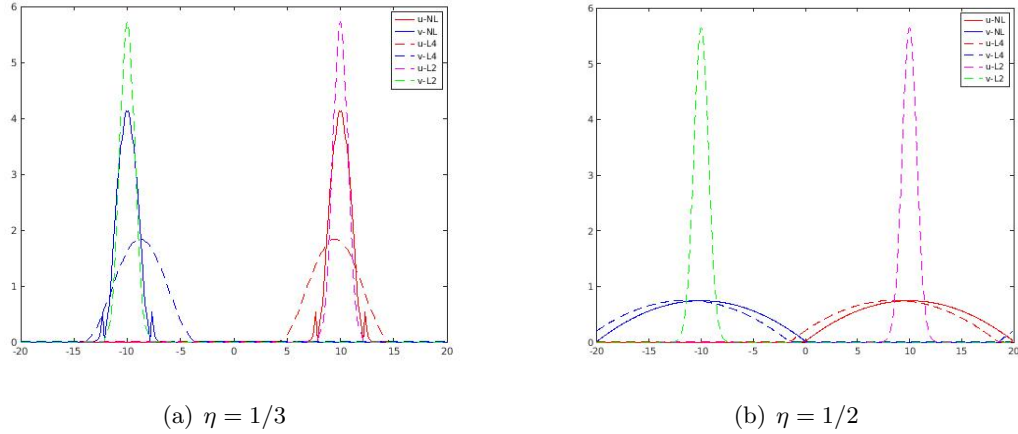
Figure 2.4: Energy minimizers for segregated starting data. NL refers to the non-local model, L2 and L4 to the 2nd-order and 4th-order approximations, respectively.

First, consider the case of two groups interacting with no environmental influence. From our analysis, for random starting data, we observe that the fourth-order local model is a better approximation to the nonlocal model in comparison to the second-order model. The second-order approximation either does not match the nonlocal model or is unstable, by which we mean that the algorithm did not return a reasonable minimizer. The latter was the case for the numerical experiments illustrated in Figure 2.3, which is the reason that results from the second-order approximation are not included. The results illustrated in Figure 2.3 are as expected: the two groups

form territories that are segregated, but have larger territories as η increases. For lower values of η, the minimizers for the fourth-order local energy tend to be shorter and wider than the minimizers for the nonlocal energy. Also note that as η increases, the fourth-order approximation does a better job matching the nonlocal equilibrium. A potential reason for this behavior is the desire to segregate is stronger in the nonlocal model than in the local counterpart. We observe that this difference diminishes as the two groups diffuse more and thus have less space to occupy (due to the boundedness of the domain), see Figure 2.3.

When seeding the minimizer algorithm with segregated data, we often find minimizers of higher energy as compared to the minimizers obtained when seeding the algorithm with random data. Recall that these energies are not convex and there are many local minimizers, which our algorithm will find depending on the data seeded. In fact, in all of our simulations, we found a minimizer of higher or equal energy when we seeded segregated data versus random data. This implies that we are more likely to get to a global minimizer if seeding the algorithms random data.

Comparing the nonlocal minimizers illustrated in Figures 2.3(a) and 2.4(a), we note that the former has lower energy than the latter. Also, the nonlocal minimizers illustrated in 2.3(b) and 2.4(b) have equal energy. In Figure 2.4, the minimizer of the nonlocal model is not a minimizer of the fourth-order approximation, but is a minimizer of the second-order approximation. Hence, there are rare cases where the second-order approximation matches the nonlocal and the fourth-order approximation does not.

We must also point out that in some cases, when the algorithm was initialized with segregated data, the minimizer of the fourth-order approximation did not match the nonlocal minimizer. However, this was never the case when seeded with random data. The second-order approximation matched in rare cases, but was unstable more often than not. For these reasons, we find the fourth-order approximation to be more suitable.

When comparing computational time, the fourth-order approximation performed at about the same level as the nonlocal counterpart, this is illustrated in Table 2.1. Thus, while the fourth-order approximation seems to be a suitable replacement for the nonlocal model, it does not save

computational time in one-dimension. Interestingly, for smaller values of η the local approximation was faster, but for larger values of η computing the minimizer for the nonlocal energy was faster. The computational times for segregated starting data are not shown in Table 2.1, because when feeding the algorithm a starting point close to an energy minimizer it takes at most two seconds for any of the models to find the minimizer. If the data seeded to the algorithm are not close to a minimizer, the results are similar to those with random starting points. In either case the fourth-order approximation does not really save computational time in the one-dimensional case with two-species interacting.

2.5.1.2   Three groups interacting with no environmental influence

η	1/6	1/3	1/2	2/3	5/6
Nonlocal - 2 Groups	78	153	78	33	23
Nonlocal - 3 Groups	563	1460	268	143	138

Table 2.2: Computation times in seconds for three groups with no environmental influence and random starting data.

Next, we look at energy minimizers when three groups interact with no environmental influence. When considering random starting data, in contrast to the previous case studied, both the fourth-order and the second-order approximation returned unstable results. Therefore, we only illustrate the nonlocal minimizers in Figure 2.5, where we observe intuitive results as we did with two groups.

For segregated starting data, the results for the nonlocal model and the second-order local approximation are very similar to the previous case. The fourth-order local approximation remains unstable. We see matches between the nonlocal and the second-order approximation in some cases, for example, for $\eta = 1/3$, as illustrated in Figure 2.6(a). In contrast, for $\eta = 2/3$, the starting data remains near a steady state for the second-order approximation, and is no longer a steady state for the nonlocal model. Therefore, the second-order approximation does not appear match the nonlocal model for the data seeded as η increases. Moreover, as in earlier cases, the energies

of the minimizers found with random starting data are lower than or equal to the energies found with segregated starting data.

We also analyze the computational expense incurred when adding a group to the nonlocal model. These times are displayed in Table 2.2. Adding a group significantly increases computational time, as we can see from the time differences shown in Table 2.2. The computational time for segregated starting data is not included, for the same reasoning as previously mentioned.

(a) $\eta = 1/3$ (b) $\eta = 2/3$
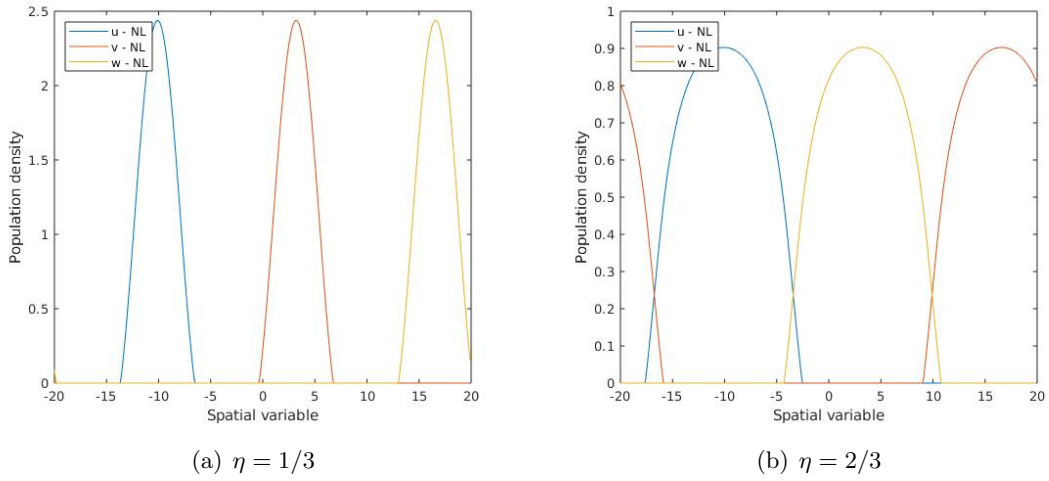
Figure 2.5: Minimizers for random starting data for the nonlocal model with different η values.

(a) $\eta = 1/3$ (b) $\eta = 1/2$
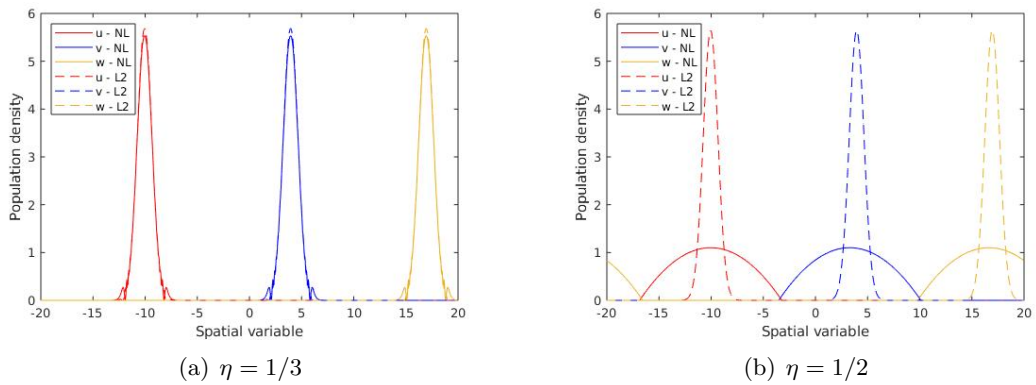
Figure 2.6: Minimizers for segregated starting data

(a) $\eta = 1/6$ (b) $\eta = 1/2$
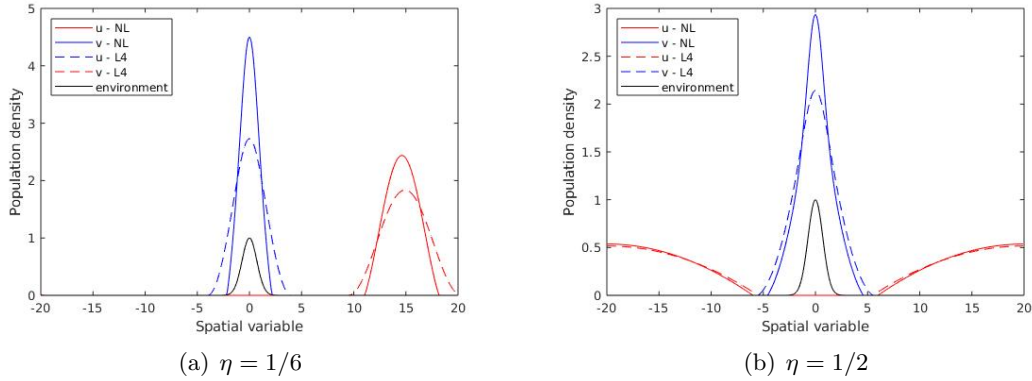
Figure 2.7: Minimizers of the nonlocal and the fourth-order approximation energy for random starting data.
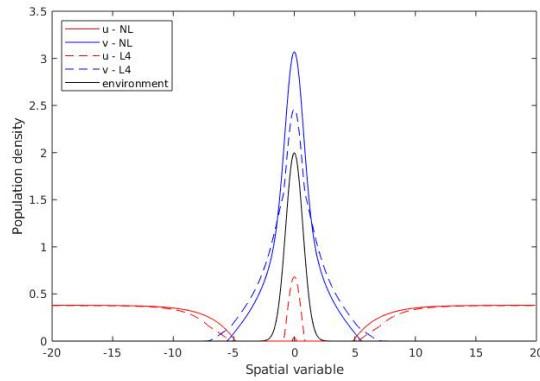
Figure 2.8: Minimizers of the nonlocal and fourth-order approximation energies with random starting data, $\eta = 2/3$, $a = 2$.

	Environment				No Environment			
η	1/6	1/3	1/2	2/3	1/6	1/3	1/2	2/3
Nonlocal	38	39	31	21	78	153	78	33
Local-4th order	51	42	53	69	56	40	67	75

Table 2.3: Computational times in seconds for two groups with an environmental influence and random starting data

2.5.1.3   Two groups interacting with an environmental influence

Finally, we investigate the effect of an environmental potential which influences the movement of all groups. With random starting data, as expected for the nonlocal model, if the influence of the

environmental potential is strong enough, it overpowers the desire for groups to segregate. However, there is some balance found between establishing a territory where groups see environmental benefits while being reasonably segregated. This balance is illustrated in Figure 2.7, where we have used the environmental potential $U = ae^{-x^2}$ with $a = 1$. the change of the environmental strength is done by changing the value of a.

For weak diffusion coefficients, as seen in Figure 2.7(a), one group tends to overpower regions that provide a good environment. The group that dominates depends on the seeded data (*i.e.* it is random if the seeded data is random). For larger values of η, the groups remain segregated but are closer and the second group is closer to the environment potential, illustrated in 2.7(b). Like the cases without the environment potential, the minimizers of the local energy were often shorter and wider for lower η values.

The environment potential also highlights some differences between the nonlocal model and local approximation that we have not seen previously. In Figure 2.8, the strength of the environment potential ($a = 2$) overpowered the segregation in the fourth-order local approximation: both groups have some claim to territory where the environment is beneficial, and their territories overlap. However, the desire to segregate remains strong in the nonlocal minimizers. In fact, only one group has established territory in regions where the environment is good and there is no territory overlap. Moreover, without the influence of an environment potential, higher η values diminished the differences in segregation between the local and nonlocal minimizers. On the other hand, with an environment potential, we observe the stronger sense of segregation in the nonlocal model for higher η values.

For segregated starting data, we obtain similar results to those seen when we considered no environmental influence. The second-order approximation matched local minimizers in limited cases, but was often unstable, and therefore is not displayed. The energy minimizers of the fourth-order approximation provide a reasonable match for most of the minimizers found using segregated data and matched the minimizers of lowest energy found. It produced stable results for a wide range of η values.

The computational times for two groups with an environmental influence are shown in the Table 2.3 for random initial data. We again omit the table for segregated starting data for the same reasons as the previous cases. The times suggest that the addition of the environment potential may, on average, slightly speed up the computation for a random starting data as compared to the results for two groups without the environmental potential. These are also listed in Table 2.3 for comparison. However, it is still clear that in one-dimension, the fourth-order approximation did not save computation time, and in many cases, it was more computationally expensive.

2.5.2   Two-dimensional energy minimizers

In this section, we perform an analysis which is analogous to that done in one-dimension. However, as two-dimensional domains are physical for many applications in spatial Ecology, the results from these sections are more relevant from the application perspective. When investigating both the second and fourth-order local approximations in two-dimensions, the results from the second-order approximation are not stable and we are forced to use the fourth-order approximation. Therefore, in this section we only analyze and compare the fourth-order local approximation to the nonlocal counterpart.

2.5.2.1   Two groups with no environmental influence

For two groups with no environmantal influence, we obtain results mirroring those seen in one-dimension. For random starting data, the local model matches the nonlocal model reasonably well, as we see in Figure 2.9. In some cases, like Figure 2.9, the minimizer of the local energy is slightly translated and has a larger territory than the nonlocal minimizer. This effect diminishes as η increases, just as we saw in one dimension.

For segregated starting data, we find that in many cases, the fourth-order local approximation matches the nonlocal model well. However, in some cases the nonlocal model returns a different minimizer than the local model. Just as we saw in one dimension, the nonlocal minimizers that do not match the local approximation, in each case, have been minimizers with a higher energy than

those found with random starting data.

When comparing computation time, we find differences between the one- dimensional and two-dimensional case. In two-dimensions, if the algorithm was fed random starting data, the local approximation terminated much faster than the nonlocal. This is likely because in one-dimension, we implement the convolution with an N x N matrix, but in two-dimensions, in order to implement the convolution, we use an N^2 x N^2 matrix, so the time complexity is much larger when we increase to two-dimensions. The computation time for random starting data can be found in Table 2.4. However, when fed starting data closer to a minimizer (i.e. segregated territories), the computation time was similar. There were cases ($\eta = 1/3$) where the local model terminated faster, but also cases when the nonlocal model terminated faster ($\eta = 1/2$). Some of these computation times are displayed in Table 2.4.

(a) Nonlocal group u (b) Nonlocal group v

(c) Local group u (d) Local group v
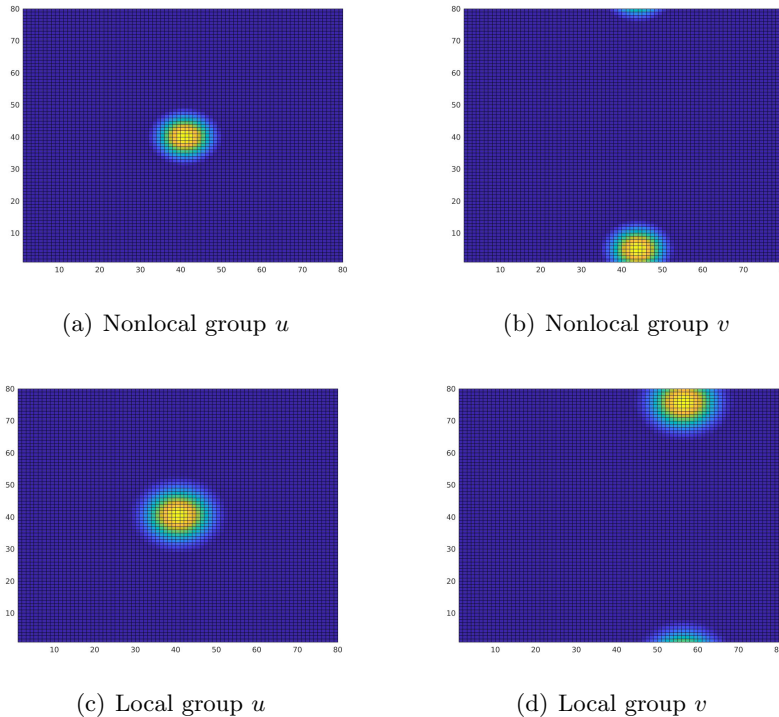
Figure 2.9: Energy minimizers for the local and nonlocal models with $\eta = 1/3$.

	Random Starting Data			Segregated Starting Data		
η	1/6	1/3	1/2	1/6	1/3	1/2
Nonlocal	> 600000	509988	> 600000	16	3121	767
Local	17202	45452	112098	13	24	5252

Table 2.4: Computational times (s) for two groups in two-dimensions.

2.5.2.2   Two groups with an environment potential

Here, we observe analogous results to the one-dimensional case when we include an environmental influence. Figure 2.10 illustrates results in two dimensions with environmental potential $U = e^{-\frac{1}{4}((x-20)^2+(y-30)^2)}$. This minimizer can be compared to the minimizer Figure 2.7, which illustrates results one-dimension. One group overpowers the territory where there are environmental benefits, and the other group crowds closely by while maintaining some segregation. As we have in one-dimension, the group that develops their territory with environmental benefits depends on the random starting data.

When comparing the nonlocal model and the local model, we also see results similar to those observed in one-dimension. At lower η values, we see that the nonlocal model often has higher population density, it retains more segregation than the local model. When η increases or the mass of the population increases, we see better matches if there is no environment term. However, with an environment term, the desire to be in environmentally beneficial locations overpowers the desire to segregate in the local model: the groups develop overlapping territories over beneficial environment. On the other hand, the desire to segregate remains strong in the nonlocal model. Figure 2.11 displays this discrepancy. It is enlightening to see what a possible cross-section of Figure 2.11 might look like by referencing the analogous one dimensional figure, Figure 2.8.

Similar to the results in one dimension, the computation time is sped up with an environment potential, but in two-dimensions, it is considerably faster than without an environment term. This can be seen in the differences in Table 2.4 and 2.5. It is also still the case that with random starting data, the local model terminates much faster than the nonlocal model.

(a) Nonlocal group u

(b) Nonlocal group v

(c) Local group u

(d) Local group v
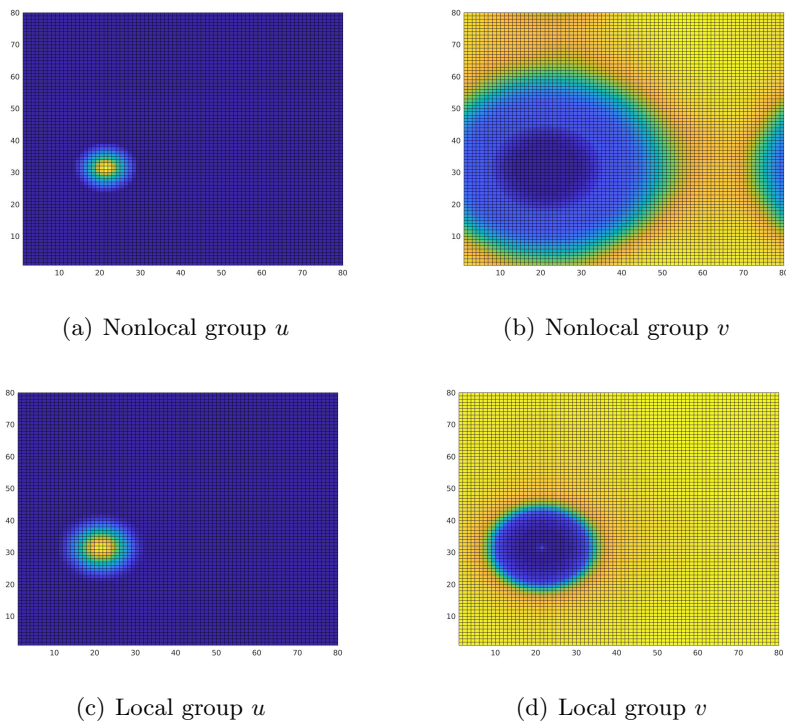
Figure 2.10: Energy minimizers for the local and nonlocal model with an environment potential with $\eta = 1/3$

η	$1/6$	$1/3$	$1/2$
Nonlocal	177161	84358	70929
Local	16613	14242	43122

Table 2.5: Computation times in seconds for two groups with an environment potential, random starting data

2.5.2.3 Three groups with no environmental influence

Finally, we found energy minimizers in two-dimensions with three groups. The computational expense it took to add a group in the nonlocal model in two-dimensions with random starting data was too great for the algorithm and our resources, although we were able to get results with segregated starting data. We found interesting results when comparing to two groups in two-dimensions. In the cases where the local model was a reasonable match for the nonlocal, lower values of η, we observed the local model terminated much faster given the same starting data. So, with the trials we ran, the local model saved computation time irrespective of whether the starting

(a) Nonlocal group u

(b) Nonlocal group v

(c) Local group u

(d) Local group v
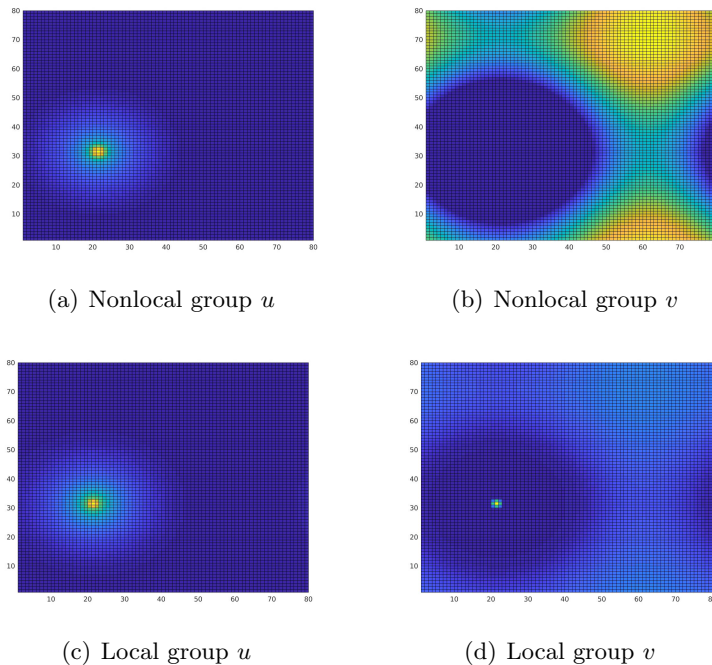
Figure 2.11: Energy minimizers for the nonlocal model and local approximation with an environment potential, $\eta = 1/2$

(a) Group u - NL

(b) Group v - NL

(c) Group w - NL

(d) Group u - L4

(e) Group v - L4

(f) Group w - L4
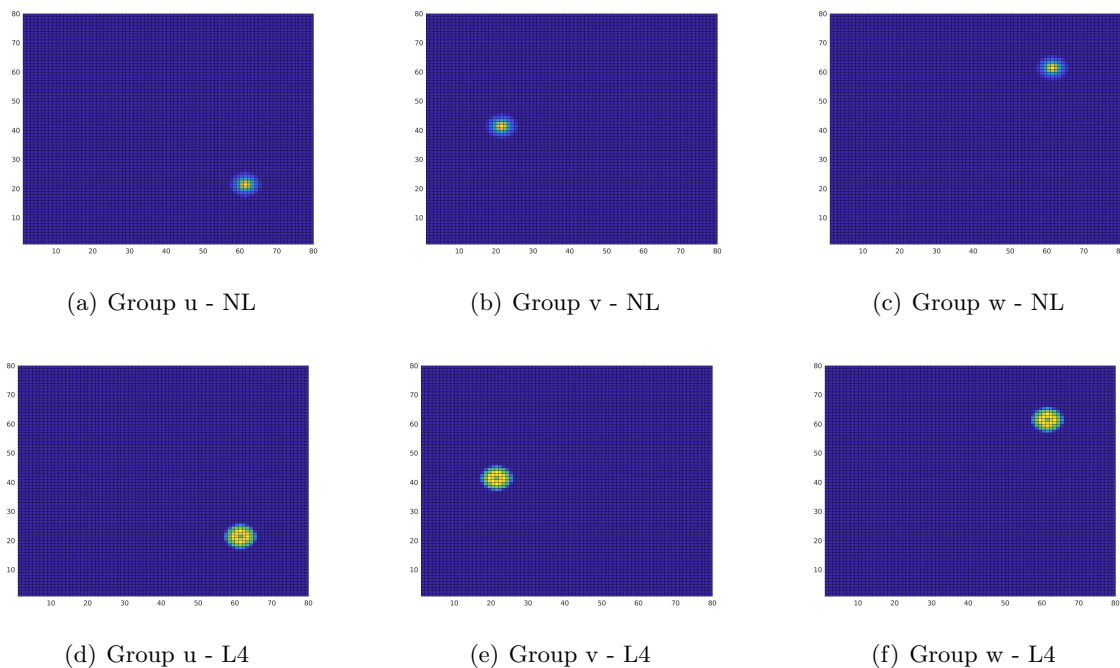
Figure 2.12: Energy minimizer for three groups with a segregated starting point for both the nonlocal and local model and $\eta = 1/3$.

data was random or segregated. However, we still observe that the local approximation did not match the nonlocal model well in every case with segregated data and returned unstable results in some cases. Figure 2.12 illustrates a reasonable match between the minimizers of the nonlocal model and its fourth-order approximation. Note that the local minimizers are more concentrated than their local approximations.

2.6   Numerical Solutions via Spectral Methods

In this section, we solve System (2.7) using spectral methods. We are able to investigate how the parameters, potentials, and terms in the model affect the behavior of equilibrium solutions and are also able to use this method to incorporate synthetic data into the model.

2.6.1   Discretization Scheme

We outline the process to numerically find equilibrium solutions of System (2.7). We take advantage of working with a bounded, periodic grid and use the Fast Fourier Transform to move to frequency space, compute derivatives and convolutions, and use the Inverse Fast Fourier Transform to move back to physical space. This process gives us a discrete representation of the right hand side of our system, which allows us to discretize in time and numerically solve the system.

Consider the Fourier Transform,

$$\hat{u}(x) = \int_{-\infty}^{\infty} u(x)e^{-2\pi i k x}dx, \;\; k \in \mathbb{R}.$$

Because we are solving a nonlocal system of PDEs, we must address computing convolutions and derivatives efficiently. Therefore, there we employ two convenient properties of the Fourier Transform in our computations:

$$\widehat{f'}(x) = ik\widehat{f}(x) \tag{2.24}$$

$$\widehat{K * f}(x) = \widehat{K}(x)\widehat{f}(x). \tag{2.25}$$

However, we are working on a bounded, periodic grid. Thus, we compute derivatives and convolutions in frequency space using the Discrete Fourier Transform (DFT),

$$\hat{v}_k = h \sum_{j=1}^{N} v_j e^{-ikx_j}, \ \ k \in -\frac{N}{2} + 1, ..., \frac{N}{2}, \tag{2.26}$$

which allows us to pass into frequency space. The Inverse Discrete Fourier Transform (IDFT),

$$v_j = \frac{1}{2\pi} \sum_{k=-N/2+1}^{N/2} \hat{v}_k e^{ikx_j}, \ \ j \in 1, ..., N, \tag{2.27}$$

allows us to return to physical space. We utilize equation (2.26) to move into the Fourier domain, we use properties (2.24) and (2.25) to compute derivatives and convolutions in Fourier space, and use (2.27) to move back to physical space. In fact, we make use of the Fast Fourier Transform (FFT) and Inverse Fast Fourier Transform (IFFT) in order to move in and out of frequency space efficiently, reducing number of operations from N^2 to $N \log N$.

We first compute the right hand side of System (2.7) on the bounded, periodic grid for $t = n\Delta t$. Let $u_{mj}^{i,n}$ be the value of u at time $n\Delta t$ for group $i \in \{1, ..., M\}$ at grid point (m, j) for $m, j \in \{1, ..., N\}$, and let $\hat{u}_{k\ell}^{i,n}$ represent the DFT for $k, \ell \in \{-N/2 + 1, ..., N/2\}$. We begin by using the FFT to move into Fourier space to determine $\hat{u}_{k\ell}^{i,n}$, $\hat{K}$, and $\hat{U}$. We compute the nonlocal terms in System (2.7) by multiplying $\hat{u}_{k\ell}^{i,n}$ and $\hat{K}$ for each group i, utilizing the property in equation (2.25). We remain in Fourier space to compute the gradient of the nonlocal terms and $U(x, t)$, using the property in equation (2.24). We then use the IFFT to return the physical domain and multiply these terms by u. We move back into frequency space in order to compute derivatives. Finally, we take the IFFT to move back to physical space. This gives us a discrete representation of the right hand side for group i at time $t = n\Delta t$,

$$\partial_t u^{i,n} = f(u^{i,n}), i = 1, ..., M, \tag{2.28}$$

where f is the function described above. To find equilibrium solutions, we either solve (2.28) with $\partial_t u^{i,n} = 0$ for $i = 1...M$, or we time step. One can use equation 2.28 and an ODE solver to find $u^{i+1,n}$. In particular, we use a Runge Kutta method in Matlab.

After solving for the equilibrium solution or between time steps, we mitigate error by following two processes as done in [7]. First, we set all negative entries for $u_{m,j}^{i,n}$ equal to zero. Second, we approximate the mass of each group,

$$M_i^n = \sum_{m,j=1}^{N} \frac{1}{4}(u_{m,j}^{i,n} + u_{m,j+1}^{i,n} + u_{m+1,j}^{i,n} + u_{m+1,j+1}^{i,n})\Delta x \Delta y,$$

and divide $u^{i,n}$ by M_i^n to maintain a mass of 1. Note that when m or $j = N$, we use periodicity in u. We determine error at time $n\Delta t$ by computing the the L^2 norm of $f(u^{i,n})$ for for $i = 1...M$. For an equilibrium solution, this value should be zero. We continue time-stepping until this value is below a chosen tolerance.

We explore acceptable error tolerances by exploring the differences in equilibrium solutuions. For example, in one instance, decreasing the error tolerance from .025 to .001 produced similar territories with one having a slightly larger maximum density than the other. However, the computation time increased from 15 seconds to 125. Therefore, we must find an acceptable balance in the differences in territory predictions with the computational expense of reducing error.

2.6.2 The Effect of Potentials on the Behavior of Equilibrium Solutions

In this section, we investigate how the terms, parameters, and potentials in our model affect the territory formation of social groups and how the computation time scales as we increase the number of groups. The former allows us to determine how changing the shape of the interaction potential and the environment potential changes the behavior of solutions, which can help inform how one may choose potentials going forward. The latter is of particular importance in application, as the meerkat location data we are interested in incorporating into the model includes thirteen social groups. We solve for equilibrium solutions using the methods described in section 2.6.1 while varying the parameters and potentials used.

In our simulations, we use parameters η, a, and b, where η is the strength of diffusivity shown in system 2.7, and a and b are constants multiplied by $U(x, y)$ and $K(x, y)$, respectively. We refer to these as the environment and interaction potential strength. We also vary the shape of the

environment potential and the interaction potential. In most simulations, the environment potential used is $U(x, y) = A \exp(-.1x^2 - .1y^2)$. However, when varying the shape of the environment potential, we also use a Laplace potential, $U(x, y) = A \exp(-\sqrt{\frac{3}{2}}|\mathbf{x}|)$. In both cases, A is found to normalize U so the maximum value is one. Therefore, the most attractive environment has a value of one, and a less attractive environment, or neutral environment, has a value of zero. We also use various interaction potentials. Typically, the interaction potential used is the Laplace potential as described above. However, A is found so that K integrates to one over the domain. When investigating how the shape of the interaction potential changes the equilibirum solutions, we also use a Gaussian potential, $K(x, y) = A \exp(-\frac{x^2}{2\sigma^2} - \frac{y^2}{2\sigma^2})$, where we change the variance, σ, and A is chosen so that K integrates to one over the domain. Finally, we also consider a Morse Potential, $K(x, y) = 2 \exp(-c(x^2 + y^2 - r)) - \exp(-2c(x^2 + y^2 - r))$. This allows us to consider a larger range of b and η values, as the Morse potential repels a population at close distances. Therefore, a higher b value does not need a higher η value to balance it. In all of these simulations, we are computing equilibrium solutions over a 100x100 grid. This is due to the fact that this is the resolution of the data we intend to incorporate into our model.

2.6.2.1   Equilibrium Solutions $N = 1$

We begin with a simple case– one group in two dimensions. This allows us to investigate how the behavior of the solutions changes as our potentials and parameters change. We investigate the strength of diffusion, η, the strength and shape of the interaction potential, K, and the strength and shape of the environment potential, $U(x, y)$.

In System (2.7), the parameter η affects the strength of diffusivity within a group. While the nonlocal term $K * u$ is aggregating the group, η balances this aggregation by imposing diffusion. The interplay between these two terms helps to determine the area and population density of a group's territory. For this reason, we would expect as we increase η and keep other parameters constant, the territory a group occupies increases and the population density decreases. Figure 2.13 shows an example of how a solution changes when the diffusion strength, η, is varied and

(a) $u(\mathbf{x}, \infty)$, $\eta = 3$ (b) $u(\mathbf{x}, \infty)$, $\eta = 5$ (c) $u(\mathbf{x}, \infty)$, $\eta = 7$

(d) $u(\mathbf{x}, \infty)$, $U(\mathbf{x})$, $\eta = 3$ (e) $u(\mathbf{x}, \infty)$, $U(\mathbf{x})$, $\eta = 5$ (f) $u(\mathbf{x}, \infty)$, $U(\mathbf{x})$, $\eta = 7$
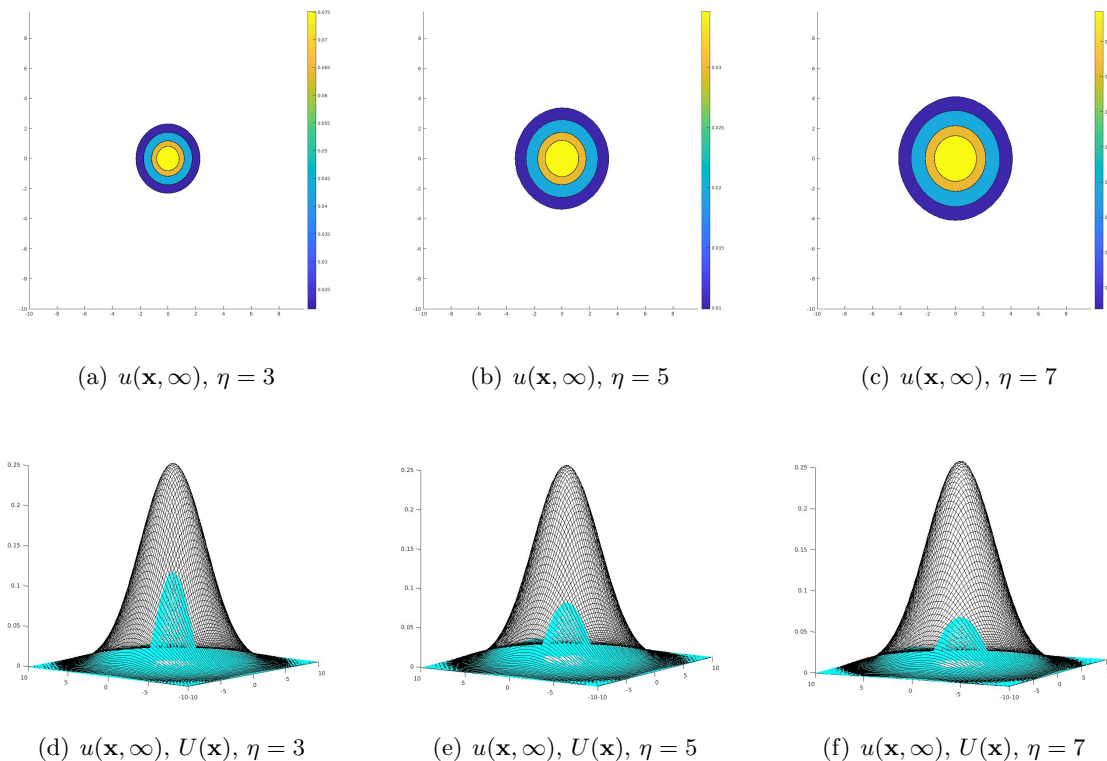
Figure 2.13: Equilibrium solutionsto (2.7) for $a = .25$, $b = .25$, and varied η, shown as a contour plot (top), and a three-dimensional plot with $U(\mathbf{x})$ in black (bottom).

the environment strength and the interaction potential strength remain constant. Each column of figures shows one simulation for a value of η; the top figure is a contour plot of u and the bottom figure is a three-dimensional plot of u and $U(x, y)$. The difference in territory size as η increases is apparent in Figure 2.13(a), 2.13(b), and 2.13(c). As we would expect, the territory size increases with η, and the population density decreases. The change in population density is more apparent in Figure 2.13(d), 2.13(e), and 2.13(f), because the population density in relation to U is shown. As η increases, the population spreads out to territory with a less attractive environment and therefore population density decreases.

When we investigate the interaction potential, we consider both the strength of the interaction potential, b, and the shape of the interaction potential. Therefore, we perform simulations changing the value of b and simulations with different functions, $K(x, y)$. Because K controls aggregation

(a) $u(\mathbf{x}, \infty)$, $b = .25$ (b) $u(\mathbf{x}, \infty)$, $b = .5$ (c) $u(\mathbf{x}, \infty)$, $b = 1$

(d) $u(\mathbf{x}, \infty)$, $U(\mathbf{x})$, $b = .25$ (e) $u(\mathbf{x}, \infty)$, $U(\mathbf{x})$, $b = .5$ (f) $u(\mathbf{x}, \infty)$, $U(\mathbf{x})$, $b = 1$
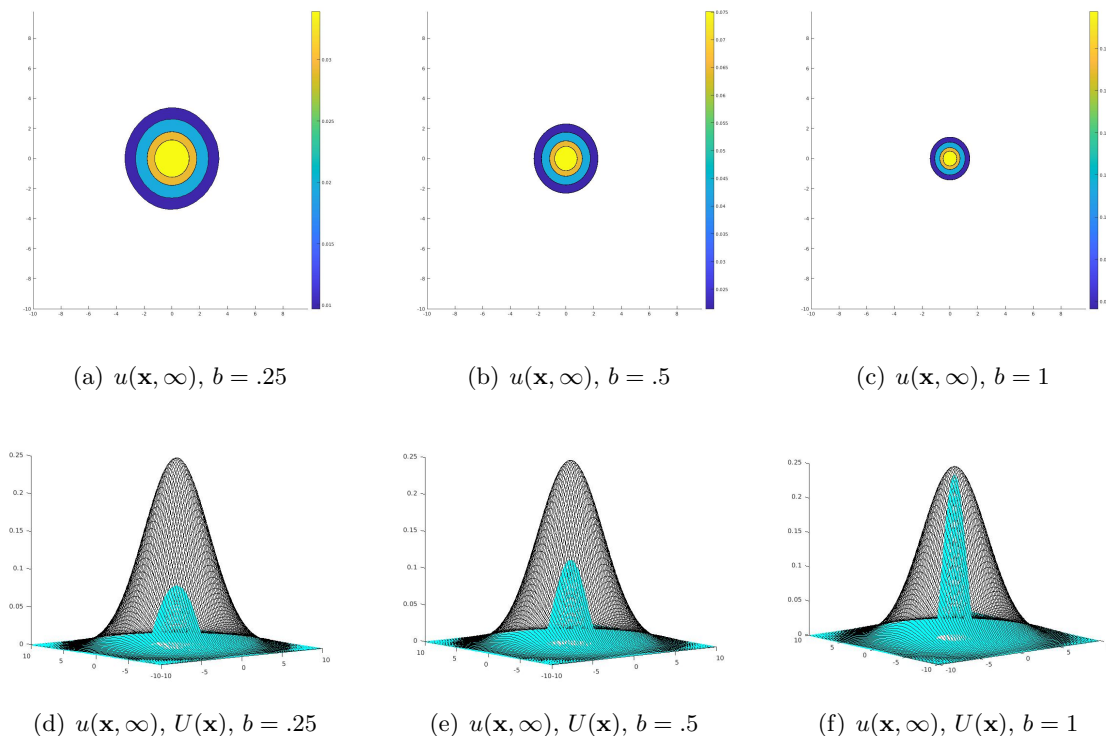
Figure 2.14: Equilibrium solutions to (2.7) with $a = .25$ and $\eta = 3$, and varied b, shown as a contour plot (top), and a three-dimensional plot with $U(\mathbf{x})$ in black (bottom).

within a group, we are looking to see how aggregation changes as we change the shape and strength of K. It is important to note that the repulsion between groups would also be affected when $N > 1$, which we investigate in Section 2.6.2.2.

Figure 2.14 illustrates how the strength of the interaction potential changes the behavior of the solution. In this simulation, the interaction potential is the Laplace potential. The diffusion strength and environment strength are kept constant. As with the previous case, each column is a simulation for a different value of b and each row is a different plot of the same simulation. We would expect as we increase the strength of the interaction potential, b, the aggregation within a group will increase and the size of the group's territory decreases. This behavior is demonstrated in Figure 2.14(a), 2.14(b), and 2.14(c); the area the group occupies in Figure 2.14(c) is much smaller than in Figure 2.14(a). The increase in population density as K increases is more apparent in Figure 2.14(d), 2.14(e), and 2.14(f). When $b = 1$, as in 2.14(f), the population density is much

(a) $u(\mathbf{x}, \infty)$

(b) $u(\mathbf{x}, \infty)$

(c) $u(\mathbf{x}, \infty)$

(d) $u(\mathbf{x}, \infty)$ and $U(\mathbf{x})$

(e) $u(\mathbf{x}, \infty)$ and $U(\mathbf{x})$

(f) $u(\mathbf{x}, \infty)$ and $U(\mathbf{x})$

(g) $K(x, y)$, $\sigma = 2$

(h) $K(x, y)$,$\sigma = .5$

(i) K Laplace

Figure 2.15: Equilibrium solutions to (2.7) for $a = .25$, $\eta = 3$ and $b = 1$ and varied K, shown as a contour plot (top), a three-dimensional plot with $U(\mathbf{x})$ in black (middle), and the respective potentials $K(x, y)$ (bottom).

higher than when $b = .25$, in Figure 2.14(d).

Next, we consider how the shape of the interaction potential changes the behavior of the solution. We use the same interaction potential from Figure 2.14, and compare the behavior of the equilibrium solutions to solutions with a Gaussian as the interaction potential. We vary σ to determine how the solution changes. The environment and η are kept constant. Figure 2.15 compares the equilibrium solutions from these different interaction potentials. The first two rows are similar to previous simulations, with the bottom row depicting a three-dimensional plot of the interaction potential used. Figure 2.15(g) and Figure 2.15(h) are Gaussian potentials with $\sigma = 2$ and

$\sigma = .5$, respectively. Figure 2.15(i) is the Laplace potential. When comparing the simulations using the potentials with different values of σ, it is interesting to note that although K is qualitatively quite different in Figure 2.15(g) and 2.15(h), the predicted territory and population density are quite similar, with the population density in Figure 2.15(h) being slightly higher. Although K in Figure 2.15(h) and 2.15(i) qualitatively look most similar, the difference in equilibrium solutions is most drastic when we shift K from the Gaussian to the Laplace Potential. In Figure 2.15(c) and 2.15(f), the population density is much higher and the territory is smaller than in the simulations with K Gaussian.

We also consider a Morse potential for K. The motivation for this is drawn from the interplay between η and the strength of K. If K is stronger, η must be larger to balance out the aggregation within a group. This needed balance is reflected in the stability of our numerical simulations. If K is too strong and η is too small, our numerical methods take much longer to find an equilibrium solution with the requested tolerance, if the simulation terminates at all. This phenomena is addressed later in this section when we consider multiple groups and the scaling of computation time. However, with the Morse potential, there is repulsion within a group at shorter distances, and aggregation at longer distances. Therefore, the balance between diffusion and aggregation is encapsulated in K. We completed simulations with a constant, varying b and η, for both K as the Laplace potential and K as the Morse potential. We determined a viable range of η in our numerical simulations for each b value. When K was the Laplace potential, there was a lower bound for stable η values. However, for the Morse potential, we could set $\eta = 0$ and incorporate both the diffusion and aggregation in K. This is depicted with multiple groups where we have different potentials for aggregations and segregation in Section 2.6.2.2.

Finally, we investigate the influence of the strength of the environment potential, a, and the shape of the environment potential. An illustration of the effects of shape and strength are demonstrated in Figure 2.17 and 2.16. Figure 2.16 shows simulations with the same $U(x, y)$ from previous simulations. Each column in these two rows is one simulation with different a values and the same two plots as previous simulations. Figure 2.17 shows simulations with a Laplace potential

(a) $u(\mathbf{x},\infty)$, $U(\mathbf{x})$, $a = .25$ (b) $u(\mathbf{x},\infty)$, $U(\mathbf{x})$, $a = .5$ (c) $u(\mathbf{x},\infty)$, $U(\mathbf{x})$, $a = 1$

(d) $u(\mathbf{x},\infty)$, $a = .25$ (e) $u(\mathbf{x},\infty)$, $a = .5$ (f) $u(\mathbf{x},\infty)$, $a = 1$
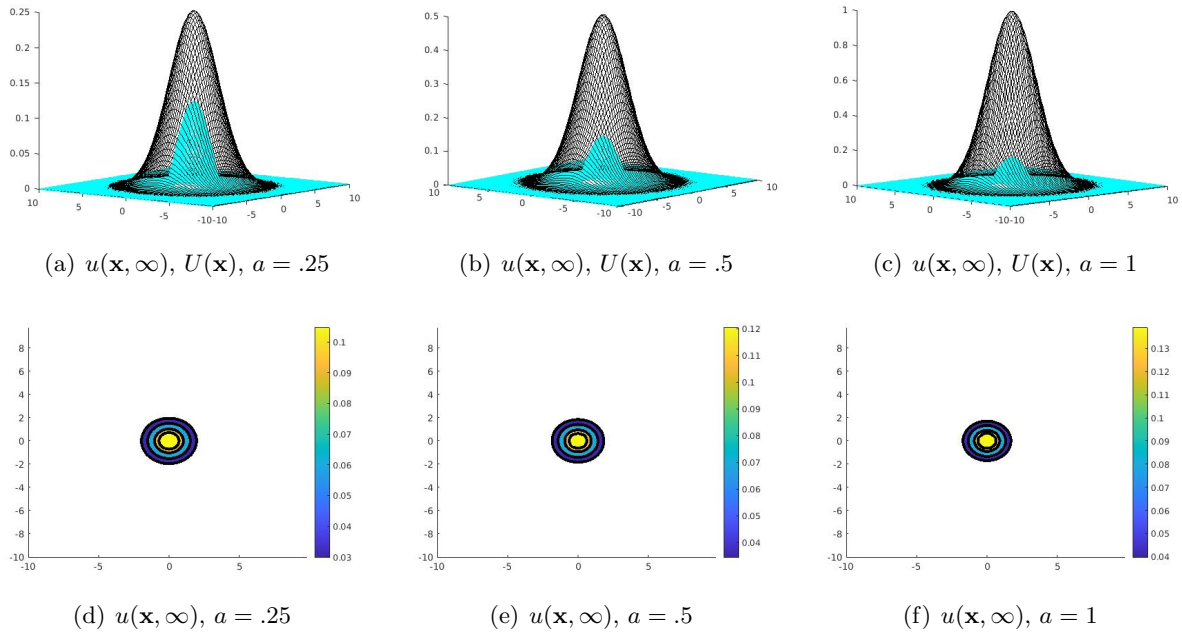
Figure 2.16: Equilibrium solutions for $\eta = 3$, $b = .5$, and varied a, shown as a three-dimensional plot with $U(\mathbf{x})$ in black (top), and a contour plot (bottom).

(a) $u(\mathbf{x},\infty)$, $U(\mathbf{x})$, $a = .25$ (b) $u(\mathbf{x},\infty)$, $U(\mathbf{x})$, $a = .5$ (c) $u(\mathbf{x},\infty)$, $U(\mathbf{x})$, $a = 1$

(d) $u(\mathbf{x},\infty)$, $a = .25$ (e) $u(\mathbf{x},\infty)$, $a = .5$ (f) $u(\mathbf{x},\infty)$, $a = 1$
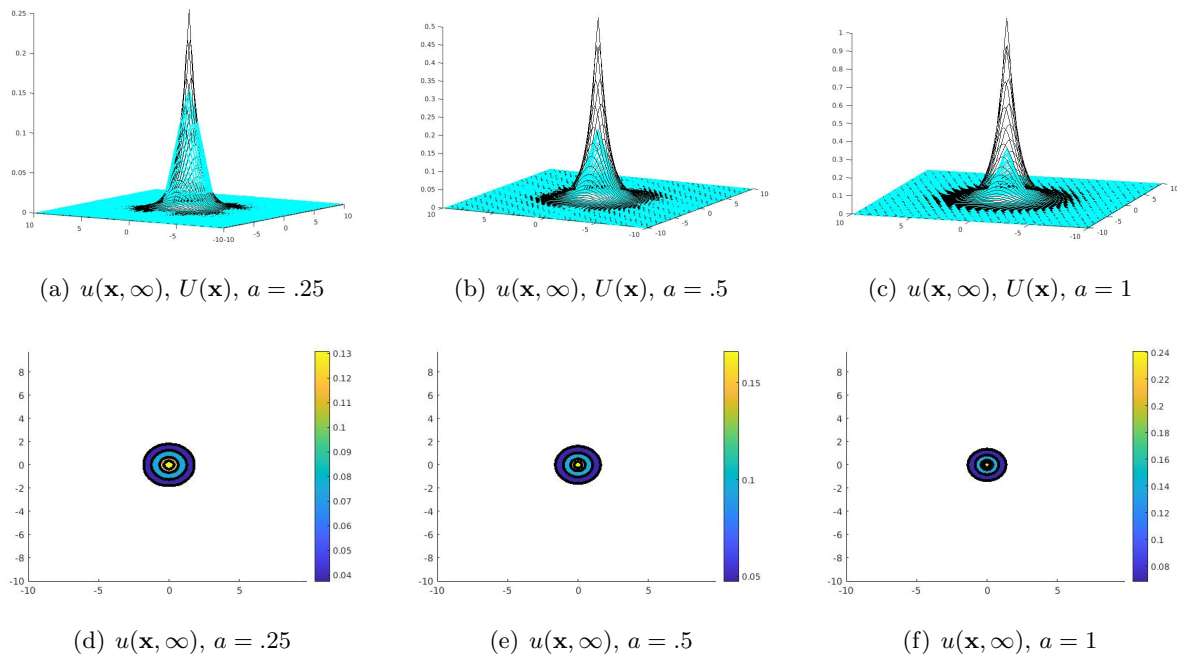
Figure 2.17: Equilibrium solution to (2.7) for $\eta = 3$, $b = .5$, and varied a, shown as a three-dimensional plot with $U(\mathbf{x})$ in black (top), and a contour plot (bottom).

(a) $u(\mathbf{x}, \infty)$, $a = .5$

(b) $u(\mathbf{x}, \infty)$, $a = .25$

(c) $u(\mathbf{x}, \infty)$, $U(\mathbf{x})$, $a = .5$
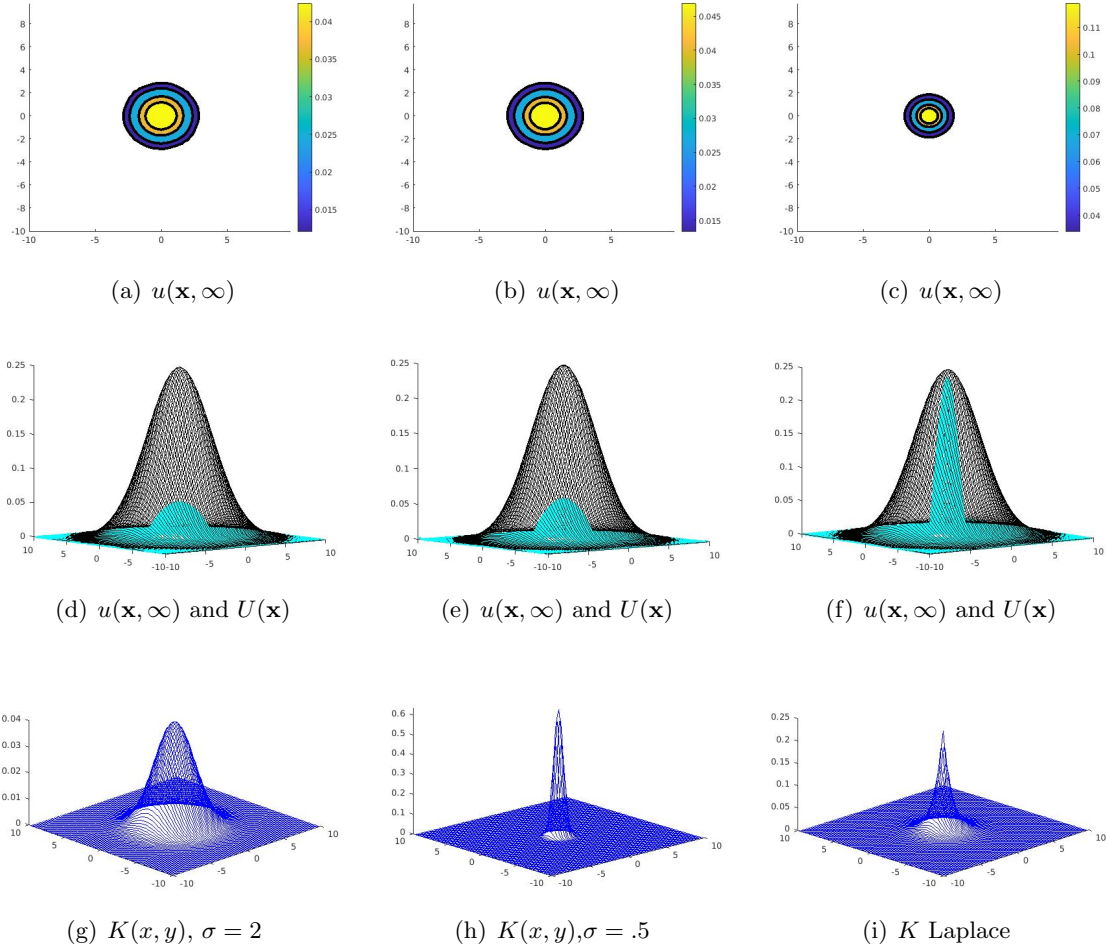

(d) $u(\mathbf{x}, \infty)$, $U(\mathbf{x})$, $a = .25$
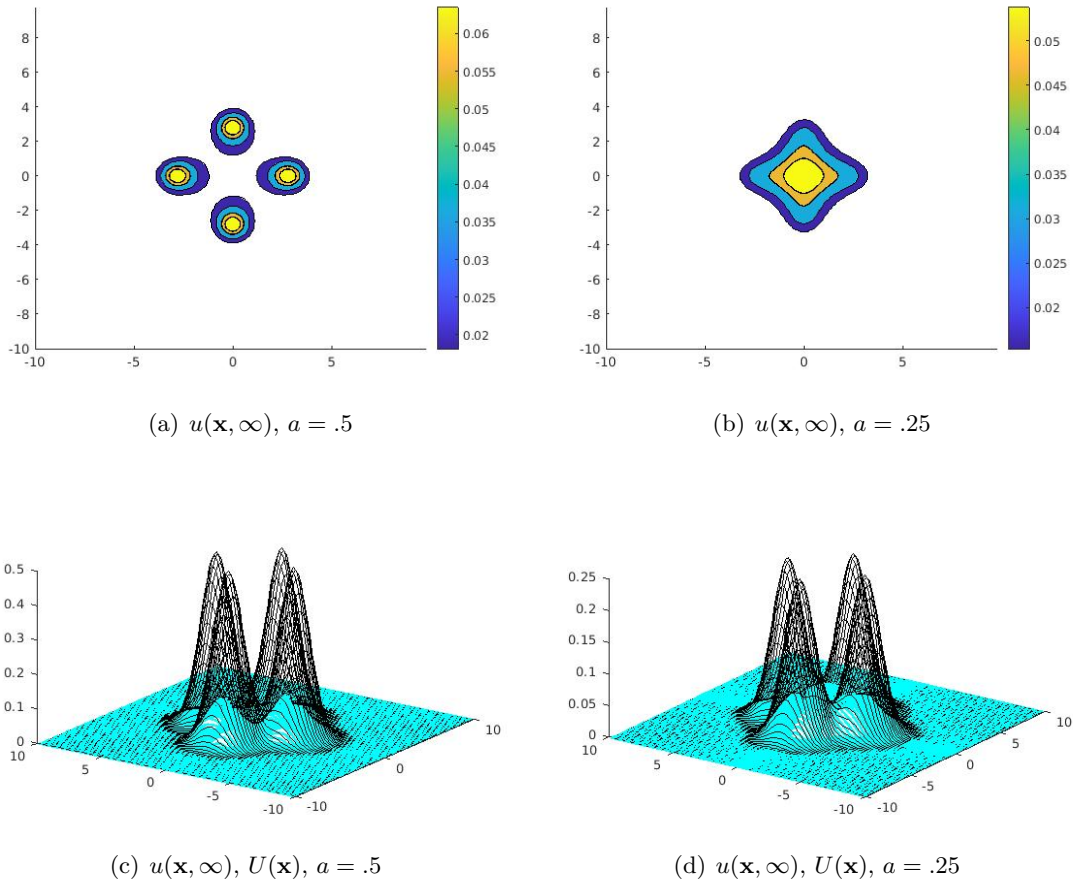
Figure 2.18: Equilibrium solutions to (2.7) with varied a, $\eta = 3$ and $b = .5$, shown as a contour plot (top) and a three-dimensional plot with $U(\mathbf{x})$ in black (bottom)

for $U(x, y)$. Each column is a simulation with a different a value, and each row shows the same perspectives as in 2.16.

First, we consider how changing a changes the equilibrium solution. In both cases, the attractiveness of the environment pulls in more of the population as a increases, and the territory becomes smaller and more concentrated around the attractive environment. We also note that the shape of the environment affects the change in territory as a increases, as well. The territory in Figure 2.17 changes more drastically than Figure 2.16 due to the fact that there is a sharp decrease in U. In Figure 2.17, the population density also changes more drastically. The maximum value of u changes from approximately .13 in Figure 2.17(d) when $a = .25$ to a maximum value of .24 in

Figure 2.17(f) when $a = 1$. In Figure 2.16, there is a slower decrease in U, meaning a larger area of attractive environment, and less drastic change as we change a. In this simulation, the maximum value of u changes from approximately .1 in Figure 2.16(d) to .13 in 2.16(f) as a changes from .25 to 1. The shape of the environment also plays a role in the shape of the equilibrium solutions, as can be seen in Figure 2.16(a), 2.16(b), and 2.16(c), the solution decreases more gradually, while in Figure 2.17(a), 2.17(b), and 2.17(c), the solutions decreases more sharply, both mimicking the shape of the environment.

The previous simulation demonstrated how the environment potential can compete with the strength of diffusion. However, it is also the case that an environment can compete with the aggregation strength. This is demonstrated in Figure 2.18, which shows two simulations with η and b constant and varying values of a. There are four distinct peaks of attractive environment. In Figure 2.18(b), the territory of u is connected, although attracted to the environment in four different directions. In Figure 2.18(a), a is stronger, and thus overpowers the aggregation strength within u, and the territory splits into the four distinct regions. Note that the territories are still pulled towards the center of the domain, as the four separate regions are attracted to each other.

2.6.2.2   Solutions - $N > 1$

As discussed, investigating equilibrium solutions for multiple groups is of particular importance, as the data we plan to consider include thirteen groups of meerkats. We begin by investigating the effect of the interaction potential K with multiple groups, because the potential K acts as an aggregation potential within groups and a segregation potential between groups. We also consider the importance of each of the terms in the behavior of the solutions to System (3.10), and how the computation time scales as we increase the number of groups in our simulations. Finally, we consider the meerkat location data and the environment data in solutions to the the model

Figure 2.19 demonstrates what occurs as the interaction potential strength changes for multiple groups. In this figure, b is varied and the environment and η are kept constant. The environment potential is the same as Figure 2.16(d). The columns are simulations for each value of b, and the

(a) $u_i(\mathbf{x}, \infty)$, $b = .5$ (b) $u_i(\mathbf{x}, \infty)$, $b = .75$ (c) $u_i(\mathbf{x}, \infty)$, $b = 1$

(d) $u_i(\mathbf{x}, \infty)$, $U(\mathbf{x})$, $b = .5$ (e) $u_i(\mathbf{x}, \infty)$, $U(\mathbf{x})$, $b = .75$ (f) $u_i(\mathbf{x}, \infty)$, $U(\mathbf{x})$, $b = 1$
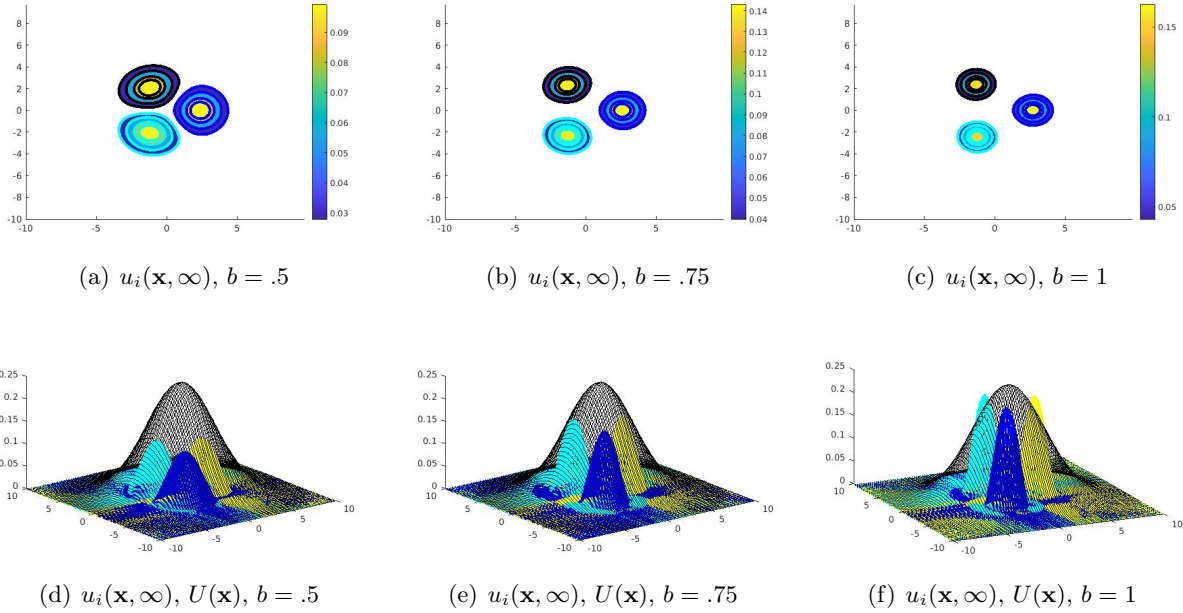
Figure 2.19: Equilibrium solution to (2.7) for $i = 1, 2, 3$ with $\eta = 3$ and $a = 1$ shown with a contour plot (top) and a three dimensional plot with U in black (bottom).

rows are the same two plots as previous cases. In Figure 2.19(c), the groups take up less territory and have higher population density which occurs when $n = 1$, but there is also more space separating the territories between groups than we see in Figure 2.19(a). Thus, as b increases, there is more aggregation within groups and more segregation between groups.

Next, we demonstrate the importance of each term in System (2.7). Figure 2.20 considers the dynamics of the solution when $\eta = 0$; no diffusion within each group. This illustrates the importance of the diffusion term, $\eta \Delta u^2$. In this case, the aggregation within a group resulting from the potential K has nothing to balance it out, and each group begins to aggregate to a single point, seen in Figure 2.20(c) and Figure 2.20(f). However, there are cases where the diffusion term is not needed if the aggregation potential is chosen correctly. Figure 2.21 shows a simulation done with $\eta = 0$, but the aggregation potential is the Morse potential, shown in Figure 2.21(c), which repulses a group at shorter range and aggregates a group at longer range. The segregation potential is the Laplace potential. In this simulation, we have two different functions for K; one potential controls the aggregation within a group (Figure 2.21(c)), and the other controls the repulsion between

(a) $u_i(\mathbf{x},0)$ (b) $u_i(\mathbf{x},t_1)$, $t_1 > 0$ (c) $u_i(\mathbf{x},t_2)$, $t_2 > t_1$

(d) $u_i(\mathbf{x},0)$ and $U(x)$ (e) $u_i(\mathbf{x},t_1)$, $t_1 > 0$ and $U(x)$ (f) $u_i(\mathbf{x},t_2)$, $t_2 > t_1$ and $U(x)$
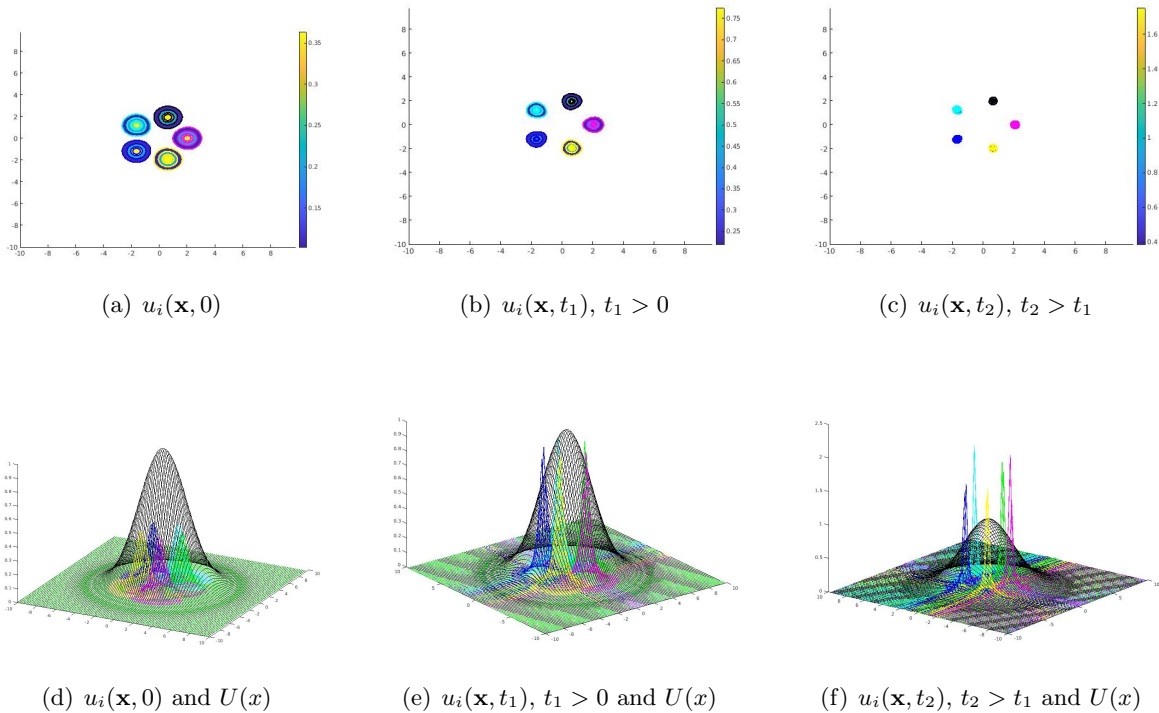
Figure 2.20: Dynamics of solution to (2.7) for $i = 1, ..., 5$ with $\eta = 0$, $b = 1$, and $a = .25$, shown with a contour plot (top) and three-dimensional plot with $U(\mathbf{x})$ in black (bottom).

(a) Equilibrium solution   (b) Equilibrium solution and U (c) Aggregation Potential
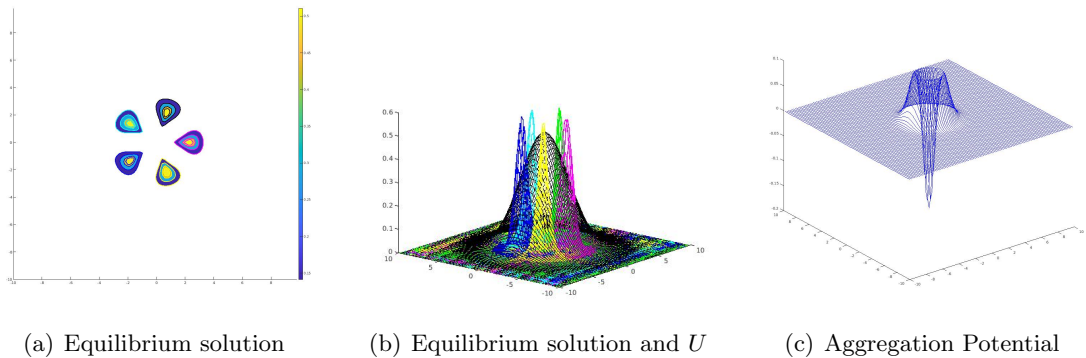
Figure 2.21: Equilibrium solution to (2.7) for $i = 1, ..., 5$ with $\eta = 0$, $a = .5$, $b = .5$ shown with a contour plot (left) and three-dimensional plot with U in black (middle), and K as the Morse potential (right).

groups (Figure 2.15(i)). The repulsion at shorter range in the Morse potential allows for $\eta = 0$, preventing groups from aggregating to a single point and maintaining coherence within a group, shown by the equilibrium solution in Figure 2.21(a).

(a) $u_i(\mathbf{x}, 0)$ (b) $u_i(\mathbf{x}, t_1)$, $t_1 > 0$ (c) $u_i(\mathbf{x}, t_2)$, $t_2 > t_1$
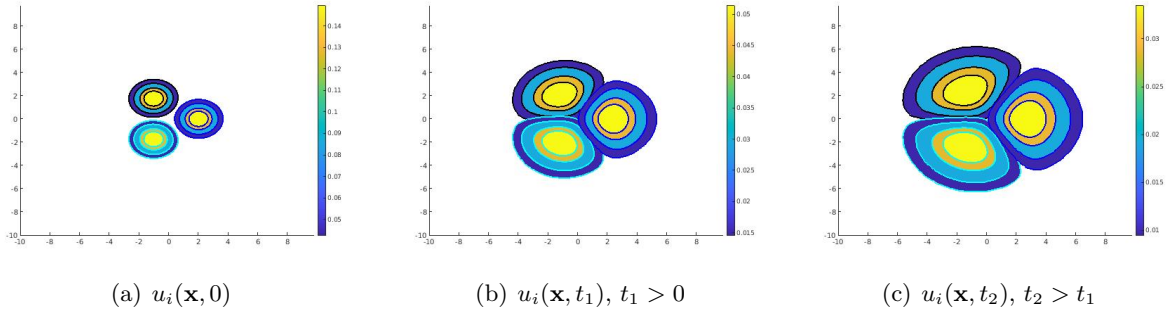
Figure 2.22: Dynamics of the solution to (2.7) with $\eta = 5$, $b = 1$, $a = .25$, $U(\mathbf{x}, t) = 0$, and no aggregation potential.

(a) $u_i(\mathbf{x}, 0)$ (b) $u_i(\mathbf{x}, t_1)$, $t_1 > 0$ (c) $u_i(\mathbf{x}, t_2)$, $t_2 > t_1$
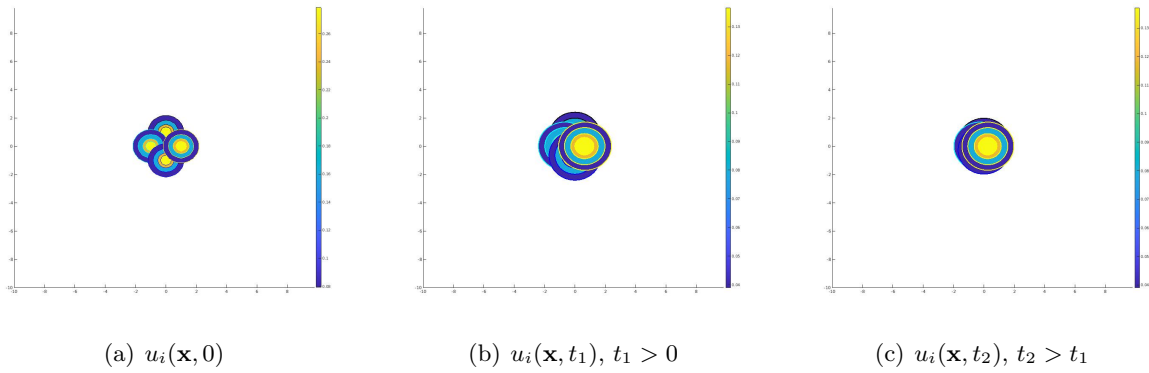
Figure 2.23: Dynamics of the solution to (2.7) with $\eta = 5$, $b = 1$, $a = .25$, and no segregation potential, and $U(\mathbf{x})$ from Figure 2.20.

Figure 2.22 demonstrates the importance of the nonlocal aggregation within a group. Without this term, the groups do not maintain coherence. The initial condition is shown in Figure 2.22(a), and u at a later time is shown in Figure 2.22(c). The difference between the maximum value and the minimum value of the population density are getting closer together, thus closer to a constant in the area not occupied by opposing groups. With only one group, we would see the solution go towards a constant, and with $U(x, y) > 0$, the group would be attracted to larger values of U without regard to whether it split into disjoint territories. Finally, Figure 2.23 demonstrates the importance of the nonlocal segregation term. In this simulation, the segregation potential is zero. The groups are attracted to the environment and overlap their territories over desirable habitat. Thus, to achieve segregated territories, the nonlocal segregation term is necessary.

		a = .25					a = 1				
	$N\ /\eta$	1	3	5	7	9	1	3	5	7	9
	1	6	25	14	16	20	46	8	15	17	21
$b = .5$	3	82	31	58	56	69	194	25	62	49	66
	5	362	107	120	108	133	354	52	75	115	115
	7	1038	270	216	169	206	1926	164	119	162	138
	$N\ /\eta$	1	3	5	7	9	1	3	5	7	9
	1	65	6	20	14	25		6	14	10	17
$b = 1$	3		126	94	63	73		50	32	49	91
	5		446	248	202	191		265	226	156	147
	7		1202	481	375	288		734	392	351	290

Table 2.6: Computation time in seconds for varying environment strength (a), potential strength (b), group number (n), and diffusivity parameter (η) with $tol = .025$.

We also consider the expense of adding multiple groups to our simulations. For different values of η, a and b, we determine how long it takes to compute an equilibrium solution for $N = 1, 3, 5, 7$ groups. Table 2.6 shows these computation times. These simulations were done with the same starting point for each trial, $u^{i,0} = e^{-(x-x_0^i)^2-(y-y_0^i)^2}$, the same environment potential, $U(x,y) = \exp(-.1x^2 - .1y^2)$, and K as the Laplace potential. For $n = 1$, $(x_0, y_0) = (0,0)$. For $n > 1$, (x_0^i, y_0^i) were spaced symmetrically about a circle centered at the origin with radius 2. The simulations were run until the error for each equation in the System (2.7), described in Section 2.6.1, was under a chosen tolerance, $tol = .01$.

It is clear that the computational expense increases as we increase the number of groups. However, it is worth noting that the computational expense is dramatically less than in [36], where the time to compute an equilibrium solution in two dimensions with $N = 1$ was on the order of hours. It is also the case that some regimes of η and b are more efficient than others for higher values of N. As mentioned in the case where $N = 1$, there is interplay between η and b. When b is larger and there is a stronger sense of aggregation within groups, a higher η balances this out. It can clearly be seen in Table 2.6 that lower η values take longer to compute when $b = 1$ than when $b = .5$. In these regimes, it seems the expense of adding groups is constant relative to group number, while in the regimes where η is small relative to b, it is more expensive to add groups. It is also possible that this could be the effect of initial data. In some parameter regimes, the initial data

is further away from an equilibrium solution. It is also important to note that we have observed different simulations with different environments are faster or slower than others. We remark on this in more detail later in the section.
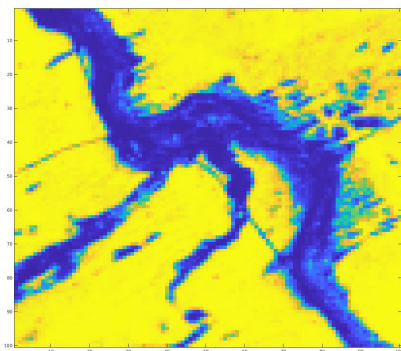
(a) Sand Environmental Data
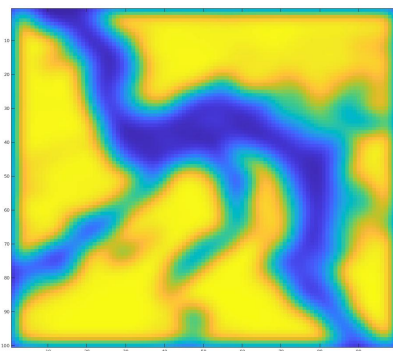
(b) Mollified Sand Environmental Data
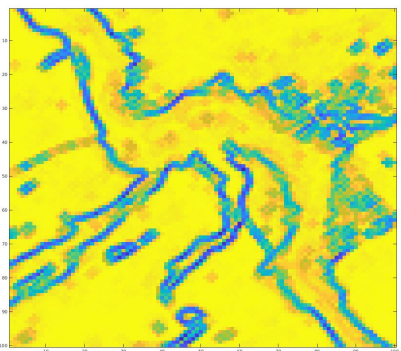
(c) Edge Environmental Data
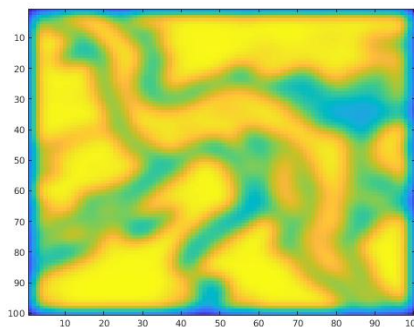
(d) Mollified Edge Environmental Data

Figure 2.24: Environmental data (left) and mollified environmental data (right) in the same geographical area in South Africa for two environment types on a scale of 0 (unattractive environment) to 1 (attractive environment), where yellow is attractive and blue is unattractive.

Finally, we consider the environment data and meerkat location data while solving for meerkat equilibrium solutions. The detailed account of the acquisition of the habitat data can be found in [7]. The environmental data are shown in Figure 2.24(a) and Figure 2.24(c). The data were rescaled fall between zero and one. For the sand-type data, Figure 2.24(a), zero corresponds to clay sand, and one corresponds to ferrous sand. For the edge data, or the interface between sand-types seen

in Figure 2.24(c), zero corresponds to the interface and one corresponds to one distinct sand-type. Due to the nature of the data, we convolve the environmental data with a mollifier so that we can consider a smoother $U(x, y)$ in our simulations. These mollified environment functions are shown in Figure 2.24(b) and Figure 2.24(d). Finally, we consider the meerkat location data. In [7], three time periods of data were considered: a steady period where territories didn't move, a period where a group split into two new meerkat groups, and a period where territories shifted. Due to the fact that we are considering equilibrium solutions, we show the data from the steady period in Figure 2.25(a). To feed our algorithm initial conditions with this data, we compute the kernel density estimation with the given data for each group, shown in Figure 2.25(b). Figure 2.25(c) and Figure 2.25(d) show how the two different environments considered can lead to different territories. These figures were both generated with the same parameter values, but Figure 2.25(c) was generated with the environment seen in Figure 2.24(d), and Figure 2.25(d) was generated with the environment seen in Figure 2.24(b). For this parameter set, it is clear that the edge environment more accurately predicts the meerkat locations than the sand environment. These equilibrium solutions found with starting points from location data were found more quickly than those with a similar number of groups found with the typical Gaussian environment. It is likely the more detailed environment and the initial conditions that begin in popular locations helped to decrease the computation time.

2.7   Incorporation of Data

For proof of concept and to test our method of incorporating data, we work with synthetic data. We generate the synthetic data by first finding an equilibrium solution, $f(x, y)$, with known parameters. We then pick (x, y) randomly in the domain and p randomly in $(0, 1)$. If $f(x, y) > p$, we keep the sample. If $f(x, y) < p$, we reject it. Therefore, if (x, y) is at a location with higher population density, we are more likely to keep that sample. Figure 2.26(a) shows an example of a PDF generated with known parameters and Figure 2.26(b) shows the synthetic data generated from the PDF.
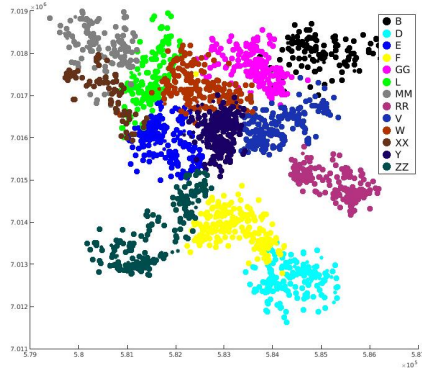
(a) Meerkat location data
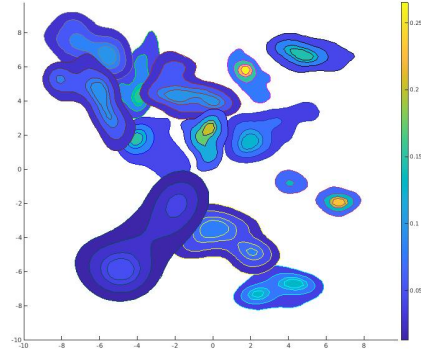
(b) Kernel density estimation of (a)
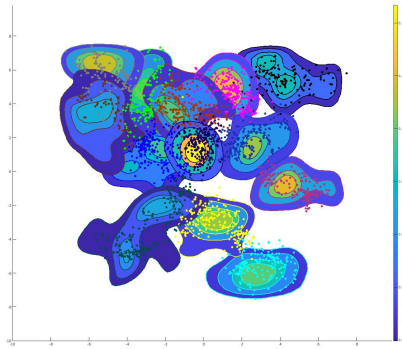
(c) Equilibrium solution to (2.7) with $u_0(x)$ from (b), $U = $ Edge, and data from (a)
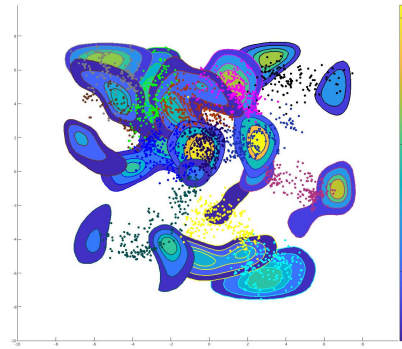
(d) Equilibrium solution to (2.7) with $u_0(x)$ from (b), $U = $ Sand, and data from (a)

Figure 2.25: Meerkat location data in (a), kernel density estimation of location data in (b), and equilibrium solutions to (2.7) with $b = .25$, $a = 1$, $\eta = 3$, $u_0(x)$ from Figure 2.25(b), and two different mollified environment types from Figure 2.24, $U = $ Edge (c) and Sand (d).

We perform maximum likelihood estimation on the set of synthetic data, $\{y_i | i = 1, ...N\}$. We minimize the negative of the log-likelihood function over the set of parameters, θ,

$$-\ell(\theta) = -\log\left(\prod f\left(y_i|\theta\right)\right).$$

To do this, we find the PDFs, $f(x|\theta)$ using the methods described in Section 2.6.1 with starting point determined by kernel density estimation of the set of synthetic data. In order to better understand the behavior of the function we are minimizing, we found an equilibrium solution for a pre-determined value of b and generated synthetic data from that PDF. Using this data, y_i for $i = $

(a) PDF with known parameters   (b) Synthetic data generated from PDF
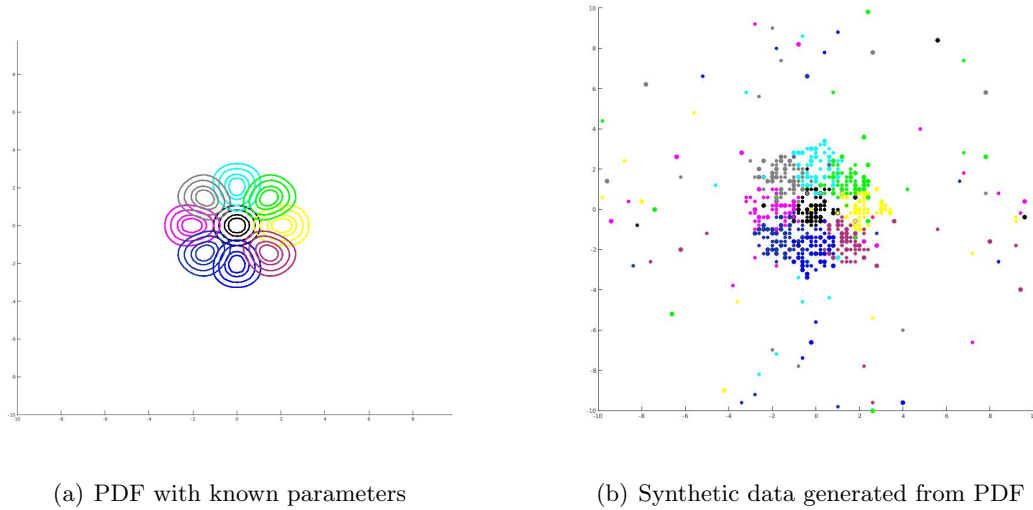
Figure 2.26: Contour plot of a PDF from numerical solution of system (3.10) (left) and corresponding synthetic data (right).

(a) $b = 1$ (b) $b = 2$
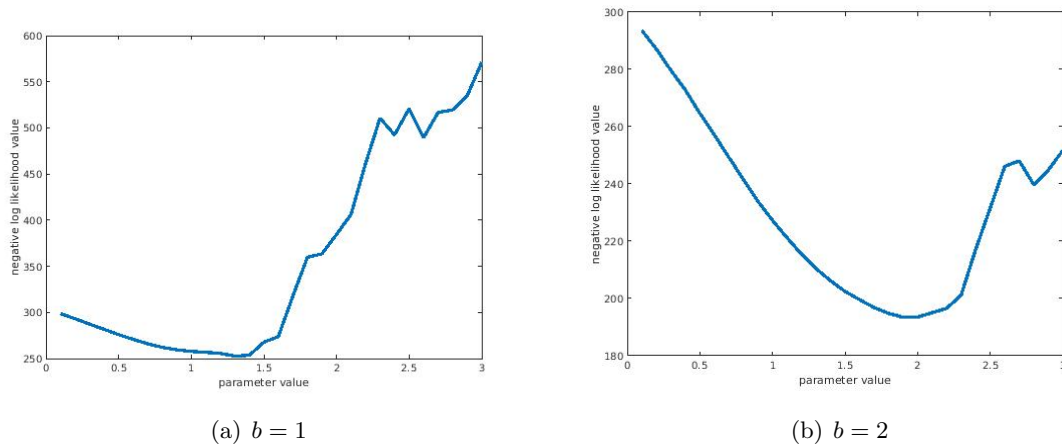
Figure 2.27: Negative log-likelihood functions with data generated from varying b, $n = 1$, $\eta = 5$ and $a = .25$.

1...50, we calculated the one-dimensional negative log-likelihood function by generating equilibrium solutions for values of b, $f(x|b)$, and computing $-\log\left(\prod f\left(y_i|b\right)\right)$. Therefore, the minimum of this function is the parameter value most likely used to generate the data. The negative log-likelihood functions for two different data sets generated from different parameter values, b, are shown in Figure 2.27. In Figure 2.27(a), the data was generated with $b = 1$. Due to the random nature

of the generated data, the minimum of the log-likelihood function is actually around $b = 1.4$. The data used in the log-likelihood function in Figure 2.27(b) was generated with $b = 2$, which is approximately where the minimum occurs. In both cases, the minimum is near the parameter used to generate the data. It is important to note that there are local minimums which we want to avoid while minimizing these functions. We also observe in some cases for lower values of b, the slope of the log-likelihood function below b gets shallower. Thus, we want to consider methods to minimize the negative log-likelihood function that will allow us to avoid getting stuck in local minimums and also to move quickly down shallow slopes.

Therefore, we use stochastic gradient descent (SGD) to minimize the negative log likelihood function. SGD uses a small subset of data to update the parameter at each iteration. This leads to more variance in the update, thus allowing a possibility to move away from a local minimizer. We update the parameter as follows:

$$\theta = \theta - \alpha \nabla_\theta \left(-\log(f(y_i|\theta)) \right), \tag{2.29}$$

where y_i is a randomly chosen data point (or small set of data points) from the set of synthetic data, and α is the learning parameter which typically decreases as we iterate. We also consider a variation of stochastic gradient descent, the momentum method, that averages over past gradients. This method can be useful to speed up convergence for functions with shallow gradients in some directions, thus an attractive method for the cases with shallow gradient that we have observed. The parameter is updated as follows,

$$\begin{cases} v = \gamma v + \alpha \nabla_\theta \left(-\log(f(y_i|\theta)) \right) \\ \theta = \theta - v. \end{cases} \tag{2.30}$$

Both α and γ can change in time.

Figure 2.28 and Figure 2.29 demonstrate two examples of fitting a single parameter to data for one group. We fit b and η, respectively. Figure 2.28(a) and Figure 2.29(a) are the log-likelihood functions that we are attempting to minimize. Note that the shallower slopes in the log likelihood functions occur in the parameter regimes that lead to larger territories. Intuitively, this makes sense

(a) Negative log-likelihood function

(b) Approximated b (top) and corresponding log-likelihood value (bottom) for each iteration of SGD
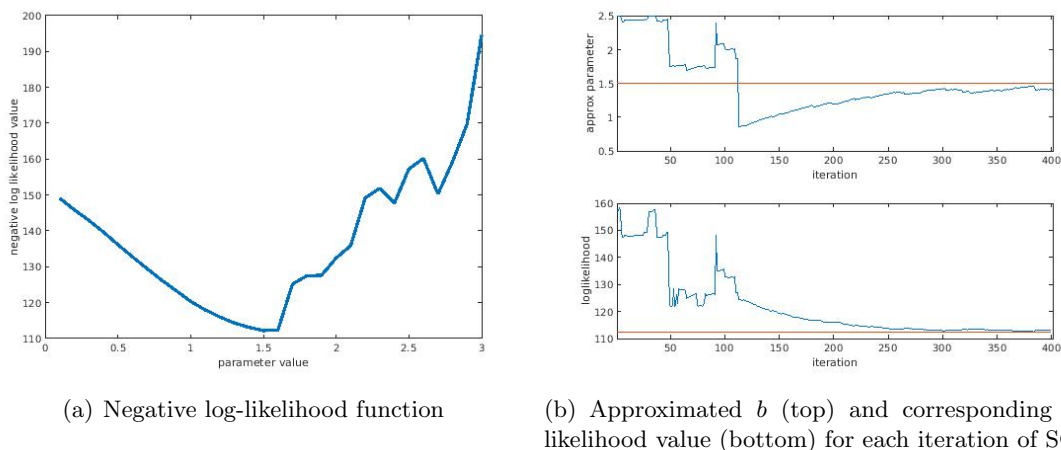
Figure 2.28: The negative log likelihood function (left) and stochastic gradient descent iterations to estimate b (right), with 50 data points generated with $n = 1$, $b = 1.5$, $a = .25$, $\eta = 5$.

(a) Negative log-likelihood function

(b) Approximated η (top) and corresponding log-likelihood values (bottom) for each iteration of SGD
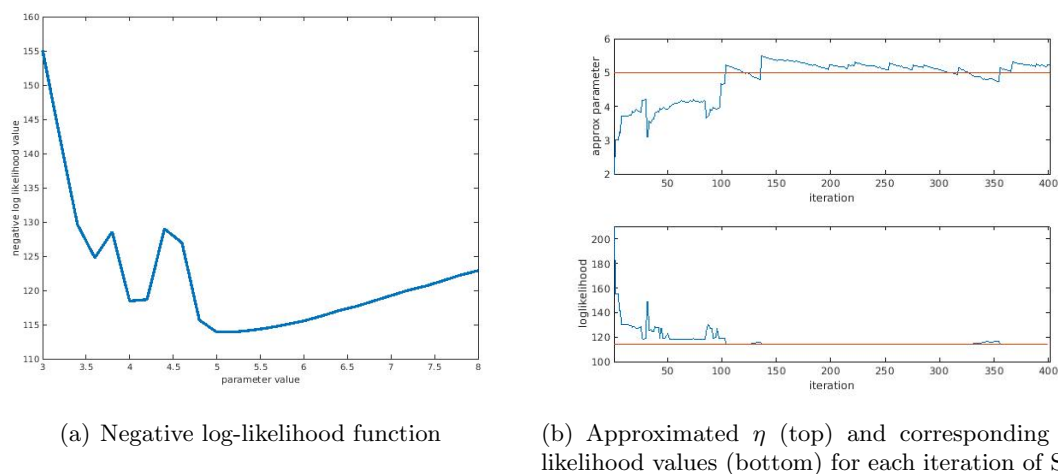
Figure 2.29: The negative log likelihood function (left) and stochastic gradient descent iterations to estimate η (right), with 50 data points generated from $\eta = 5$, $b = 1.5$, $a = .25$.

as there is a greater expense for data points lying outside of a territory due to the steepness of the log function near zero. This may serve as information to keep in mind when choosing starting estimates for parameters when the log-likelihood function is unknown. In Figure 2.28, $\eta = 5$, $a = .25$, and the number of data points generated was 50. The step size for iteration m was $\alpha(m) = .01(.9)^m$. In Figure 2.28(a), there are local minimums in the log likelihood function we are able to successfully avoid and converge to the correct parameter value. In Figure 2.29, $b = 1.5$,

$a = .25$, and the number of data points generated was 50. The step size for iteration m was $.1(.9)^m$. When we fit η, we found a larger step size to be appropriate. Again, we see local minimums in Figure 2.29(a), and we are able to successfully avoid these and converge to the correct parameter value.
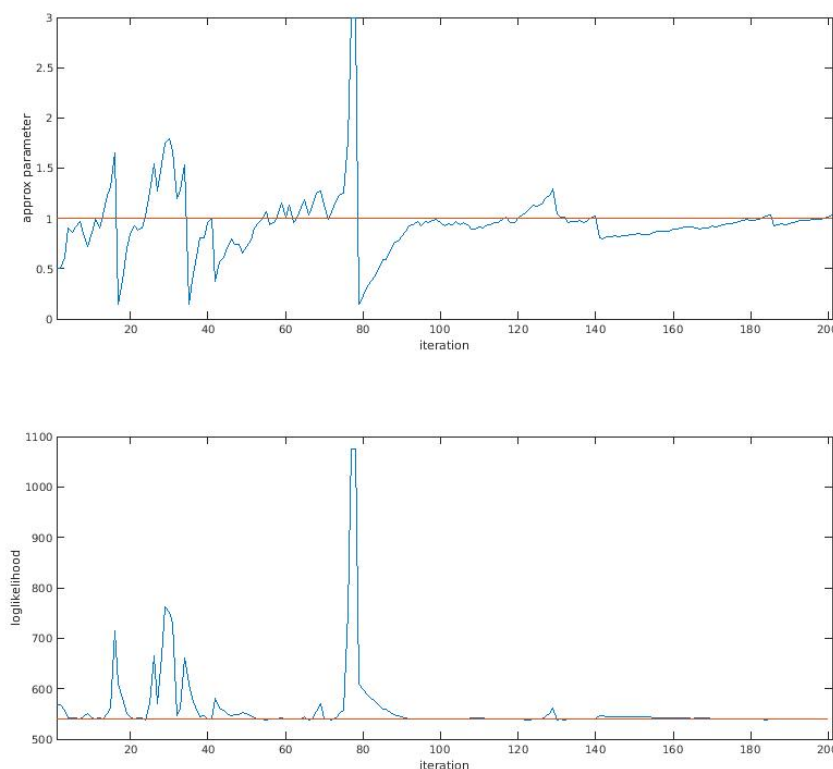
Figure 2.30: The estimated parameter value for b (top) and log likelihood value (bottom) for each iteration of stochastic gradient descent (blue), and the values from true parameters (red) using 100 data points generated with $n = 2$, $b = 1$, $a = .25$, and $\eta = 5$.

It is a natural next step to consider fitting data to multiple groups and to fit multiple parameters. As we increase n and the number of parameters we are estimating, we cannot efficiently generate the log-likelihood function to find the minimum, and we must depend on stochastic gradient descent. We begin by fitting data with one parameter and $n = 2$. In Figure 2.30, we estimate the parameter b from data generated with $b = 1$ and $n = 2$. The figure shows the algorithm con-
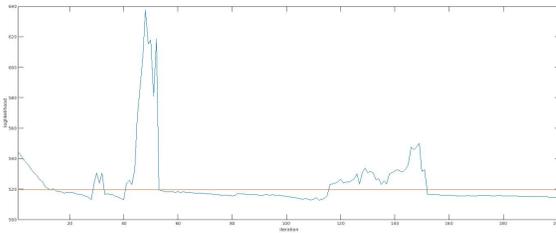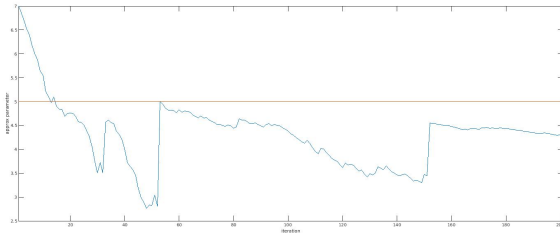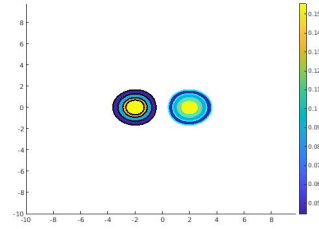
(b) Equilibrium solution to (2.7) with $b = 1$ and $\eta = 4.3$

(c) Equilibrium solution to (2.7) with $b = 1$ and $\eta = 5$

(a) Estimated parameter value for η (top) and log-likelihood value (bottom) for each iteration of SGD (blue), and values from true parameters (red).
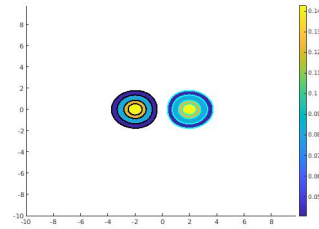
Figure 2.31: One trial of stochastic gradient descent done with 100 data points generated with $n = 2$, $b = 1$, $a = .25$, and $\eta = 5$ (left), and equilibrium solutions to (2.7) with the parameters used to generate the data (bottom right) and from the predicted parameters (top right).

verging to $b = 1$ and to the minimum of the log-likelihood value, both shown in red. In Figure 2.31, we estimate η from data generated with $\eta = 5$ and $n = 2$. Here, the algorithm does not converge to the parameter the data was generated with, but converges to a parameter value that has a lower log-likelihood value than the parameter used to generate the data. It is worth looking at the predicted territories from both of these parameters. Figure 2.31(b) and 2.31(c) show equilibrium solutions from the parameters predicted in Figure 2.31(a) and the parameters used to generate the data, respectively. Here, the territory boundaries and the population densities are similar, and the algorithm predicts a similar territory to the one the data came from.

In Figure 2.32, we estimate both the parameter b and η for $n = 1$ using data generated with $b = 1.5$ and $\eta = 5$. The figure shows the approximated parameters for each iteration and the corresponding log-likelihood functions. The red lines show the parameter value used to generated the
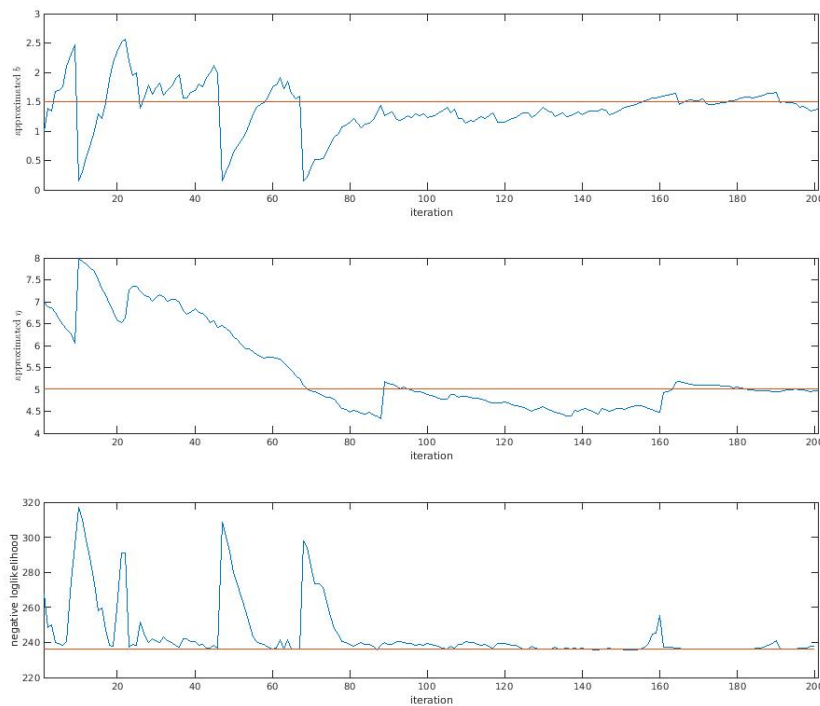
Figure 2.32: Estimated b (top), η (middle), and corresponding log-likelihood values (bottom) for each iteration of stochastic gradient descent (blue) using 100 data points generated with $n = 1$, $b = 1.5$, $a = .25$, and $\eta = 5$, where the true parameters and log-likelihood value are shown in red.

data and its corresponding log-likelihood value. In this simulation, we converge to approximately the correct parameter for both η and b.

There are cases where stochastic gradient descent does not converge to the parameters that were used to generate the data. We consider this in Figure 2.33. Figure 2.33(a) and Figure 2.33(b) show two trials of stochastic gradient descent, both using data generated with $b = 1$ and $\eta = 5$. In Figure 2.33(a), the algorithm converges approximately to $\eta = 6.6$ and $b = 1.6$. In Figure 2.33(b), the algorithm converges approximately to $\eta = 6.7$ and $b = 1.25$. In both of these cases, the value of the log-likelihood function that the estimated parameters produces is similar to that of the true parameters. We consider whether these estimated parameters predict similar territories. This is reasonable, as η is overestimated, leading to a larger territory, but b is also overestimated,
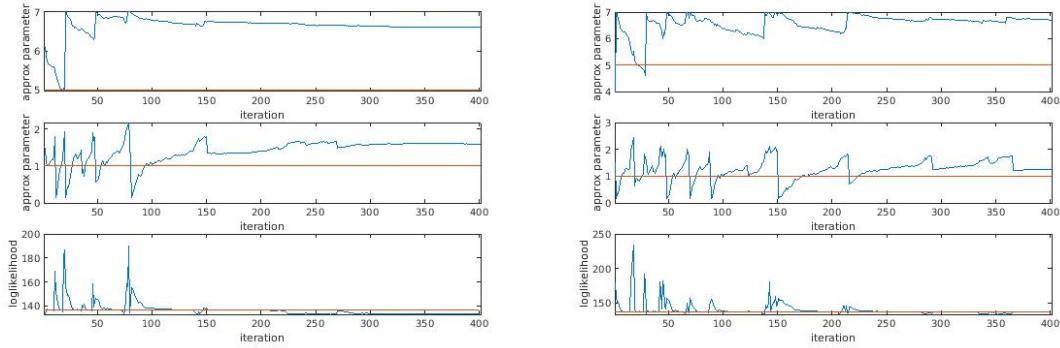
(a) Estimated η, b, and corresponding log-likelihood values for each iteration of SGD (blue), and values from true parameters (red).

(b) Estimated η, b, and corresponding log-likelihood values for each iteration of SGD (blue), and values from true parameters (red)
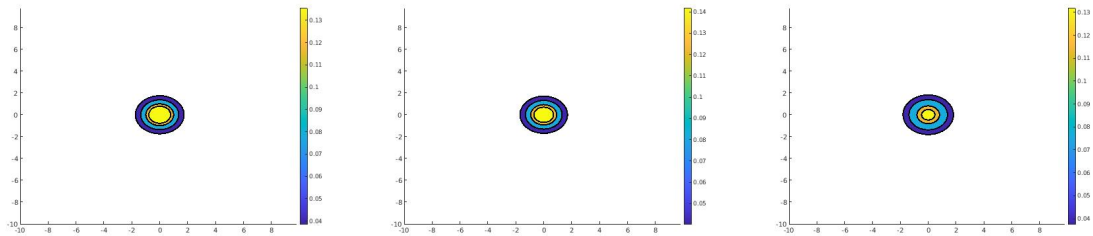
(c) Equilibrium solution to (2.7) with $b = 1$, $\eta = 5$

(d) Equilibrium solution to (2.7) with $b = 1.6$, $\eta = 6.6$

(e) Equilibrium solution to (2.7) with $b = 1.25$, $\eta = 6.7$

Figure 2.33: Two trials of Stochastic Gradient Descent (top) to determine η and b from two sets of 100 data data points generated with $\eta = 5$ and $b = 1$, and equilibrium solutions (bottom) from the true parameters (left) and the predicted parameters (middle and right).

leading to a more aggregated territory. These could balance out to result in similar territories. In Figures 2.33(c), 2.33(d), and 2.33(e), we consider the equilibrium solutions of System 3.10 with the parameters used to generate data, and the two estimated parameter sets. These three sets of parameters predict similar territory boundaries, and they all have a maximum value between .13 and .14. While the algorithm converges to different parameters than those used to generate the data, the estimated parameters still predict a similar territory. It is worth noting that the step size, α, used for η seems to be too small to visit the parameter space in the same way that was done for b. Perhaps with a larger step size or a different starting value for η, the correct parameter would resurface. In all of these cases, converging to the correct parameter is sensitive to the chosen step size. A step size too large might take many iterations to converge, and thus take too long, but a

step size too small or decreasing too quickly could decrease before the algorithm has had a chance to settle on the correct parameter value.

2.8 Conclusions and Future Work

We investigate a nonlocal mechanistic model which we argue to be more suitable for social groups without a home center. First, we study the gradient-flow structure of our model and its local approximations by minimizing associated energies to find equilibrium solutions. We find the energy landscapes to be complex, and in some cases, the equilibrium solutions of the local approximation did not match those of the nonlocal model. We also find that for starting data close to a minimizer, the local approximation was not necessarily more efficient. Second, we use spectral methods to solve System (2.7), and find this method to be a more efficient way to compute solutions. Using spectral methods, we are able to investigate the effects of each term, the aggregation and segregation potential, and the environment on solutions. We are also able to compute equilibrium solutions efficiently enough to incorporate synthetic data into the model for two groups and two parameters. When incorporating synthetic data, a more rigorous study of appropriate step sizes in stochastic gradient descent and initial guesses for the parameters remains to be investigated. Naturally, we also aim to use spectral methods to incorporate the meerkat location data and environmental data to our model.

Chapter 3

Birth Jump Processes

3.1   Introduction

Since Skellam's seminal paper linking random walks of species and the heat equation [102], the study of reaction-diffusion equations has gone hand in hand with the study of spatial ecology. In fact, numerous researchers have used the classical reaction-diffusion equation,

$$u_t(x,t) = d\Delta u + f(u,x), \ \ \text{for } (x,t) \in \mathbb{R} \times \mathbb{R}^+, \tag{3.1}$$

as a general model to understand the spatio-temporal dynamics of ecological populations; see [16, 56, 83, 88] and references within. This equation naturally considers these subprocesses as separate and is suitable for certain populations (e.g. many mammals). Another equation typically used to study the spatiotemporal dynamics of ecological populations, where dispersal may be born out of a *position-jump process*, is a generalization of the classical reaction-diffusion equation that incorporates a non-local diffusion operator:

$$u_t = \int_{\mathbb{R}} J(x-y)u(y,t) \, dy - u + f(x,u) \ \ \text{for } (x,t) \in \mathbb{R} \times \mathbb{R}^+. \tag{3.2}$$

For example, in ecology (3.2) is a more suitable model for species, such as seeds, that are moved from one location to another due to wind effects [53, 87, 52]. Equation (3.2) has received much attention and has been the subject of numerous studies – see for example [20, 1] and reference within. One can argue that it broadens the types of species whose dynamics can be described through these types of mechanistic models. However, it still separates the subprocesses of dispersal

and reproduction. A *birth-jump process* is one where these subprocesses are inextricably linked. As mentioned earlier, a strong case has been made that these processes are more suitable for phenomena such as fire propagation and cancer cell dynamics. It has also been argued to be more accurate to seed dispersal.

3.1.1   Application: Seed Dispersal

Dispersal is crucial to the ability of plants to be able to move in and adapt to their environment, hence crucial to their survival. Various models have been used to describe seed dispersal including integrodifference equations, random walks, reaction-diffusion equations, and agent based models, and the interest in modeling seed dispersal extends to a variety of situations including changing environments [41] and two-species predator-prey interactions [58]. Classical results have used random walks to describe seed dispersal [39, 54]. However, processes that move seeds such as wind and animals are better described by long distance dispersal. This has been done in the context of integro-difference equations [55], stochastic models [25], and a a generalization of reaction-diffusion equations called a position-jump process, equation (3.2) [53, 87, 52].

Consider what happens when a seed is produced. It is immediately dispersed via wind, gravity, and animals. Thus, modeling seed dispersal where birth and dispersal are linked is of interest. This has been done in the context of Agent Based Models (ABM), which provide a description of how individuals move in a spatially heterogeneous environment, and are useful in describing ecological processes that include birth and death, movement, and the environment [42, 66]. They have also been useful to describe how individuals move in response to environmental changes due to climate change [31, 92]. An ABM was used in [65] to understand plant dynamics. However, as noted in [93], the ABM does not provide much opportunity for analysis. Thus, from this model, they derive a birth-jump process as a model for plant dynamics, which we provide details on below. The birth-jump process can be seen as a generalization of a classical reaction-diffusion equation which provides the benefit of determining when a species survives or goes extinct, but is also distinct from models such as a position-jump process due to the fact that birth cannot be

decoupled from dispersal.

3.1.2   Model and Methods

We consider the following integro-differential equation modeling a *birth-jump process*, which was introduced in [48],

$$\begin{cases} u_t(x,t) = g(u(x,t),x) \int_{\mathbb{R}^2} S(x,y)\beta(u(y,t),y)u(y,t) \, dy - \delta u(x,t), \ x \in \mathbb{R}^d, \ t > 0, \\ u(x,0) = u_0(x). \end{cases} \tag{3.3}$$

To understand the connection between the classical reaction-diffusion equation and the integro-differential equation modeling a birth-jump process, one can take a diffusion limit of the latter (under suitable conditions of the relocation potential) to obtain a reaction-diffusion equation where the birth term appears not only in the reaction term, but also in the diffusion term. Thus, one might expect that the dynamics of a population following the birth-jump model can be very different. Above, the function $\beta(y,u)$ models the birth rate at location y, which can density dependent; the function $g(x,u)$ represents the rate of survival once the organism arrives at x, which can also be density dependent; and δ is the death rate. In the context of plant dynamics, g represents the germination rate. One can see that once birth takes place at the rate of β, relocation happens immediately. This relocation is controlled by $S : \mathbb{R} \times \mathbb{R} \to [0,\infty)$, the relocation potential; thus, $S(x,y)$ is the probability that an individual at location y will be relocated to location x. Note also the actual growth in the population at (x,t) is controlled by the function g.

The purpose of this study is to begin to understand the effect that a birth-jump process has on the persistence of a population that is subject to either logistic growth or a strong Allee effect. In a classical reaction-diffusion model the type of growth is modeled in the reaction term. However, in birth jump processes, one can model the Allee effect or logistic growth in either the survival rate or birth term. For example, in some plants an Allee effect has been detected in the germination process due to seed predation, but not in the production of seeds [110]. Motivated by this, we consider two types of germination functions: bistable-type or monostable-type, which we defined concretely in below. The dynamics in this case turn out to be very different than those for the case

when the Allee effect is incorporated in the birth term, and we will remark on this in more detail later on.

When modeling a strong Allee effect in the germination function we assume that g is of *bistable-type* with only three zeros at each spatial location and satisfies:

$$g(0,x) = g(\theta(x), x) = g(m(x), x) = 0, \ g'(0,x) < 0 \text{ for all } x \in \mathbb{R}^d. \tag{3.4}$$

for $0 < \theta(x) < m(x)$ for all $x \in \mathbb{R}^d$. The Allee threshold θ and the carrying capacity m can be spatially heterogeneous. To compare the dynamics of a population with and without the presence of the Allee effect we also study the case when g is of monostable-type: in this case g only has two zeros at each spatial location and satisfies:

$$g(0,x) = g(m(x), x) = 0, \ g'(0,x) > 0 \text{ for all } x \in \mathbb{R}^d, \tag{3.5}$$

where $0 < m(x)$ for all $x \in \mathbb{R}^d$. We assume that there is no loss of individuals during the redistribution process. Moreover, let us assume the following conditions:

(A1) The functions g and β be Lipschitz continuous and bounded with Lipschitz constants $\text{Lip}(g)$ and $\text{Lip}(\beta)$ respectively;

(A2) $\sup_{x \in \mathbb{R}^d} m(x) = M < \infty$;

(A3) S bounded and satisfies

$$\int S(x,y) \, dy \leq 1 \text{ for all } x \in \mathbb{R}^d \quad \text{and} \quad \int_{\mathbb{R}^d} \int_{\mathbb{R}^d} S(x,y) \, dy \, dx = 1 \text{ for all } x \in \mathbb{R}^d;$$

(A4) $\int S(x,y) \, dy > 0$ for all $x \in \mathbb{R}^d$.

Using analysis tools we first prove the existence of a global-in-time solution to equation (3.3) under physically relevant assumptions on g, β, and S. Next, we study the issue of persistence of a population depending on the initial data, with g either monostable or bistable. We also examine whether the relocation potential S can play a role in overcoming a strong Allee effect. By overcoming the Allee effect we mean that there are solutions with initial data below the Allee threshold that

will persist. In contrast to the classical reaction-diffusion equation (3.1), when the Allee effect or logistic growth is included in g we observe that the dynamics are governed at each spatial location by an ODE, leading to potentially discontinuous solutions. Interestingly, in this case S cannot help overcome the Allee effect. On the other hand, if there is an Allee effect incorporated in β, then the dynamics become more complex and there are relocation potentials that can help overcome the Allee effect. This is verified numerically. However, a limitation of this work is the lack of analytical results in this case. Another limitation of this study is that we do not consider an *ignition-type g* or β, which are physically very relevant.

We then consider a birth-jump process with the additional mechanism of linear diffusion,

$$\begin{cases} u_t(x,t) = d\Delta u(x,t) + g(u(x,t),x) \int_{\mathbb{R}^2} S(x,y)\beta(u(y,t),y)u(y,t)\,dy - \delta u(x,t), \\ u(x,0) = u_0(x), \end{cases} \tag{3.6}$$

for $x \in \mathbb{R}^d, t > 0$. We perform an analogous analysis to equation (3.3). In contrast, we find the analysis to be more difficult in some cases. This leads us to consider a simpler, and as mentioned, more physically relevant case where g is of ignition-type. In this case, g satisfies:

$$g(u) = 0 \text{ for } u \in (-\infty, \theta] \cup [m, \infty) \text{ and } g > 0 \text{ for } u \in (\theta, m). \tag{3.7}$$

We begin by proving global existence and uniqueness of a solution to equation (3.6) under similar assumptions to the case where $d = 0$. We also some prove properties of solutions, and in contrast to equation (3.3), solutions to equation (3.6) are continuous. Then, we study whether a population persists or goes extinct under certain initial data, with g monostable, ignition-type, and bistable. Unlike the case where $d = 0$, here we find cases in our numerical simulations where a population can overcome the Allee effect when it is incorporated in g. However, it is still true in this case that the redistribution term does not aid in overcoming the Allee effect when a population is below the Allee threshold.

3.2   From an Agent Based Model to a Birth-Jump Process

Birth-jump processes can be derived either from a position-jump process, seen in equation (3.2), which generalizes a random walk allowing individuals to make spatial jumps with a certain probability [52, 78, 84], or from a reaction-diffusion equation. As noted above, [93] introduced equation (3.3) as a model for plant dynamics, derived from an agent based model,

$$n_{ij}(t + \delta t) - n_{ij}(t) = \sum_{k=-\infty}^{\infty} \sum_{m=-\infty}^{\infty} p_\beta(\mathbf{x}_{km}) p_g(\mathbf{x}_{ij}) s_{\mathbf{x}_{km}\mathbf{x}_{ij}} n_{km}(t) - p_\delta(\mathbf{x}_{ij}) n_{ij}(t),$$

where $n_{ij}(t)$ is the number of plants at location x_{ij} and time t, $n_{ij}(t + \delta t)$ is the number of arriving seeds that germinate, and the number of surviving plants from time t. The number of arriving seeds that germinate is $\sum_{k=-\infty}^{\infty} \sum_{m=-\infty}^{\infty} p_\beta(\mathbf{x}_{km}) p_g(\mathbf{x}_{ij}) s_{\mathbf{x}_{km}\mathbf{x}_{ij}} n_{km}(t)$, and the surviving plants from time t is $(1 - p_\delta) n_{ij}(t)$, where p_β is the probability of birth, p_g is the probability of germination, s_{xy} is the probability that a seed at location y will be relocated to location x, and p_δ is the probability of death. To achieve the continuous model, they take the limit at δt and δx approach zero, moving from a discrete representation of plants to a density representation seen in (3.3).

3.3   Background

Much work has gone into developing a theory for equation (3.1) with both monostable and bistable growth-patterns. For simplicity, let us consider a constant Allee threshold, θ, and carrying capacity, m. We mention a few, now classical results, which are relevant for this work. For a monostable growth pattern case on $\mathbb{R}^d$, the solution to equation (3.1) with positive initial density will converge to m, uniformly in compact sets, as $t \to \infty$. The situation is more complicated for the bistable case. Indeed, let u represent the solution to (3.1) with positive initial data: if $u_0 > \theta$ in $\mathbb{R}^d$, then u will approach m, uniformly on compact sets; however, it will instead approach zero if $u_0 < \theta$ in $\mathbb{R}^d$ – see [4].

The behavior of solutions with more general initial data is more delicate, but of particular interest. For our purpose, more general means that u_0 is above the Allee threshold for some spatial

values, but less in others. In particular, the question of whether initial data with compact support will lead to extinction or persistence is an important one. As an example, consider initial data of the form $u_0 = m\chi_{[-L,L]}$ (here χ represents the characteristic function). It is known that the solution will converge to zero if L is small and will converge to m on compact sets if L is sufficiently large. In fact, there is a critical threshold L^* separating this phenomenon, we point the interested reader to [112] and references within.

3.4   Results - Equation (3.3)

We develop theory for equation (3.3), and begin by establishing some properties of the solutions and global existence and uniqueness. Following, we establish results on persistence and extinction of a species subject to certain initial conditions. We consider both logistic growth and an Allee effect. With particular interest in whether a population can overcome the Allee effect, we consider the case where the Allee effect is incorporated in the birth term .

3.4.1   Global existence and properties of the solutions

In this section we discuss some preliminary properties of solutions to equation (3.3) and the global well-posedness of these solutions with bounded initial data. The first result provides a sort-of maximum principle for equation (3.3).

Lemma 4 (Global lower and upper bounds). *Let g be of bistable or monostable-type, conditions (A1)-(A3) hold, and $0 \leq u_0(x) \leq m(x)$ for all $x \in \mathbb{R}^d$. Then any solution to equation (3.3) must satisfy the bounds $0 \leq u(x,t) \leq m(x)$ for all $x \in \mathbb{R}^d$ and $t > 0$.*

Proof. Let us first assume that the initial data, for some $\varepsilon > 0$, satisfies $0 < \varepsilon < u_0(x) < m(x) - \varepsilon$ in $\mathbb{R}^d$. Assume for contradiction that there exists a first time, $t_1 > 0$, for which there exists an $x_1 \in \mathbb{R}^d$ such that $u(x_1, t_1) = 0$. Note then that $u_t(x_1, t_1) = 0$ and so the solution cannot decay below zero at x_1. A similar argument can be made for the upper bound. If $u(x_1, t_1) = m(x_1)$ for the first time at $t = t_1$ and $x = x_1$ then we see that $u_t(x,t) = -\delta u(x_1, t) = -\delta m(x_1) < 0$. Thus, u

will decay after time $t > t_1$. Taking $\varepsilon \to 0$ gives the result. $\qquad\square$

Our next result proves continuous dependence of initial data.

Lemma 5 (Continuous dependence on initial data). *Assume the conditions from Lemma 1. Let u and v be solutions to equation* (3.3) *with respective initial data $u_0, v_0 \in L^\infty(\mathbb{R}^d)$. Then $w = u - v$ satisfies the following bound:*

$$\|w(\cdot, t)\|_\infty \leq e^{(L-\delta)t}\|w_0(\cdot)\|_\infty, \tag{3.8}$$

for some $L > 0$.

Proof. Let u and v be solutions to (3.3) with initial data $u_0(x)$ and $v_0(x)$, respectively. Note that $w = u - v$ satisfies:

$$w_t = g(u(x,t)) \int_{\mathbb{R}^d} S(x,y)\beta(u(y,t))u(y,t) \, dy - g(v(x,t)) \int_{\mathbb{R}^d} S(x,y)\beta(v(y,t))v(y,t) \, dy - \delta w.$$

For simplicity, we have suppressed the explicit dependence on the spatial variable x above. After some algebra and integration in time we get the following bound for w:

$$
\begin{aligned}
\|w(\cdot, t)\|_\infty &\leq e^{-\delta t}\|w_0(\cdot)\|_\infty + L \int_0^t e^{-\delta(t-s)}\|w(\cdot, s)\|_\infty \, ds, \\
&\leq e^{-\delta t}\|w_0(\cdot)\|_\infty + L \int_0^t \|w(\cdot, s)\|_\infty \, ds
\end{aligned}
\tag{3.9}
$$

where

$$L = \max_K g(u,x)\left(\mathrm{Lip}(\beta)M + \max_K \beta(u,x)\right) + \mathrm{Lip}(g)\left(\max_K \beta(u,x)M\right)$$

with $K = \{(u,x) : 0 \leq u \leq m(x), \ x \in \mathbb{R}^d\}$. Above, we have used the conservation of mass of S and conditions (A1) and (A2). An application of Grönwall's inequality then gives (3.8).

$\qquad\square$

It also holds that solutions to equation (3.3), with $L^\infty(\mathbb{R}^d)$ initial data, exist globally in time and are unique.

Theorem 1 (Global existence and uniqueness of solution). *Under the assumptions made in Lemma 5, equation* (3.3) *with initial data* $u_0 \in L^\infty(\mathbb{R}^d)$, *such that* $0 \leq u_0(x) \leq m(x)$ *in* $\mathbb{R}^d$, *has a unique global solution in the space* $L^\infty(\mathbb{R}^d, [0, \infty))$.

Proof. We use a fixed point argument. Let $\Gamma_T = L^\infty(\mathbb{R}^d, [0, T))$ for suitably small T, which we describe below. Consider now a suitable subset of Γ_T:

$$\Gamma_{T,M} := \{u \in \Gamma_T : \|u(\cdot, t)\|_\infty \leq M \quad \text{for all} \quad t \in [0, T]\}.$$

Let $\tilde{u} = u_0 \in \Gamma_{T,M}$ and let u to be the solution to the problem:

$$u_t(x,t) = g(\tilde{u}, x) \int_{\mathbb{R}^{2d}} S(x, y) \beta(\tilde{u}(y, t), y) u(y, t) \, dy - \delta u(x, t),$$

with initial data $u(x, 0) = u_0(x)$. This problem has a solution and we let F denote the solution map. Using assumptions we have on S, β, and g, and bounding estimates, we have,

$$\frac{d}{dt} \|u\|_\infty \leq (\max_K g(u, x) \max_K \beta(u, x) - \delta) \|u\|_\infty$$

$$\|u\|_\infty \leq \|u_0\|_\infty e^{(\tilde{M} - \delta)t}$$

where $K = \{(u, x) : 0 \leq u \leq M, \ x \in \mathbb{R}^d\}$ and $\tilde{M} = \max_K g(u, x) \max_K \beta(u, x)$. Thus, u grows at most exponentially, and for T suitably small, we have $F : \Gamma_{T,M} \to \Gamma_{T,M}$.

Similar computations to those used to obtain (3.9) and Grönwall's inequality give that the map $\tilde{u} \to u$ is a contraction if T is sufficiently small. A fixed point argument then provides a solution $u(x, t)$ for $t \in [0, T]$. We can then take $u(x, T)$ as initial data and continue this process indefinitely to create our global solution. Finally, uniqueness of the solution is obtained from (5). $\square$

3.4.2   Asymptotic behavior of the solutions

One of the main objectives of this work is to compare the long-term behavior of the solutions with positive initial data to equation (3.3) with those of the solutions to the classical equation (3.1) with the same initial data. First, we consider the case when there is no death.

3.4.2.1   The case when $\delta = 0$

We discuss first the result for the monostable germination function.

Theorem 2 (Monostable germination with $\delta = 0$). *Let $\delta = 0$, $\beta > 0$ and g be of monostable-type and conditions $(A1) - (A4)$ be satisfied. Let u be the unique solution with nontrivial initial data $u_0 \in L^\infty(\mathbb{R}^d)$, satisfying $0 \le u_0 \le m$, which is guaranteed to exist by Theorem 1. Then, for $x \in \mathbb{R}^d$ the following hold:*

   (i) if $u_0(x) > 0$ then $u(x,t) \to m(x)$ as $t \to \infty$;

   (ii) if $u_0(x) = 0$ then $u(x,t) = 0$ for all $t > 0$.

Proof. Let $x \in \mathbb{R}^d$. First, consider the case when $u_0(x) = 0$. Then, $g(u_0(x,t), x) = 0$ and as $\int_{\mathbb{R}^d} S(x,y)\beta(u(y,t),y)u(y,t)\, dy > 0$ we have that $u_t(x,0) = 0$ and so $u(x,t) = 0$ for all t. On the other hand, if $0 < u_0(x)$ then $g(u_0(x,t),x) > 0$ and as $\int_{\mathbb{R}^d} S(x,y)\beta(u(y,t),y)u(y,t)\, dy > 0$ we have that $u_t(x,0) > 0$ for all $t > 0$. In fact, $u(x,t) \to m(x)$ as $t \to \infty$. If not the case, assume for contradiction that $u(x,t) \to w(x)$ with $w(x) \not\equiv m(x)$. Then consider the solution v with initial data $w(x)$, clearly $v_t > 0$ at x, which is a contradiction. $\qquad\square$

Note that equation (3.3), with $\delta = 0$ and g monostable, has an infinite number of weak equilibrium solutions. In fact, $u(x) = \chi_{[a,b]}m(x)$, for any $a < b$, are equilibrium solutions. Moreover, any linear combination of these solutions, with disjoint support, is also a solution. Unlike the classical reaction diffusion equation, there is no regularization in the process governed by (3.3). One might, very naturally, expect that the nonlocal redistribution would help the population grow at locations where the initial data is equal to zero, but this actually does not happen. Note also that if for $x \in \mathbb{R}^d$ fixed, $\int S(x,y)\, dy = 0$ holds then $u(x,t) = u_0(x)$ for all $t > 0$. Figure 3.1 illustrates results from a simulation with g of monostable-type and a potential S that redistributes all the mass in $[-L,0]$ symmetrically to $[0,L]$. That is, all of the mass located at $-x$ relocates to x (with $x > 0$). In the region $x < 0$, Figure 3.1 illustrates that, as $\int S(x,y)\, dy = 0$, condition (A4) does

not hold; hence, $u(x,t) = u_0(x)$ for all $t > 0$. However, in the region $x > 0$, since $\int S(x,y) > 0 \, dy$, the solution u reaches its carrying capacity, $m = 2$, as expected from Theorem 2.

(a) $u(x,0) = u_0$ (b) $u(x,1)$ (c) Long term population density
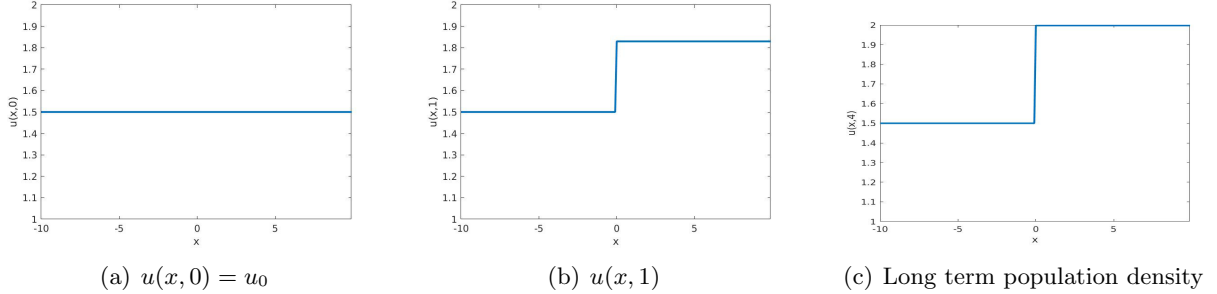
Figure 3.1: Solution to (3.3) with monostable g, $\delta = 0$, $\beta = 2$, and $m = 2$.

Theorem 3 (Bistable germination with $\delta = 0$). *Let $\delta = 0, \beta > 0, g$ be of bistable-type and conditions $(A1) - (A4)$ be satisfied. Let u be the unique solution with nontrivial initial data, $u_0 \in L^\infty(\mathbb{R}^d)$, satisfying $0 \leq u_0 \leq m$, which is guaranteed to exist by Theorem 1. Then, we have the following dichotomy:*

    (i) if $0 < u_0(x) < \theta(x)$ for $x \in \mathbb{R}^d$, then $u(x,t) \to 0$ as $t \to \infty$.

    (ii) if $\theta(x) < u_0(x) < m(x)$ for $x \in \mathbb{R}^d$, then $u(x,t) \to m(x)$ as $t \to \infty$.

Proof. Let $B_1 = \left\{x \in \mathbb{R}^d : 0 < u_0(x) < \theta(x)\right\}$ and $B_2 = \left\{x \in \mathbb{R}^d : \theta(x) < u_0(x) < m(x)\right\}$. First, consider $x \in B_1$. Since $g(u(x,0),x) < 0$ and $\int_{\mathbb{R}^d} S(x,y)\beta(u(x,0),y)u(y,t) \, dy > 0$ in B_1, we have that $u_t(x,0) < 0$. Thus, as u decreases initially, the same argument shows that u is decreasing with t point-wise in B_1. In fact, $u(x,t) \to 0$ as $t \to \infty$ in B_1, by a similar argument as presented in the proof of Theorem 2. This proves (i). If $\delta = 0$ and for $x \in B_2$, since the initial data satisfies $\theta(x) < u_0(x) < m(x)$, then u is increasing. Moreover, note that $u(x,t) \leq m(x)$ for all $t \geq 0$. This implies, that $u(x,t)$ converges point-wise to $m(x)$ in B_2. $\square$

Remark 1. Note that (i) remains true for $\delta > 0$.

    Similar to the monostable case discussed above, equation (3.3) with $\delta = 0$ and g bistable also has an infinite number of weak equilibrium solutions. Here, $u(x) = \chi_{[a,b]}m(x)$ and $v(x) = \chi_{[c,d]}\theta(x)$

for any $a < b$ and $c < d$, are equilibrium solutions. From the modeling perspective, considering $\delta = 0$ and incorporating the strong Allee effect in g, essentially means that we are incorporating the birth and death competition in the function g. The simulation illustrated in Figure 3.2 incorporates the strong Allee effect in g and uses the same potential S as in Figure 3.1. As in Figure 3.1, in the region where $x < 0$, $u(x,t) = u_0(x)$ for all $t > 0$. However, for $x > 0$ where $\int S(x,y)\, dy > 0$, we see the results from Theorem 3 demonstrated. If u_0 is below the Allee threshold, $\theta = .3$, as illustrated in the region where $5 < x < 10$ in Figure 3.2(a), then the population approaches zero in the long term, as seen in Figure 3.2(c). This happens in spite of the fact that all of the mass from the negative region is redistributed to the positive counterpart. If u_0 is above θ, as seen in the region $0 < x < 5$ in Figure 3.2(a), then the population persists and approaches the carrying capacity in the long term, as seen in Figure 3.2(c).

(a) $u(x,0) = u_0$ (b) $u(x,6)$ (c) Long term population density
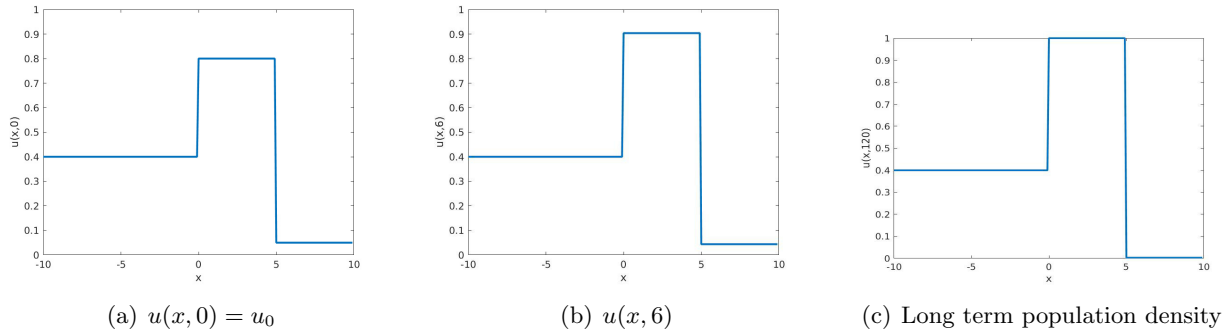
Figure 3.2: Solution to (3.3) with bistable g, $\delta = 0$, $\theta = .3$, $\beta = 2$, and $m = 1$.

Remark 2. It is interesting to consider the case when the strong Allee effect is incorporating in β instead of g. While this is a more difficult situation to consider analytically, we can use simulations to gain insight. Figure 3.3 illustrates a simulation where the Allee effect is incorporated in β, while g is constant, and S remains as defined above. We see in Figure 3.3(a), that for $x > 0$, $u_0(x)$ is below the Allee threshold, and once the solution reaches its equilibrium, as illustrated in Figure 3.3(c), it overcomes the Allee effect to reach the carrying capacity. This is a direct consequence of the redistribution of mass from the negative region to the positive region.

(a) $u(x,0) = u_0$ (b) $u(x,208)$ (c) Long term population density
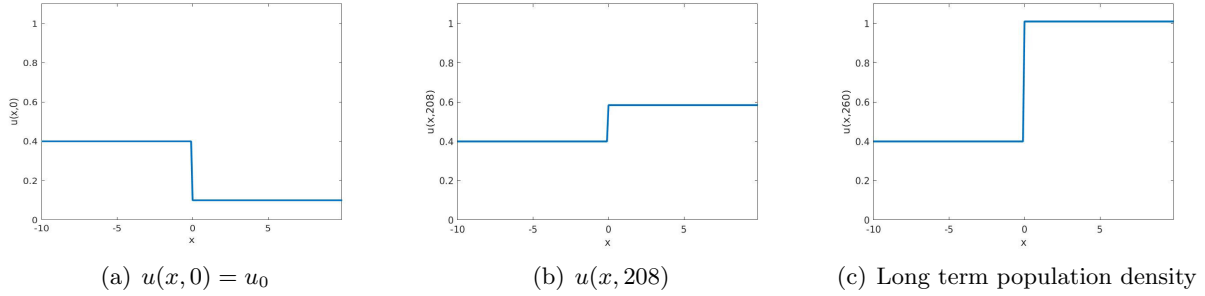
Figure 3.3: Solution to (3.3) with bistable β, $\delta = 0$, $\theta = .3$, $g = 2$, and $m = 1$.

3.4.2.2   The case when $\delta > 0$

When $\delta > 0$ the situation is more delicate. In the section above, we used only the fact that if u_0 is nontrivial and nonnegative then the redistribution term $F(x,t) = \int_{\mathbb{R}^d} S(x,y)\beta(u(y,t),y)u(y,t)\,dy$ is strictly positive, but we never used the actual value. However, this changes when $\delta > 0$ as we are now considering the competition between (possible growth) and decay. Here the actual value of F comes into play and for a general result we would need more information on the redistribution potential. For this work, we only consider the case of a symmetric redistribution kernel, that is $S(x,y) = K(|x - y|)$, and g, β spatially homogeneous (that is m, θ are assumed to be constant). The equation we consider in this section is then:

$$u_t(x,t) = g(u(x,t)) \int_{\mathbb{R}^{2d}} K(|x - y|)\beta(u(y,t))u(y,t)\,dy - \delta u(x,t). \tag{3.10}$$

Rewrite $g(u) = uf(u)$ with f having either one zero (if g is monostable) or two (if g is bistable) and assume further that there exists u_1, u_2 with $\theta < u_1 < u_2$ such that

$$u_1 f(u_1)\beta(u_1) = u_2 f(u_2)\beta(u_2) = \delta. \tag{3.11}$$

Then u_1, u_2 are equilibrium solutions. It is straight forward to obtain the following result.

Theorem 4 (The case $\delta > 0$)**.** *Let g be of bistable-type or monostable-type such that (3.11) holds and $S(x,y) = K(|x - y|)$. Let u be the unique solution with constant initial data $u_0 \in L^\infty(\mathbb{R}^d)$ to (3.10), which is guaranteed to exist by Theorem 1. We have the following dichotomy:*

(a) $u(x,0) = u_0 < u_1$

(b) $u(x, 12.5)$

(c) Long term population density

(d) $u(x,0) = u_0 > u_1$

(e) $u(x,1)$

(f) Long term population density
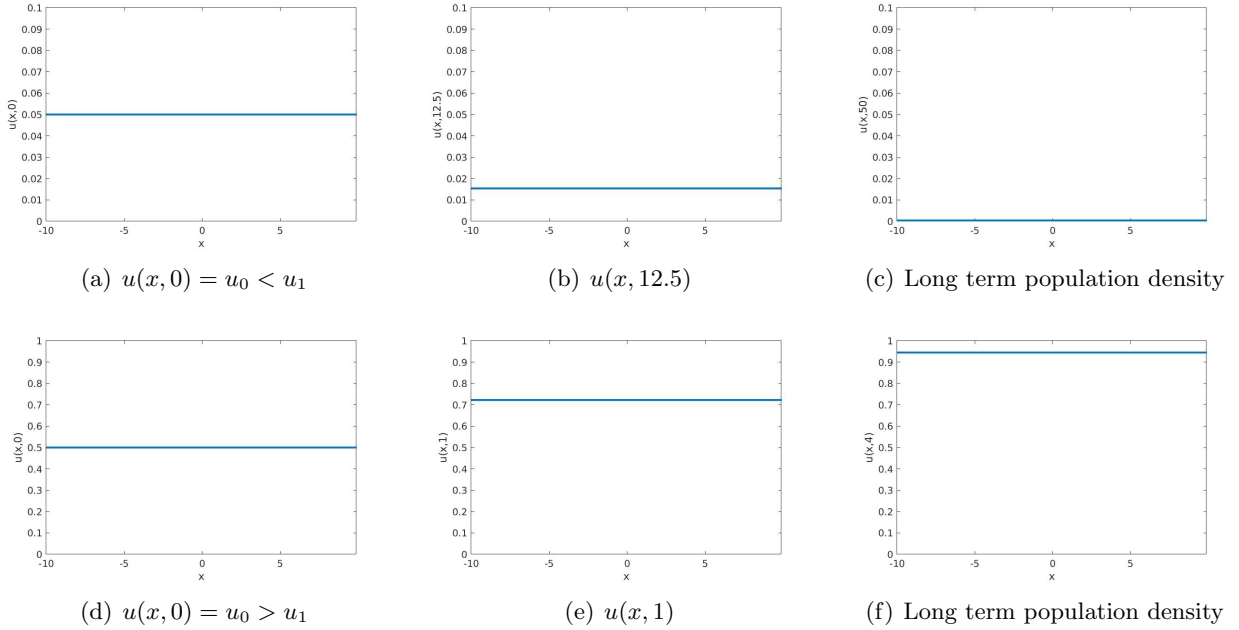
Figure 3.4: Two solutions to (3.3) with monostable g, $\delta = 0.1$, $\beta = 2$, $m = 1$, $u_0 < u_1$, and $u_0 > u_1$, respectively.

(i) If $0 \le u_0 \le u_1$ then $u(x,t) \to 0$ uniformly in x as $t \to \infty$.

(ii) If $u_1 < u_0 < m$ for all $x \in \mathbb{R}$ then $u(x,t) \to u_2$ uniformly in x as $t \to \infty$.

Proof. The key is to realize that as u_0 is constant, the rearrangement does not do anything except to act as a homogeneous growth/decay term. Thus $u(x,t) = u(t)$ for all $t \ge 0$. □

Figure 3.4 demonstrates the results of Theorem 4 with a symmetric redistribution potential, $S(x,y) = \frac{1}{2}e^{-|x-y|}$, and a monostable-type function g. For this case, one can quickly find the equilibrium solutions $u_{1,2} = \frac{1}{2} \pm \sqrt{.2}$. The first simulation with initial data shown in Figure 3.4(a), sets $u_0 < u_1$. As expected, u decays to zero, shown in Figure 3.4(c). The second simulation with initial data shown in Figure 3.4(d), sets $u_0 > u_1$ and shows $u(x,t) \to u_2$, seen in Figure 3.4(f).

Remark 3. Note that in the case when $\delta > 0$ and g is monostable there is actually an Allee effect in place. There are in fact three steady state solutions $0 < u_1 < u_2 < m$.

To gain more insight to the case when $\delta > 0$ we have taken the previous simulations, which

(a) $u(x,0) = u_0$ (b) $u(x, 12.5)$ (c) Long term population density
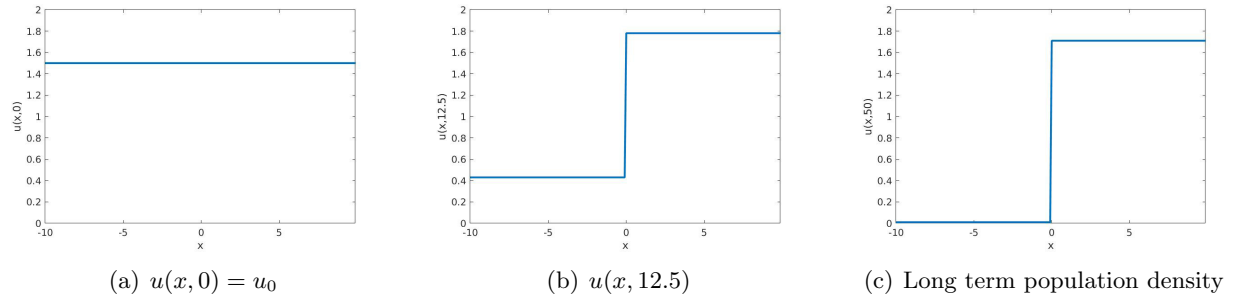
Figure 3.5: Solution to (3.3) with monostable g, $\delta = 0.1$, $\beta = 2$ and $m = 2$.

(a) $u(x,0) = u_0$ (b) $u(x, 10)$ (c) Long term population density
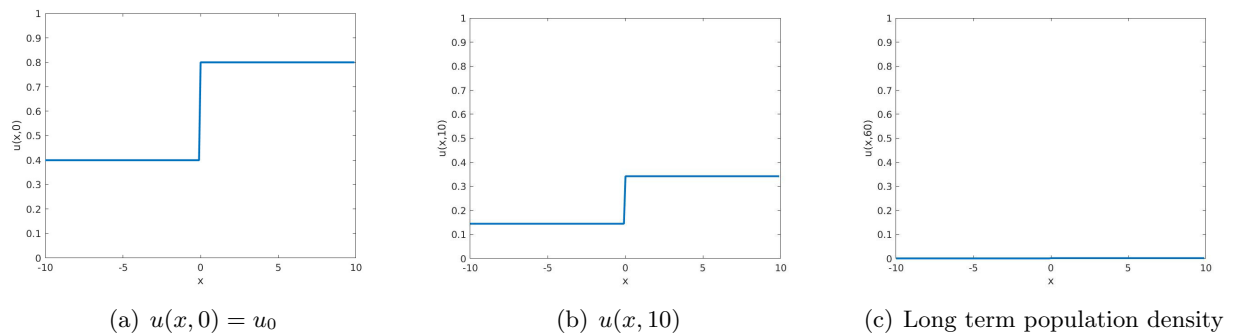
Figure 3.6: Solution to (3.3) with bistable g, $\delta = 0.1$, $\theta = .3$, $\beta = 2$, and $m = 1$.

were performed for $\delta = 0$ and potential S that relocates mass symmetrically from $[-L, 0]$ to $[0, L]$, and run them for $\delta = .1$. In each case, one item of note is that in the region where $x < 0$, we have that $u(x,t) \to 0$ as $t \to \infty$. This is due to the combined facts that $\int S(x,y)\, dy = 0$ for $x < 0$ and the decay due to a positive δ. However, when $x > 0$, Figure 3.5 illustrates a balance between the growth and decay with Figure 3.5(c) being a non-zero equilibrium. In Figure 3.6(a), we have initial conditions that are able to sustain the population at carrying capacity for $x > 0$ when $\delta = 0$. With $\delta > 0$, this is not the case as demonstrated by its equilibrium at zero in Figure 3.6(c). Finally, in Figure 3.7, we model the strong Allee effect in β. With the same u_0 illustrated in Figure 3.7(a), $g = 2$ and $\delta = 0$, note that the population was able to overcome the Allee effect. With the decay incorporated by $\delta = .1$, the population can overcome the Allee effect with sufficiently high g (we have $g = 18$). Indeed, for $x > 0$, although u_0 is below the Allee threshold, it reaches a non-zero

equilibrium in 3.7(c).

(a) $u(x,0) = u_0$ (b) $u(x,11)$ (c) Long term population density
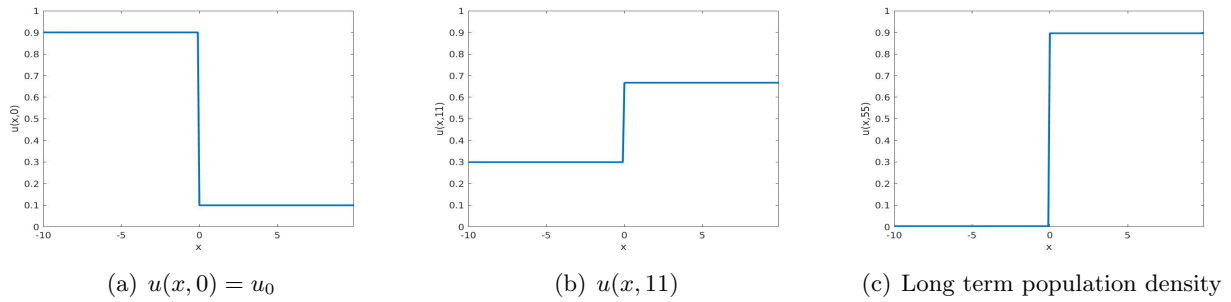
Figure 3.7: Solution to (3.3) with bistable β, $\delta = 0.1$, $\theta = .3$, $g = 18$, and $m = 1$.

3.5   Results - Equation (3.6)

Here, we develop results analogous to Section 3.4. We prove global existence and uniqueness, some properties of solutions, and persistence and extinction results for equation (3.6) with g monostable, g ignition-type, and g bistable. We compare these results to those for equation (3.3).

3.5.1   Global Existence and properties of the solution

In this section we discuss the global well-posedness of solutions to equation (3.6) with bounded initial data. We begin by proving boundedness of solutions to equation 3.6.

Lemma 6 (Boundedness of solutions). *Let conditions (A1)-(A4) hold. Let δ, d be positive constants, $\beta \geq 0$, and g be of bistable, monostable, or ignition-type. Let u be a smooth solution to equation (3.6) with initial data $0 \leq u_0(x) \leq M$. Then, $0 \leq u(x,t) \leq M$ for all $x \in \mathbb{R}^d$, $t > 0$.*

Proof. Suppose $\varepsilon < u_0(x) < M - \varepsilon$, ans suppose there exists a first time t_1 such that $u(x_1, t_1) = 0$ for some $x_1 \in \mathbb{R}^d$. Then, $u_t(x_1, t_1) = d\Delta u$. Because $u(x_1, t_1) \geq 0$ everywhere, then $d\Delta u \geq 0$, and the solution cannot decay below zero. Suppose there exists a first time t_1 such that $u(x_1, t_1) = M$ for some $x_1 \in \mathbb{R}^d$. Then, $u_t = Cg(M, x_1) - \delta M + d\Delta u(x_1, t_1)$ for some positive constant C arising from the integral. Because $M \geq m(x)$, $g(M, x_1) \leq 0$. We also have that $u(x,t) \leq M$ everywhere,

so $d\Delta u(x_1, t_1) \leq 0$. Therefore, $u_t(x_1, t_1) \leq 0$ and u cannot rise above M. Take $\varepsilon \to 0$ to get the final result. □

The following proves continuous dependence on initial data for equation (3.6).

Lemma 7 (Continuous dependence on initial data)**.** *Let conditions (A1)-(A4) hold and g be of monostable or bistable type. Let u and v be solutions to (3.6) with initial data $u_0(x), v_0(x)$ in $L^\infty(\mathbb{R}^d)$. Then, $w = u - v$ satisfies the following bound:*

$$\| w(\cdot, t) \|_\infty \leq e^{(L+d)t} \| w_0(\cdot) \|_\infty$$

for some $L > 0$.

Proof. Let u and v be solutions to (3.6) with initial data $u_0(x)$ and $v_0(x)$, respectively. Note that we can write the solution $w = u - v$ using the fundamental solution of the heat equation, $\phi(x, t)$,

$$
\begin{aligned}
w(x, t) =\ & \int_{\mathbb{R}^d} \phi(x - y, t) w_0(y) dy \\
& + \int_0^t \int_{\mathbb{R}^d} \phi(x - y, t - s) \left[g(u, y) \int_{\mathbb{R}^d} S(y, k) \beta(u, k) u(k, s) dk \right] dy ds \\
& - \int_0^t \int_{\mathbb{R}^d} \phi(x - y, t - s) \left[g(v, y) \int_{\mathbb{R}^d} S(y, k) \beta(v, k) v(k, s) dk - \delta v(y, s) \right] dy ds
\end{aligned}
$$

Through algebra and bounding estimates we obtain the following:

$$
\begin{aligned}
\| w(\cdot, t) \|_\infty \leq\ & \| w_0 \|_\infty + \left\| \int_0^t \int_{\mathbb{R}^d} \phi(x - y, t - s) \right\| g(u, y) \int S(y, k) \beta(u, k) u(k, s) dk \\
& - g(v, y) \int S(y, k) \beta(v, k) v(k, s) dk - \delta w(y, s) \Big\|_\infty dy ds \Big\|_\infty \\
\leq\ & \| w_0 \|_\infty + \int_0^t \| g(u, y) \int S(y, k) \beta(u, k) u(k, s) dk \\
& - g(v, y) \int S(y, k) \beta(v, k) v(k, s) dk - \delta w(y, s) \|_\infty ds \\
\leq\ & \| w_0 \|_\infty + \int_0^t \| g(u, \cdot) - g(v, \cdot) \|_\infty \| \beta(u, \cdot) \|_\infty \| u(\cdot, s) \|_\infty ds + \delta \int_0^t \| w(\cdot, s) \|_\infty ds \\
& + \int_0^t \| g(v, \cdot) \|_\infty \| \beta(u, \cdot) - \beta(v, \cdot) \|_\infty \| u(\cdot, s) \|_\infty + \int_0^t \| g(v, \cdot) \|_\infty \| \beta(v, \cdot) \|_\infty \| w(\cdot, s) \|_\infty \\
\leq\ & \| w_0 \|_\infty + (M Lip(g) \max_K(\beta) + M Lip(\beta) \max_K(g) + \max_K g \max_K \beta + \delta) \int_0^t \| w(\cdot, s) \|_\infty .
\end{aligned}
$$

An application of Gronwall's inequality gives:

$$\| w(\cdot,t) \|_\infty \le e^{(L+\delta)t} \| w_0 \|_\infty$$

with $L = M(Lip(g)\max_K(\beta) + Lip(\beta)\max_K(g)) + \max_K(g)\max_K(\beta)$ and $K = \{(u,x) : 0 \le u \le M, \ x \in \mathbb{R}^d\}$. $\qquad\square$

Now we are ready to prove global existence and uniqueness of solutions.

Theorem 1 (Global Existence and Uniqueness). *Let conditions (A1)-(A4) hold and g be of bistable, monostable, or ignition-type, $\beta \ge 0$. Given initial condition $u_0(x) \in L^\infty(\mathbb{R}^d, [0,T))$ such that $0 \le u_0(x) < M$ for all $x \in \mathbb{R}^d$, we have a unique, global solution to equation (3.6) in $L^\infty(\mathbb{R}^d, [0,\infty))$.*

Proof. We use a fixed point argument. Consider the space $\Gamma_T = L^\infty(\mathbb{R}^d, [0,T))$ for suitably small T, which we describe below. Consider a subset of Γ_T:

$$\Gamma_{T,M} := \{u \in \Gamma_T : \| u(\cdot,t) \|_\infty \le M \text{ for all } t \in [0,T)\}.$$

Consider $u_0 = \tilde{u} \in \Gamma_{T,M}$ and let u be the solution to the equation,

$$u_t = d\Delta u + g(\tilde{u}(x,t),x)\int_{\mathbb{R}^d} S(x,y)\beta(\tilde{u}(y,t),y)u(y,t)dy - \delta u. \qquad (3.12)$$

with initial data $u_0(x)$. Define $F\tilde{u}$ to be the solution map. Using a similar process to Theorem 1 in Section 3.4, we can bound $\|u\|_\infty \le \|u_0\|_\infty e^{(\tilde{M}-\delta)t}$. Thus, u can grow at most exponentially. For T sufficiently small, we have $0 \le u(x) \le M$, and $F : \Gamma_{T,M} \to \Gamma_{T,M}$.

Similar computations to those used in Lemma 7 can be used to show F is a contraction if T is sufficiently small. An application of the Contraction Mapping Theorem provides a solution for $u(x,t)$ for $t \in [0,T]$. We can then use $u(x,T)$ as initial data and continue this process to create the global solution. Uniqueness follows from Lemma 7. $\qquad\square$

The following result establishes smoothness of the solutions $u(x,t)$.

Lemma 8 (Regularity of solutions). *Let conditions (A1) - (A4) hold, g be of monostable, bistable, or ignition-type, and u be the solution to equation (3.6) guaranteed to exist from Theorem 1 with continuous initial condition, $u_0(x)$. Then, $u(x,t)$ is $C^\infty(\mathbb{R}^n, [0,T))$ for $t > 0$.*

Proof. Consider writing the solution to equation (3.6) using the fundamental solution to the heat equation, $\phi(x, t)$,

$$\int_{\mathbb{R}^d} \phi(x - y, t)u_0(y)dy + \int_0^t \int_{\mathbb{R}^d} \phi(x - y, t - s)[g(u, y) \int_{\mathbb{R}^d} S(y, k)\beta(u, k)u(k, s)dk - \delta u(y, s)]dyds$$

$$= I_1(x, t) + I_2(x, t),$$

We have that $u_0(x)$ is continuous, so $I_1(x, t)$ is $C^\infty(\mathbb{R}^n, [0, T))$. Therefore, what is left to show is that $I_2(x, t)$ is $C^\infty(\mathbb{R}^n, [0, T))$. The continuity of $I_2(x, t)$ follows from considering $I_2(x_1, t) - I_2(x_2, t)$, bounding g, β, and $u(x, t)$, using the assumptions on $S(x, y)$, and finally using the continuity of ϕ. Consider the partial derivative of the integrand, I(x,t),

$$\left| \frac{\partial}{\partial x} I(x, t) \right| \leq (\max g \max \beta M + \delta M) \left| \frac{\partial}{\partial x} \phi(x - y, t - s) \right|$$

We know derivatives of the fundamental solution, $\phi(x, t)$, are integrable, and therefore the derivative of the integrand is bounded by an integrable function. We then have,

$$\frac{\partial}{\partial x} I_2(x, t) = \int_0^t \int_{\mathbb{R}^d} \frac{\partial}{\partial x} \phi(x - y, t - s)[g(u, y) \int_{\mathbb{R}^d} S(y, k)\beta(u, k)u(k, s)dk - \delta u(y, s)]dyds.$$

Therefore, we can conclude that $u = I_1 + I_2$ is $C^1(\mathbb{R}^n)$ in its x variables with bounded derivatives. We can iterate this argument to conclude u is C^2, etc, to gain regularity in u. $\qquad\square$

3.5.2   Asymptotic behavior of the solutions

In this section, we develop persistence and extinction results for equation (3.6). We do this for $\delta = 0$ when g monostable and ignition-type, and for g bistable above the Allee Threshold. We also consider the case when $\delta > 0$.

3.5.2.1   The case where $\delta = 0$, g monostable and ignition-type

In order to prove long time behavior of solutions, we first establish a comparison principle.

Lemma 9 (Comparison Principle for monostable or ignition-type g, $\beta, \beta' > 0$). *Let conditions (A1)-(A4) hold, g be of monostable-type or ignition-type, and $\beta, \beta' > 0$. Consider solutions u, v to (3.6) with initial data $u_0(x) > v_0(x)$. Then, we have $u(x, t) \geq v(x, t)$ for all $x \in \mathbb{R}^d$ and $t > 0$.*

Proof. Let $w = u - v$. We have,

$$w_t = \Delta w - \delta w + g(u(x,t),x) \int_{\mathbb{R}^d} S(x,y)\beta(u(y,t),y)u(y,t)dy$$

$$- g(v(x,t),x) \int_{\mathbb{R}^d} S(x,y)\beta(v(y,t),y)v(y,t)dy$$

$$= \Delta w - \delta w + (g(u,x) - g(v,x)) \int_{\mathbb{R}^d} S(x,y)\beta(u,y)u(y,t)dy$$

$$+ g(v,x) \int_{\mathbb{R}^d} S(x,y)(\beta(u,y) - \beta(v,y))u(y,t)dy$$

$$+ g(v,x) \int_{\mathbb{R}^d} S(x,y)\beta(v,y)w(y,t)dy$$

$$= \Delta w - \delta w + g'(\theta,x)w(x,t) \int S(x,y)\beta(u,y)u(y,t)dy$$

$$+ g(v,x) \int_{\mathbb{R}^d} S(x,y)\beta'(s,y)w(y,t)u(y,t)dy$$

$$+ g(v,x) \int_{\mathbb{R}^d} S(x,y)\beta(u,y)w(y,t)dy.$$

We use the Mean Value Theorem above on g and β. Suppose for the first time t_1 that $u(x_1,t_1) = v(x_1,t_1)$. Then, we have that $w(x_1,t_1) = 0$, and $\Delta w(x_1,t_1) \geq 0$, as $u(x,t) \geq v(x,t)$. Therefore, the first integral term evaluated at (x_1,t_1) is zero, and the second and third must be positive due to the positivity of g,S,β,β' and w. Thus, $w_t(x_1,t_1) \geq 0$ and u cannot decrease below v. If g is ignition-type and we consider initial conditions below θ or below θ in some area, a similar argument holds, however some of the positive terms above are simply zero because g is zero below θ □

Remark 4. The above result also holds for g bistable above the Allee threshold. However, below the Allee threshold, g is negative and thus is it possible for $w_t(x_1,t_1) \leq 0$. We comment on this is more detail later.

The existence of positive equilibrium solutions follows from the comparison principle.

Theorem 2 (Existence of equilibrium solutions for g monostable or ignition-type, $\delta = 0$). *Assume the conditions for Lemma 9 hold. Then, equation (3.6) with $\delta = 0$ has at least one positive equilibrium solution.*

Proof. By Theorem 1, we know there exists a global solution to equation (3.6), $\tilde{u}(x,t)$ with constant initial condition $u_0 > 0$ if g monostable, or $u_0 > \theta$ if g or ignition-type. We have that the constant

is a sub-solution, as

$$d\Delta u_0 + g(u_0, x) \int S(x, y)\beta(u_0, y)u_0 dy = g(u_0, x) \int S(x, y)\beta(u_0, y)u_0(y, t)dy > 0.$$

We also can find a super-solution: $M = \sup_{x \in \Omega} m(x)$. Define $w(x, t) = \tilde{u}(x, t + \delta)$ for arbitrary $\delta > 0$; $w(x, t)$ is a solution to (3.6) because the equation is autonomous in time. We also have $w(x, 0) = \tilde{u}(x, \delta) > \tilde{u}(x, 0) = u_0$ because u_0 is a sub-solution. Lemma 9 then implies that $w(x, t) \geq u(x, t)$ for all $t > 0$. Because δ is arbitrary, this implies $u(x, t)$ is increasing in time. However, we also have that $u(x, t)$ is bounded above by M, so we have an increasing sequence that is bounded above. Therefore, $u(x, t) \to u^*(x, t)$ pointwise, for some equilibrium solution, u^*. $\qquad\square$

(a) $u(x, 0)$ (b) $u(x, 1)$ (c) $u(x, \infty)$
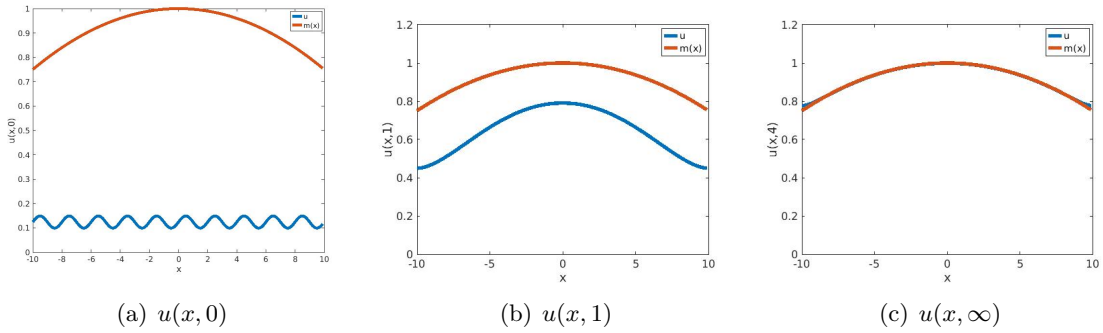
Figure 3.8: Solution to (3.6) with g monostable, $\delta = 0$, $d = 2$, $\beta = 2$

Remark 5. In the case where g is of ignition-type and with initial conditions below θ, u is the solution to the heat equation. This is due to the fact that $g(u, x) = 0$ when $u < \theta$, so the equation is $u_t = \Delta u$. In section 3.5.2.3, we will explore how this changes when $\delta > 0$.

The results of Theorem 2 for g monostable are illustrated in Figure 3.8. The intial condition $u_0(x)$ begins above zero in Figure 3.8(a), and reaches an equilibrium solution around the carrying capacity in Figure 3.8(c). Note that it does not match $m(x)$ exactly, as u is above $m(x)$ at the edges of the domain. This is in contrast to the case where $d = 0$, as the solution $u(x, t)$ is bounded above by $m(x)$.

3.5.2.2   The case where $\delta = 0$, g bistable

In the case where g is of bistable-type, we can prove the comparison principle in the same manner as Lemma 9 when u_0 and v_0 are greater than the Allee threshold, θ. However, this does not hold for bistable g when u_0 and v_0 are not above θ. This is demonstrated in Figure 3.9, as we have two solutions, u and v with $\theta > u_0(x) > v_0(x) \geq 0$, but $u(x,t) < v(x,t)$ for some time $t > 0$ and some $x \in \mathbb{R}^d$

Because we have the comparison principle for bistable g when $u_0(x)$ and $v_0(x)$ are greater than θ, we can then get similar persistence and extinction results to Theorem 2. This is demonstrated in Figure 3.10. We can see for initial condition above θ, in Figure 3.10(a), the population persists at long term, shown in Figure 3.10(c). For initial condition below θ, in Figure 3.10(d), the lack of comparison principle makes proving the analogous result for $u_0(x)$ below the Allee threshold difficult, but our numerical simulations suggest that the population decreases to zero, demonstrated in Figure 3.10(f).

(a) $u(x,0) > v(x,0)$ (b) $u(x,t) < v(x,t)$ in some area
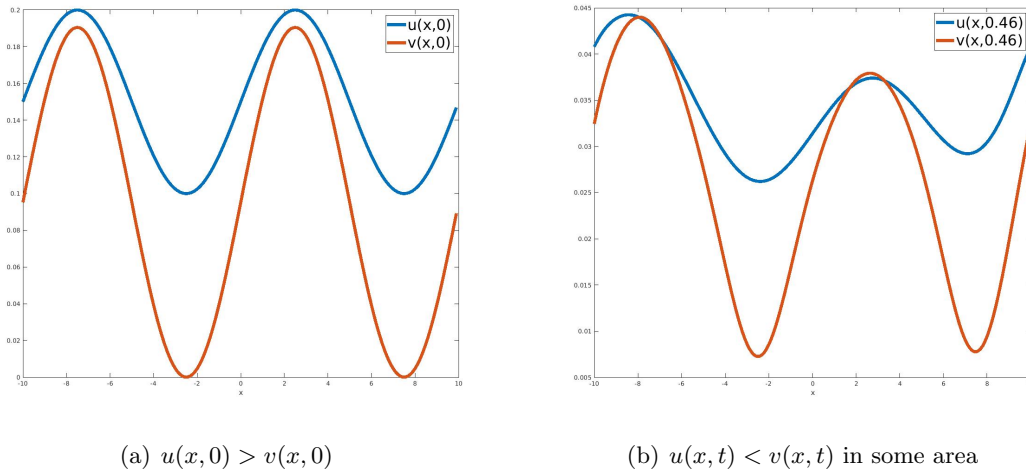
Figure 3.9: Solution to (3.6) with $\delta = 0$, g bistable, β constant, $u_0(x)$, $v_0(x) < \theta$.

3.5.2.3   The case where $\delta > 0$

We can also prove persistence of $u(x,t)$ under certain conditions when $\delta > 0$.

(a) $u(x,0)$ (b) $u(x,1)$ (c) $u(x,\infty)$

(d) $u(x,0)$ (e) $u(x,10)$ (f) $u(x,\infty)$
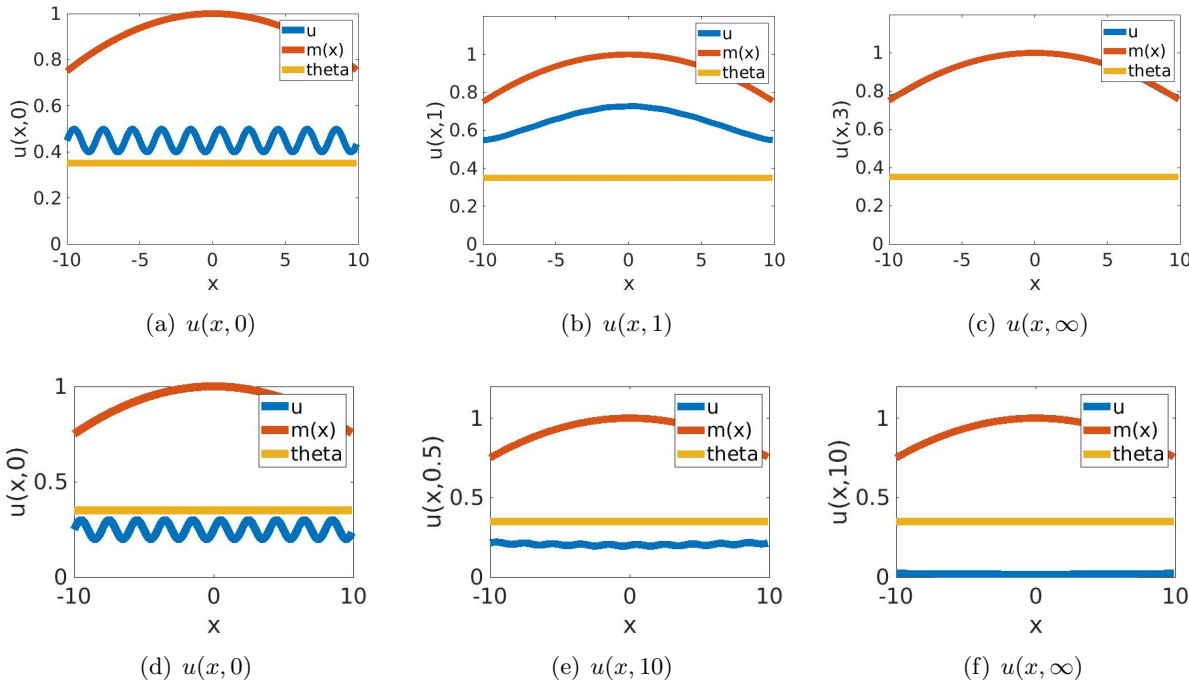
Figure 3.10: Solution to (3.6) with $\delta = 0$, g bistable, β constant
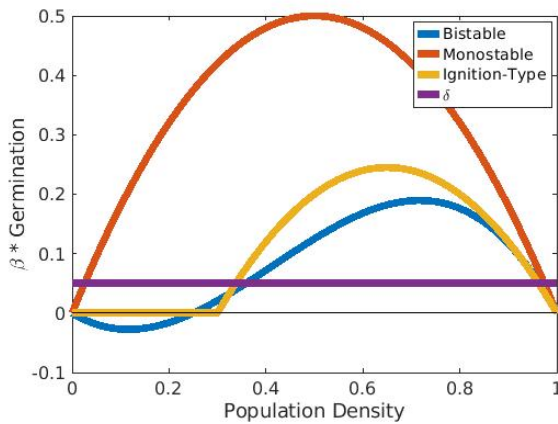
Figure 3.11: $\beta g(u)$ and δ for a fixed x

Theorem 3 (Existence of equilibrium solutions for $\delta > 0$, β constant, and $S(x,y) = S(|x-y|)$)**.**
Assume the conditions for Lemma 9 hold, g be of monostable or ignition-type, and $\beta m^2(x) > 4\delta$ or $\beta(m-\theta)^2 > 4\delta$, respectively. Then, equation 3.6 with $\delta > 0$ has at least one positive equilibrium solution.

(a) $u(x,0)$

(b) $u(x,20)$

(c) $u(x,\infty)$

(d) $u(x,0)$

(e) $u(x,18)$

(f) $u(x,\infty)$
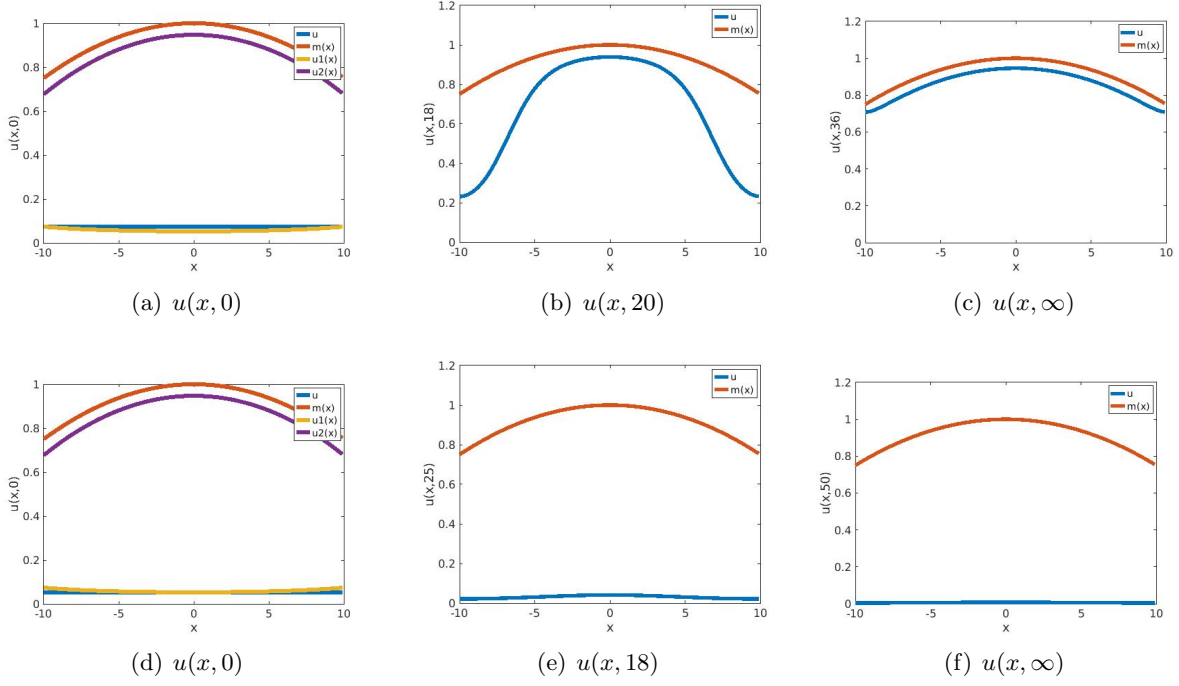
Figure 3.12: Solution to (3.6) with $\delta > 0$, g monostable, β constant

Proof. Consider $g(u,x)\beta - \delta = 0$ and the case where there is a $u_1(x)$ and $u_2(x)$ such that $0 \le u_1(x) \le u_2(x)$ for $x \in \mathbb{R}^d$ that solve this equation. Let $u_1^- = \inf_{x \in \Omega}(u_1(x))$ and $u_1^+ = \sup_{x \in \Omega}(u_1(x))$. If $u_1^+ < u_2(x)$ for all $x \in \mathbb{R}^d$, We can see that u_1^+ is a sub-solution,

$$d\Delta u_1^+ + g(u_1^+, x) \int \beta S(x,y) u_1^+ dy - \delta u_1^+ = g(u_1^+, x)\beta u_1^+ - \delta u_1^+ \ge 0,$$

and u_1^- is a super-solution,

$$d\Delta u_1^- + g(u_1^-, x) \int \beta S(x,y) u_1^- dy - \delta u_1^- = g(u_1^-, x)\beta u_1^- - \delta u_1^- \le 0.$$

By a similar argument to Theorem 2, we can consider use u_1^+ to show the existence of a positive equilibrium solution.

We can also use a similar argument to show an equilibrium solution below u_1^-. Suppose for sake of contradiction this equilibrium solution, $u^*(x)$ was not zero. We know $g(u^*, x) \int \beta S(x,y) u^*(y) - \delta u^*(x)$ is negative for all $x \in \Omega$. Therefore $d\Delta u^*(x)$ must be positive for all $x \in \Omega$ in order for this to be an equilibrium solution. However, $u^*(x)$ cannot be bounded above by u_1^- and also

have $\Delta u^*(x) > 0$ everywhere, so we have reached a contradiction. We can then conclude by the comparison principle that solutions to 3.6 with $u_0(x) < u_1^-$ decrease to zero. $\qquad\square$

See Figure 3.11 for a visual of u_1 and u_2 for a fixed value of x. Examples of a monostable, bistable, and ignition-type g are plotted along with the value of δ. We find $u_1(x) < u_2(x)$ by the intersection with δ and these germination functions. The condition that this theorem needs to meet essentially means that over the entire domain, the largest u value in which the first intersection occurs between $\beta g(u, x)$ and δ cannot be bigger than the smallest u value in which the second intersection occurs.

If g is monostable of the form $g(u, x) = u(m(x) - u)$ and $\beta m^2(x) > 4\delta$ for all $x \in \mathbb{R}^d$, then $\sup u_1(x) < u_2(x)$ for all $x \in \mathbb{R}^d$. This can be shown first by using the quadratic formula to find $u_{1,2}(x) = \frac{m(x)}{2} \mp \frac{1}{2\beta}\sqrt{\beta^2 m^2(x) - 4\beta\delta}$. In order to have two real solutions, we must have $\beta m^2(x) < 4\delta$. From here, we want $\sup_{x \in \mathbb{R}^d}\left[\frac{m(x)}{2} - \frac{1}{2\beta}\sqrt{\beta^2 m^2(x) - 4\beta\delta}\right] < \inf_{x \in \mathbb{R}^d}\left[\frac{m(x)}{2} + \frac{1}{2\beta}\sqrt{\beta^2 m^2(x) - 4\beta\delta}\right]$. We determine the value of x that maximizes or minimizes the two expressions by taking the derivative. We have $u'_{1,2}(x) = \frac{m'(x)}{2}\left(1 \mp \frac{\beta m(x)}{\sqrt{\beta^2 m^2(x) - 4\beta\delta}}\right)$ and can determine from this expression that $u_1(x)$ is maximized and $u_2(x)$ is minimized when $m(x)$ is minimized. We then want $\frac{\inf_{x \in \mathbb{R}^d} m(x)}{2} - \frac{1}{2\beta}\sqrt{\beta^2 \inf_{x \in \mathbb{R}^d} m^2(x) - 4\beta\delta} < \frac{\inf_{x \in \mathbb{R}^d} m(x)}{2} + \frac{1}{2\beta}\sqrt{\beta^2 \inf_{x \in \mathbb{R}^d} m^2(x) - 4\beta\delta}$ which always holds. While the case with ignition-type g is more difficult to do the same analysis, we can follow the same process for two cases: m constant and θ constant. In each case, we can find that if $\beta(m - \theta)^2 > 4\delta$ for all $x \in \mathbb{R}^d$, then $\sup_{x \in \mathbb{R}^d} u_1(x) < \inf_{x \in \mathbb{R}^d} u_2(x)$.

The result from Theorem 3 is demonstrated numerically in Figure 3.12. In Figure 3.12(a) and 3.12(d), $u_1(x)$ and $u_2(x)$ are shown, and $u_0(x) = u_1^+$ and $u_0(x) = u_1^-$, respectively. For $u_0 = u_1^+$, the population persists to a positive equilibrium solution, shown in Figure 3.12(c). For $u_0 = u_1^-$, the population decreases to zero, shown in Figure 3.12(f).

(a) $u(x, 0)$ (b) $u(x, 10)$ (c) $u(x, \infty)$
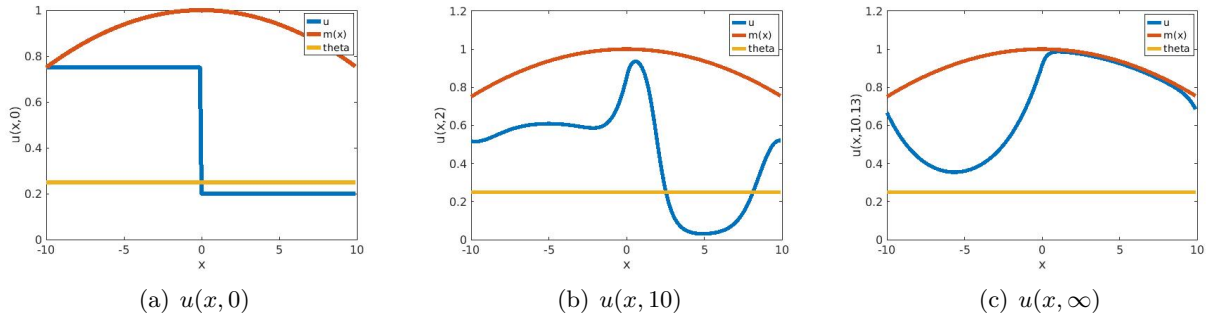
Figure 3.13: Solution to (3.6) with g bistable, β constant, $\delta = 0$.

(a) $u(x, 0)$ (b) $u(x, 10)$ (c) $u(x, \infty)$
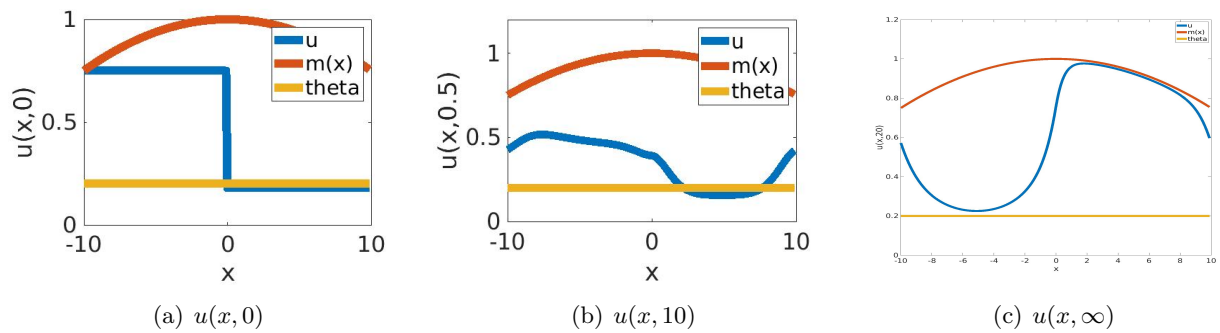
Figure 3.14: Solution to (3.6) with g bistable, β constant, $\delta = 0.1$.

3.5.2.4   Overcoming the Allee Effect

Finally, we use numerical simulations to demonstrate a case that is difficult numerically. We are interested in whether a population can overcome the Allee effect, meaning a population that is initially below the Allee threshold in some area, persists. In the case where $d = 0$, a population beginning below the Allee threshold could not overcome the Allee effect when it was incorporated in $g(u, x)$. This is because the dynamics are governed by an ODE at each spatial location, where $u_t(x, t) < 0$ if $g(u, x) < 0$. However, when $d > 0$, $\delta = 0$, and the Allee Effect is incorporated in g, we see in Figure 3.13 there are some cases where a population can indeed overcome the Allee effect. When $x > 10$, the initial population begins below the Allee threshold, seen in Figure 3.13(a). In Figure 3.13(c), we see the population persists to a positive equilibrium solution. However, it is the local diffusion driving this, as the nonlocal dispersal term is still negative at the spatial locations

below the Allee Threshold.

A population overcoming the Allee efffect can also occur when $\delta > 0$. In this case, without the local diffusion term, a population cannot overcome the Allee threshold when incorporated into g, and without the nonlocal term, a population would not persist either. However, with both of these terms, we can find a case where a population below the Allee threshold persists to a positive equilibrium solution. This is illustrated in Figure 3.14. In Figure 3.14(a), the population begins below the Allee threshold for $x > 0$. At long term, the population persists, shown in Figure 3.14(c). Below the Allee Threshold, the concavity of the solution is causing the diffusion term to be positive, pulling the population above the Allee Threshold. Above the Allee threshold, the nonlocal dispersal term is positive positive, causing growth in the solution to counteract δ. Note that below the Allee Threshold, the redistribution still does not help a population overcome the Allee effect when it is incorporated in the germination term, as the germination term is negative at that spatial location, and the integral is positive. To see the redistribution aid a population in overcoming the Allee effect, we would need the Allee effect to be incorporated in β, as was the case with $d = 0$.

3.6   Conclusions and Future Work

We study a model for birth-jump processes, where birth and dispersal cannot be decoupled, and a variant of this model with an additional linear diffusion term. We consider both logistic growth and an Allee effect, and establish global existence and uniqueness of solutions and persistence and extinction results subject to these growth terms. However, the model with linear diffusion is more difficult and in some cases, the results are more limited, but we also consider a more physically relevant growth term, g ignition-type. We pay particular attention to cases where a population can overcome the Allee effect due to nonlocal dispersal. The Allee effect must be incorporated into the birth term in both cases for redistribution to help a population overcome the Allee effect. However, we only investigate this case numerically. Analytical results for overcoming the Allee effect as well as studying the case for g ignition-type in the case without linear diffusion remains to be investigated.

Chapter 4

Discussion

There is much evidence that nonlocal forces are prominent in ecological phenomena, and thus, it has become of much interest to study nonlocal models. However, the benefit of accuracy to the physical processes that comes from studying nonlocal models also brings a large computational and analytical expense. This work studies both the effects of nonlocal terms incorporated in ecological models, and also ways to analyze these models both theoretically and numerically.

Mechanistic models, based on local dynamics, have been used successfully to understand the leading factors in the formation of territories in different species. However, many species take nonlocal information into account and thus nonlocal mechanistic models are more suitable in those situations. Using a more realistic model comes at a computational cost and when using these models to understand population dynamics by incorporating location data of species of a group, we must solve the model numerous times as we move through a (potentially very large) parameter space. If we take into account that we might have a large system to solve (maybe a double digit number of groups), it becomes imperative that we solve the system efficiently.

In this work, we explore using the energy to find minimizers and derive local approximations to determine if it is suitable to use such approximations. The main takeaway of minimizing energies of the local and nonlocal models is that the situation is more complex than we would like. In some cases the local approximations do a reasonable job approximating the equilibrium solutions of the nonlocal model and can be computed more efficiently; but, this was not always the case. Thus, if this method is to be used, our recommendation, is that the actual data be taken into account to

help ensure that the local approximation and the nonlocal models actually match.

We also use spectral methods to solve the nonlocal system of equations, utilizing the Fast Fourier Transform and properties of the Fourier Transform to reduce the computational cost of the nonlocal term. We are able to find numerical solutions of the nonlocal model, in particular, we are able to find numerical solutions using environmental data and meerkat location data. We also investigate the effect of the potentials and parameters on the solutions and fit the model to synthetic data using stochastic gradient descent to minimize the log-likelihood function. This suggests this is an appropriate direction to take in order to incorporate meerkat location data into the model. We notice that in the process of minimizing the negative log likelihood function, converging to the correct parameters is sensitive to step size. One limitation of this study is that step size is not thoroughly investigated.

Equation (3.3) arises from a process where birth and diffusion cannot be decoupled, which happens in many applications as discussed above. For those applications, the model discussed and analyzed here is a natural replacement for the reaction-diffusion equations. In comparing the dynamics of equation (3.3) to those of equation (3.1), we find some stark differences. For example, note that characteristic functions, $m(x)\chi_{[-L,L]}$, are weak equilibrium solutions of equation (3.3), but no such equilibrium solutions exist for (3.1). Moreover, the dynamics of equation (3.1) are significantly more subtle even when considering simple initial data of the form $u_0 = \chi_A$, where $A \subset \mathbb{R}^d$ is compact. This is due to the compact nature of the initial data and the regularization property of the equation. Equation (3.3) lacks a regularization property and when β is constant the dynamics are governed by g; thus, it behaves like an ordinary differential equation. Initially, these results might appear counter intuitive, as one might naturally think that some aggregating redistribution potentials may actually help overcome the Allee effect. That is to say, that for some potentials S you might expect that if you start with initial data below the Allee threshold, the redistribution might help the population survive. In fact, we see that this is not the case. On the other hand, if we include the Allee effect in β, the dynamics become more complicated and we might expect that for some redistribution potentials the population may overcome the Allee effect.

These expectations are realized as illustrated in our numerical simulations. It would be of interest to characterize potentials that lead the population to overcoming the Allee effect. It is worth pointing out that for many applications, including the ones mentioned here, g and β should really be non-negative. Hence, modeling an Allee effect in g, should correspond to g of ignition-type. We consider this case when studying equation (3.6).

With the addition of the linear diffusion term, we compare solutions to equation (3.6) to the dynamics of solutions to equation (3.3). For one, the solutions to equation (3.6) are continuous. It is also the case that the analysis of equation (3.6) is more difficult when investigating persistence and extinction results, and this prompts studying g ignition-type, which is also more physically relevant. Therefore, we develop persistence and extinction results for g monostable, bistable, and ignition-type. Finally, we find cases where a population can overcome the Allee effect when g is bistable, in contrast to the case without linear diffusion. However, it is still the case that the redistribution term is negative at a location where a population is below the Allee threshold when g is bistable. It remains the case that only if the Allee effect is incorporated in the birth term, the redistribution can aid in a population overcoming the Allee effect.

Bibliography

[1] Traveling waves for a nonlocal anisotropic dispersal equation with monostable nonlinearity. Nonlinear Analysis, Theory, Methods and Applications, 74(3):814–826, 2011.

[2] Frank A Albini. Spot fire distance from burning trees: a predictive model, volume 56. Intermountain Forest and Range Experiment Station, Forest Service, US . . . , 1979.

[3] Nicola J. Armstrong, Kevin J. Painter, and Jonathan A. Sherratt. A continuum approach to modelling cell–cell adhesion. Journal of Theoretical Biology, 243(1):98–113, 2006.

[4] D. G. Aronson and H. F. Weinberger. Nonlinear diffusion in population genetics, combustion, and nerve pulse propagation. In Partial differential equations and related topics, pages 5–49. Lecture Notes in Math., Vol. 446. Springer, Berlin, 1975.

[5] Xueli Bai and Fang Li. Classification of global dynamics of competition models with nonlocal dispersals i: symmetric kernels. Calculus of Variations and Partial Differential Equations, 57:1–35, 2015.

[6] Alethea B. T. Barbaro, Nancy Rodríguez, Havva Yoldas, and Nicola Zamponi. Analysis of a cross-diffusion model for rival gangs interaction in a city. Communications in Mathematical Sciences, 2021.

[7] A. W. Bateman, M. A. Lewis, G. Gall, M. B. Manser, and T. H Clutton-Brock. Territoriality and home-range dynamics in meerkats, Suricata suricatta: A mechanistic modelling approach. Journal of Animal Ecology, 84(1):260–271, 2015.

[8] J. Bedrossian, N. Rodríguez, and A.L. Bertozzi. Local and global well-posedness for aggregation equations and Patlak-Keller-Segel models with degenerate diffusion. Nonlinearity, 24(6):1–31, 2011.

[9] Andrew Bernoff and Chad Topaz. Biological aggregation driven by social and environmental factors: A nonlocal model and its degenerate cahn–hilliard approximation. SIAM Journal on Applied Dynamical Systems, 15(3):1528–1562, 07 2015.

[10] A.L. Bertozzi and Dejan Slepcev. Existence and uniqueness of solutions to an aggregation equation with degenerate diffusion. Communications on Pure and Applied Analysis, 9(6):1617–1637, aug 2010.

[11] Andrea L. Bertozzi and Thomas Laurent. Finite-time blow-up of solutions of an aggregation equation in rn. Communications in Mathematical Physics, 274(3):717 – 735, 2007.

[12] I. Borsi, A. Fasano, M. Primicerio, and T. Hillen. A non-local model for cancer stem cells and the tumour growth paradox. Mathematical Medicine and Biology, 34(1):59–75, 2017.

[13] Brian K. Briscoe, Mark A. Lewis, and Stephen E. Parrish. Home range formation in wolves due to scent marking. Bulletin of Mathematical Biology, 64:261–284, 2002.

[14] N. F. Britton. Reaction-Diffusion Equations and their Applications to Biology. Academic Press, London, 1986.

[15] Luca Börger, Benjamin D. Dalziel, and John M. Fryxell. Are there general mechanisms of animal home range behaviour? a review and prospects for future research. Ecology Letters, 11(6):637–650, 2008.

[16] R.S. Cantrall and C. Cosner. Spatial ecology via reaction-diffusion equations. John Wiley & Sons, West Sussex, 2003.

[17] R. S. Cantrell, C. Cosner, and Y. Lou. Approximating the ideal free distribution via reaction-diffusion-advection equations. Journal of Differential Equations, 245(12):3687–3703, 2008.

[18] Robert Stephen Cantrell, Chris Cosner, and Yuan Lou. Evolution of dispersal and the ideal free distribution. Mathematical Biosciences and Engineering, 7(1):17–36, 2010.

[19] V. Capasso and R. E . Wilson. Analysis of a Reaction-Diffusion System Modeling Man-Environment-Man Epidemics. SIAM Journal on Applied Mathematics, 57(2):327–346, 2013.

[20] J. Carr and A. Chmaj. Uniqueness of travelling waves for nonlocal monostable equations. Proc. Amer. Math. Soc., 132(8):2433—-2439 (electronic), 2004.

[21] J. Carrillo, Katy Craig, and Yao Yao. Aggregation-Diffusion Equations: Dynamics, Asymptotics, and Singular Limits, pages 65–108. 08 2019.

[22] J. Carrillo, Yanghong Huang, and Markus Schmidtchen. Zoology of a nonlocal cross-diffusion model for two species. SIAM Journal on Applied Mathematics, 78, 05 2017.

[23] José A. Carrillo, Raluca Eftimie, and Franca Hoffmann. Non-local kinetic and macroscopic models for self-organised animal aggregations. Kinetic and Related Models, 8:413–441, 2015.

[24] E. Chasseigne, M. Chaves, and J. D. Rossi. Asymptotic behavior for nonlocal diffusion equations. Journal de Mathématiques Pures et Appliquées, 86(3):271–291, 2006.

[25] James S. Clark, Mark Lewis, Jason S. McLachlan, and Janneke HilleRisLambers. Estimating population spread: What can we forecast and how well? Ecology, 84(8):1979–1988, 2003.

[26] N. S. Clayton, P. D. Griffiths, N. J. Emery, and A. Dickinson. Elements of episodic-like memory in animals. Philosophical Transactions of the Royal Society of London Series B, Biological Sciences, 356(1972):1483–1491, 2001.

[27] J. Clobert, E. Danchin, A. Dhondt, and J. D. Nichols. Dispersal. Oxford University Press, Oxford, 2001.

[28] Chris Cosner, Juan Dávila, and Salomé Martínez. Evolutionary stability of ideal free nonlocal dispersal. Journal of Biological Dynamics, 6(2):395–405, 2012. PMID: 22873597.

[29] Hamit Coşkun, Nazmiye Yıldırım, and Samettin Gündüz. The spread of covid-19 virus through population density and wind in Turkey cities. Science of The Total Environment, 751:141663, 2021.

[30] Felipe Cucker and Steve Smale. Emergent behavior in flocks. IEEE Transactions on Automatic Control, 52(5):852–862, 2007.

[31] C. J. Dey, E. Richardson, D. McGeachy, S. A. Iverson, H. G. Gilchrist, and C. A. D. Semeniuk. Increasing nest predation will be insufficient to maintain polar bear body condition in the face of sea ice loss. Global Change Biology, 23(5):1821–1831, 2017.

[32] Salih Djilali. Pattern formation of a diffusive predator-prey model with herd behavior and nonlocal prey competition. Mathematical Methods in the Applied Sciences, 43(5):2233–2250, 2020.

[33] Jean Dolbeault and Benoit Perthame. Optimal critical mass in the two dimensional keller–segel model in $\mathbb{R}^2$. Comptes Rendus Mathematique, 339:611–616, 11 2004.

[34] Raluca Eftimie, Jonathan L. Bramson, and David J. D. Earn. Interactions between the immune system and cancer: A brief review of non-spatial mathematical models. Bulletin of Mathematical Biology, 73(1):2 – 32, 2011.

[35] Raluca Eftimie, G Vries, and M Lewis. Complex spatial group patterns result from different animal communication mechanisms. Proceedings of the National Academy of Sciences of the United States of America, 104:6974–9, 05 2007.

[36] E. Ellefsen and N. Rodriguez. Efficiently finding steady states of nonlocal territorial models in ecology. Journal of Applied Analysis and Computation, 11(6):2664,2686, 2021.

[37] Joep H. M. Evers, Razvan C. Fetecau, and Theodore Kolokolnikov. Equilibria for an aggregation model with two species. SIAM J. Appl. Dyn. Syst., 16:2287–2338, 2017.

[38] Simone Fagioli and Yahya Jaafra. Multiple patterns formation for an aggregation/diffusion predator-prey system. Networks & Heterogeneous Media, 16, 01 2021.

[39] R. A. Fisher. The wave of advance of advantageous genes. Ann. Eugenics, 7:353–369, 1937.

[40] Valeria Giunta, Thomas Hillen, Mark A. Lewis, and Jonathan R. Potts. Local and global existence for non-local multi-species advection-diffusion models. arXiv 2106.0683, 2021.

[41] D. F. Greene and E. A. Johnson. Fruit abscission in acer saccharinum with reference to seed dispersal. Canadian Journal of Botany, 70(11):2277–2283, 1992.

[42] V. Grimm and S. F. Railsback. Individual-based modeling and ecology. Princeton University Press, Princeton, 2005.

[43] Daniel Grünbaum. Using spatially explicit models to characterize foraging performance in heterogeneous landscapes. The American Naturalist, 151(2):97–113, 1998. PMID: 18811411.

[44] Daniel Grünbaum. Advection–diffusion equations for generalized tactic searching behaviors. Journal of Mathematical Biology, 38(2):169 – 194, 1999.

[45] Shay Gueron and Simon A. Levin. The dynamics of group formation. Mathematical Biosciences, 128(1):243–264, 1995.

[46] Bang-Sheng Han, Yinghui Yang, Wei-Jian Bo, and Huiling Tang. Global dynamics of a lotka–volterra competition diffusion system with nonlocal effects. International Journal of Bifurcation and Chaos, 30(05):2050066, 2020.

[47] Michael Heideman, Don Johnson, and Charles Burrus. Gauss and the history of the fast fourier transform. Archive for History of Exact Sciences, 34:265–277, 01 1985.

[48] T. Hillen, B. Greese, J. Martin, and G. de Vries. Birth-jump processes and application to forest fire spotting. Journal of Biological Dynamics, 9(sup1):104–127, 2015.

[49] T. Hillen, K. Painter, and Christian Schmeiser. Global existence for chemotaxis with finite sampling radius. Discrete and Continuous Dynamical Systems - B, 7:125–144, 2007.

[50] Thomas Hillen and Mark A. Lewis. Mathematical ecology of cancer. In Marcello Delitala and Giulia Ajmone Marsan, editors, Managing Complexity, Reducing Perplexity, pages 1–13, Cham, 2014. Springer International Publishing.

[51] P Holgate. Random walk models for animal behavior. In International Symposium on Stat Ecol New Haven 1969, 1971.

[52] V. Hutson and S. Martinez. The evolution of dispersal. Journal of Math. Bio, 47:483–517, 2003.

[53] J. Jacobsen, Y. Jin, and M. A. Lewis. Integrodifference models for persistence in temporally varying river environments. Journal of mathematical biology, mar 2014.

[54] A. M. Kolmogorov, I.G. Petrovskii, and N.S. Piskunov. A study of the diffusion equation with increase in the amount of substance, and its application to a biological problem. Selected works of AN Kolmogorov, 6(1937):1–26, 1991.

[55] Mark Kot, Mark A. Lewis, and P. van den Driessche. Dispersal data and the spread of invading organisms. Ecology, 77(7):2027–2042, 1996.

[56] Simon A. Levin. The problem of pattern and scale in ecology. Ecology, 73(6):1943—-1967.

[57] Herbert Levine, Wouter-Jan Rappel, and Inon Cohen. Self-organization in systems of self-propelled particles. Physical review. E, Statistical, nonlinear, and soft matter physics, 63:017101, 02 2001.

[58] M. A. Lewis, B. Li, and H. F. Weinberger. Spreading speed and linear determinacy for two-species competition models. Journal of mathematical biology, 233:219–233, 2002.

[59] M. A. Lewis and J. D. Murray. Modelling territoriality and wolf–deer interactions. Nature, 366(6457):738 – 740, 1993.

[60] Dong Li and Xiaoyi Zhang. On a nonlocal aggregation model with nonlinear diffusion. Discrete and Continuous Dynamical Systems, 27(1):301–323, 2010.

[61] Wan-Tong Li, Yu-Juan Sun, and Zhi-Cheng Wang. Entire solutions in the Fisher-KPP equation with nonlocal dispersal. Nonlinear Analysis: Real World Applications, 11(4):2302–2313, aug 2010.

[62] Alfred J. Lotka. Elements of physical biology. Nature, 116(2917), 1925.

[63] Frithjof Lutscher. Integrodifference Equations in Spatial Ecology. 01 2019.

[64] Gabriel Andreguetto Maciel and Ricardo Martinez-Garcia. Enhanced species coexistence in lotka-volterra competition models due to nonlocal interactions. Journal of Theoretical Biology, 530:110872, 2021.

[65] G. P. Malanson and N. Rodríguez. Traveling waves and spatial patterns from dispersal on homogeneous and gradient habitats. Ecological Complexity, 33(1):57–65, 2017.

[66] G.P. Malanson and S. J. Walsh. Agent-based models: Individuals interacting in space. Applied Geography, 56:95–98, 2015.

[67] Kalyan Manna, Vitaly Volpert, and Malay Banerjee. Dynamics of a diffusive two-prey-one-predator model with nonlocal intra-specific competition for both the prey species. Mathematics, 8(1), 2020.

[68] M.B.A. Mansour. Traveling wave solutions of a reaction–diffusion model for bacterial growth. Physica A: Statistical Mechanics and its Applications, 383(2):466–472, 2007.

[69] Jonathan Martin. Derivation and investigation of mathematical models for spotting in wildland fire. University of Alberta (Canada), 2013.

[70] Annalisa Massaccesi and Enrico Valdinoci. Is a nonlocal diffusion strategy convenient for biological populations in competition? Journal of Mathematical Biology, 74:113–147, 2017.

[71] Michael S. Mitchell and Roger A. Powell. A mechanistic home range model for optimal use of spatially distributed resources. Ecological Modelling, 177(1):209–232, 2004.

[72] Alex Mogilner and Leah Edelstein-Keshet. A non-local model for a swarm. Journal of Mathematical Biology, 38:534–570, 1999.

[73] P. K. Molnár, A. E. Derocher, T. Klanjscek, and M. A. Lewis. Predicting climate change impacts on polar bear litter size. Nature communications, 2:186, 2011.

[74] P. R. Moorcroft, M. A. Lewis, and R. L. Crabtree. Home range analysis using a mechanistic home range model. Ecology, 80:1656–1665, 1999.

[75] Paul R. Moorcroft and Alex H. Barnett. Mechanistic home range models and resource selection analysis: a reconciliation and unification. Ecology, 89 4:1112–9, 2008.

[76] Paul R. Moorcroft and Mark A. Lewis. Mechanistic Home Range Analysis. Number 43 in Monographs in Population Biology. Princeton University Press, 2006.

[77] Paul R Moorcroft, Mark A Lewis, and Robert L Crabtree. Mechanistic home range models capture spatial patterns and dynamics of coyote territories in yellowstone. 273(1594):1651 – 1659, 2006.

[78] James D Murray. Mathematical biology: I. an introduction. interdisciplinary applied mathematics. Mathematical Biology, Springer, 2002.

[79] Wenjie Ni, Junping Shi, and Mingxin Wang. Global stability and pattern formation in a nonlocal diffusive lotka–volterra competition model. Journal of Differential Equations, 264(11):6891–6932, 2018.

[80] K. Oelschläger. A law of large numbers for moderately interacting diffusion processes. Z. Wahrscheinlichkeitstheorie verw. Gebiete, 69:279–322, 1985.

[81] K. Oelschläger. Large Systems of Interacting Particles and the Porous Medium Equation. Journal of Differential Equations, 88:294–346, 1990.

[82] Akira. Okubo. Diffusion and ecological problems: mathematical models. Biomathematics, v. 10. Springer-Verlag, Berlin, 1980.

[83] Akira Okubo and Simon Levin. Diffusion and ecological problems: Modern perspectives. Springer, New York, NY, 2001.

[84] H. G. Othmer, S. R. Dunbar, and W. Alt. Models of dispersal in biological systems. Journal of Mathematical Biology, 26(3):263–298, 1988.

[85] K. J. Painter, J. M. Bloomfield, J. A. Sherratt, and A. Gerisch. A nonlocal model for contact attraction and repulsion in heterogeneous cell populations. Bulletin of Mathematical Biology, 77(6):1132 – 1165, 2015.

[86] C. Parmesan and G. Yohe. A globally coherent fingerprint of climate change impacts across natural systems. Nature, 421(6918):37–42, 2003.

[87] B. Perthame and P. E. Souganidis. Front propagation for a jump process model arising in spatial ecology. Discrete Contin. Dyn. Syst., 13(5):1235–1246, 2005.

[88] E.C. Pielou. Mathematical Ecology. Wiley, New York, 1977.

[89] Jonathan R. Potts and M. A. Lewis. Spatial Memory and Taxis-Driven Pattern Formation in Model Ecosystems. Bulletin of Mathematical Biology, 81(7):2725–2747, 2019.

[90] Jonathan R. Potts and Mark A. Lewis. How memory of direct animal interactions can lead to territorial pattern formation. Journal of The Royal Society Interface, 13, 2016.

[91] A.P. Ramakrishnan. Dispersal–migration. In B.D. Fath, editor, Encyclopedia of Ecology, pages 930–938. Elsevier, Amsterdam, 2008.

[92] M. D. Redmond, K. C. Kelsey, A. K. Urza, and N. N. Barger. Interacting effects of climate and landscape physiography on piñon pine growth using an individual-based approach. Ecosphere, 8(3), 2017.

[93] N. Rodríguez and G. Malanson. Plant Dynamics, Birth-Jump Processes, and Sharp Traveling Waves. Bulletin of Mathematical Biology, 80(6):1655–1687, 2018.

[94] N. Rodríguez and L. Ryzhik. Exploring the effects of social preference, economic disparity, and heterogeneous environments on segregation. Communications in Mathematical Sciences, 14(2):363–387, 2016.

[95] Nancy Rodríguez and Yi Hu. On the steady-states of a two-species non-local cross-diffusion model. Journal of Applied Analysis, 26(1):1–19, 06 2020.

[96] O. Ronce. How does it feel to be like a rolling stone? Ten questions about dispersal evolution. Annual Review of Ecology, Evolution, and Systematics, 38(1):231–253, 2007.

[97] Edward John Routh. A Treatise on the Stability of a Given State of Motion, Particularly Steady Motion. London: Macmillan and Co, 1877.

[98] Jianshe Yu Shanshan Chen. Stability and bifurcation on predator-prey systems with nonlocal prey competition. Discrete and Continuous Dynamical Systems, 38(1):43–62, 2018.

[99] W. Shen, Y. Lou, and C-Y. Kao. Random dispersal vs. non-local dispersal. Discrete and Continuous Dynamical Systems, 26(2):551–596, oct 2009.

[100] Wenxian Shen and Aijun Zhang. Spreading speeds for monostable equations with nonlocal dispersal in space periodic habitats. Journal of Differential Equations, 249(4):747–795, 2010.

[101] Qingyan Shi, Junping Shi, and Hao Wang. Spatial movement with distributed memory. Journal of Mathematical Biology, 82(4), 2021.

[102] J. G. Skellam. Random dispersal in theoretical populations, 1951.

[103] N. C. Stenseth, A. Mysterud, G. Ottersen, J. W. Hurrel, K.-S. Chan, and M. Lima. Ecological effects of climate fluctuations. Ecology and climatology, 297:1292–1296, 2002.

[104] Y-J. Sun, W-T. Li, and Z-C. Wang. Entire solutions in nonlocal dispersal equations with bistable nonlinearity. Journal of Differential Equations, 251(3):551–581, 2011.

[105] AM Syme, SA McQuarrie, JW Middleton, and BG Fallone. Dosimetric model for intraperitoneal targeted liposomal radioimmunotherapy of ovarian cancer micrometastases. Physics in Medicine & Biology, 48(10):1305, 2003.

[106] L.N. Wasserstein. Markov processes over denumerable products of spaces describing large systems of automata. Problems of Information Transmission, 5:47–52, 1969.

[107] K. White, M. Lewis, and J. Murray. A model for wolf-pack territory formation and maintenance. Journal of Theoretical Biology, 178:29–43, 1996.

[108] K. A. J. White, J. D. Murray, and M. A. Lewis. Wolf-Deer Interactions: A Mathematical Model. Proceedings of the Royal Society B: Biological Sciences, 263(1368):299–305, 1996.

[109] Chufen Wu, Yang, and Xingfu Zou. Spatial-temporal dynamics of a lotka-volterra competition model with nonlocal dispersal under shifting environment. Journal of Differential Equations, 267(8):4890–4921, 2019.

[110] J. Xia, S. G. Sun, and G. H. Liu. Evidence of a component Allee effect driven by predispersal seed predation in a plant (Pedicularis rex, Orobanchaceae). Biology Letters, 9(5), 2013.

[111] Sofya Zaytseva, Junping Shi, and Leah B Shaw. Model of pattern formation in marsh ecosystems with nonlocal interactions. Journal of Mathematical Biology, 80:655–686, 2020.

[112] Andrej Zlato. Sharp Transition Between Extinction and Propagation of Reaction. Journal of the American Mathematical Society, 19(1):1–16, 2005.